The Effect of Solution Heat Treatment on the Tensile and Creep Properties of MarM-002

by
V.R. MING

A Thesis Submitted to the Faculty of Engineering,
University of Cape Town,
for the Degree of Master of Science in Engineering.

Department of Materials Engineering,
University of Cape Town.
1995

Acknowledgements

The student would like to extend his thanks to the following people who have contributed to this work:

Dr. R.D. Knutsen, for supervising the project and providing assistance and guidance.

Prof. A. Ball, for allowing the research to be conducted in the Department of Materials Engineering, UCT.

Dr. N. Comins and J. Benson of the Division of Materials Science and Technology (MATTEK), CSIR, for providing the material and technical assistance.

Dr. C. Lang, who provided many helpful discussions.

Messrs. B. Greaves and J. Petersen, who had to develop and print countless photographs.

Mr. G. Newins, for machining mechanical test specimens.

Mrs. M. Topic, for assistance with the metallographic preparation.

Mrs. J. Sharland and Mrs. A. Ball, for sorting out many administrative problems.

Mrs. D. Young, who provided cups of fortifying tea.

Fellow students of the Department of Materials Engineering, who provided advice, support and much needed light entertainment.

Abstract

The nickel-base superalloy MarM-002 is a high strength precipitation hardening material used in structural applications in the gas turbine field. The microstructure of MarM-002 consists of fine γ' precipitates, a γ matrix, carbides and a eutectic γ-γ', where the γ' can be composed of coarse lamellae or blocky γ' precipitates. Increasing the volume fraction of fine γ' by dissolving the coarse eutectic γ' during solution treatment can raise the alloy strength. In practice the solution heat treatment temperature does not usually exceed 1220°C because of the danger of incipient melting. At 1220°C the eutectic γ' does not dissolve and persists in the alloy structure. In the current project an alternative solution treatment technique, the varied rate solution heat treatment (VRSHT), was determined specifically for MarM-002, and was used to achieve higher solution treatment temperatures up to 1260°C without incipient melting. The microstructural response of MarM-002 to the conventional 1220°C solution heat treatment, and to solution treatment at temperatures above 1220°C, was studied extensively. Microstructural features such as carbide decomposition and the degree of γ' and eutectic γ' dissolution were noted. The tantalum and titanium rich carbides which form during casting were seen to decompose during solution treatment, while hafnium rich carbides precipitated in the interdendritic regions during heat treatment. The γ' solvus and eutectic γ' solvus was measured to be 1260°C and 1280°C respectively. A 1050°C/12h + 870°C/16h ageing heat treatment was applied to the alloy following solution treatment and the effect on the γ' characteristics was also studied.

Creep testing at 900°C/300 MPa and tensile testing at 900°C was performed on the solution treated material following an ageing heat treatment. The creep life showed no significant improvement with increased solution treatment temperature. This is attributed to the relatively easy initiation of failure at carbide sites, which overrides any benefits arising from the increased volume fraction of γ'. However, solution treatment at 1260°C did remove much of the scatter seen in the creep lives. On the other hand, tensile strengths revealed a 10% improvement as the solution treatment temperature increased from 1220°C to 1260°C. This is due to the increased volume fraction of γ' and the greater number of γ-γ' interfaces which oppose dislocation motion.

Contents

1. Introduction

Nickel-base superalloys may be defined as alloys based on the face centred cubic structure of nickel, which are used for elevated temperature service under severe load, and which possess a high degree of surface stability. These materials operate at temperatures up to 85% of their melting temperature and may be found in such fields as jet propulsion, power generation, chemical processing and metal production. Perhaps the most glamorous environment of superalloy usage is the gas turbine field and, most notably, the jet engine. Alloys in a modern jet engine may operate at engine temperatures up to 1343°C, a temperature that is above the melting point of nickel-base superalloys[1,2]. The superalloys manage to operate under such conditions because of air cooling through hollow passages in the turbine components, which effectively reduces the component temperature to below the melting point of the alloy. In these applications, materials are subjected to high frequency oscillating stresses, low frequency thermal stresses and static stresses imposed by the rotating components. Creep and fatigue are major causes of failure. The demand for the economic benefits of greater engine efficiency and longer life have spurred the development of new alloys, processing methods and component design. The history of superalloy development is reviewed briefly below.

1.1 Nickel-base Superalloy Genesis

In 1929 small amounts of aluminium and titanium were added to the face centred cubic 80/20 nickel-chromium alloy, producing significant improvements in creep life and what was, arguably, the first nickel-base superalloy. This was the start of superalloy development, which saw alloys composed of solid solution strengtheners, carbides and a precipitate that was not visually identified for almost ten years. This precipitate, known as gamma prime (γ'), is the major strengthener of nickel-base superalloys. It was soon realised that the strength of the alloys could be increased by increasing the volume fraction of precipitates. From the 1930's to the 1970's alloy chemistry was the main path of superalloy development. Titanium was added to increase the volume fraction and the strength of the precipitates. Refractory elements, first molybdenum and later tungsten, tantalum, niobium and, more recently, rhenium, were added for solid

solution strengthening or precipitate strengthening. Hafnium, boron, carbon and zirconium were added for grain boundary strengthening.

1.2 Superalloy Processing

Vacuum melting for superalloy production was developed in the 1950's, permitting greater compositional control, especially with volatile elements and impurities. Investment casting enabled the production of complex shapes and the use of materials containing large amounts of γ'. In the 1960's directional solidification was developed, to produce components with elongated or columnar grains[3]. The directionally solidified alloys exhibited increased ductility, fatigue limit and creep life by removing many grain boundaries transverse to the stress axis. The number of the major failure initiation points (grain boundaries) were drastically reduced by this production method. Various alloys were adopted by turbine engine companies. MarM-200 + Hf was adopted by Pratt-Whitney, MarM-247 by Garrett, René 80H by General Electric and MarM-002 by Rolls-Royce. Turbine blades made of directionally solidified (DS) alloys have been used for up to 15 000 hours in commercial turbofan engines for long distance flights. However, it proved difficult to solution treat DS alloys, because incipient melting limited the heat treatment temperatures that could be used. This was traced to the presence of the grain boundary strengtheners Hf, C, B and Zr. The lower solution treatment temperatures could not dissolve the coarse γ' and thus the volume fraction of the fine strengthening γ' could not be maximised, since it was "tied up" in the coarse γ' precipitates.

Pratt-Whitney pioneered single crystal casting technology in the mid-1960's, thus eliminating the need for the grain boundary strengthening elements[4]. Alloy 454, later known as PWA-1480, was the first successful superalloy designed for single crystal use. The single crystal alloy René N-4 was adopted by General Electric, SRR 99 and RR 2000 by Rolls-Royce, AM1 by the Office National d'Etudes et de Recherches Aerospatiales (ONERA) and CMSX-2, CMSX-3 by Cannon-Muskegon. Extensive γ' dissolution could be achieved without incipient melting and whereas the DS alloys had temperature capabilities in the region of 980°C to 1020°C, the single crystal alloys operated at around 1040°C. More

recent second generation alloys, such as CMSX-4 and PWA-1484, containing rhenium[5,6,7,8], operate at temperatures of approximately 1060°C.

1.3 Advantages of the Directionally Solidified Alloys

Although the single crystal alloys "have stolen the glamour", directionally solidified alloys continue to be used, because of the ease of production of components. Long, shrouded blades are expensive to produce as single crystals. The complex cooling passages used in a turbine blade are easier to produce in a DS casting than in a single crystal component. This is due to the fact that the single crystal alloy requires a less complex core shape in order to avoid residual casting stresses which can cause recrystallisation during subsequent heat treatment. The simpler air passage configuration of the single crystal casting results in less efficient cooling and the temperature advantage of the single crystal alloy can thus be negated.

1.4 Aims of this Project

Since directionally solidified alloys remain in widespread use, the polycrystalline alloy MarM-002 was selected for study. The broad aim of this project involved an investigation of the microstructure-mechanical property relationships pertaining to the alloy. The precise aim was twofold; firstly, to increase the volume fraction of fine γ' in the material. This was proposed through effective solution heat treatment at higher temperatures than the norm, which would dissolve as much of the coarse eutectic γ' as possible. Subsequent ageing of the optimally solution treated structure would lead to a more homogeneous distribution of γ' precipitates. In view of the fact that extensive dissolution of the γ' in MarM-002 is regarded as difficult due to limitations introduced by the occurrence of incipient melting[9], an alternative method of solution heat treatment was considered.

Secondly, the effect of the solution treatment temperature (and thus the amount of fine γ' in the alloy) was investigated by mechanically testing the solution treated and aged material. The mechanical tests comprised both tensile and creep testing.

2. Literature Review

2.1 Superalloy Composition and Microstructure

Nickel-base superalloys are precipitation hardened materials composed fundamentally of nickel and aluminium. The chemical composition of commercial nickel-base superalloys is complex, having evolved both empirically and from electron theory (for example, valence electron theory[10] and the d-electron concept[11]). Alloying additions commonly include Ti, Cr, Co, W, Ta, Mo, Re, Nb, Hf, C and Zr. Generally the alloys consist of four phases: the matrix phase (γ), intermetallic precipitates (γ'), a eutectic γ-γ' and carbides.

2.1.1 The Matrix and Precipitate

The fundamental characteristics of the γ and γ' phases may be illustrated in the Ni-Al phase diagram (Fig. 2.1) in the region composed of approximately 77 at.% to 90 at.% Ni.

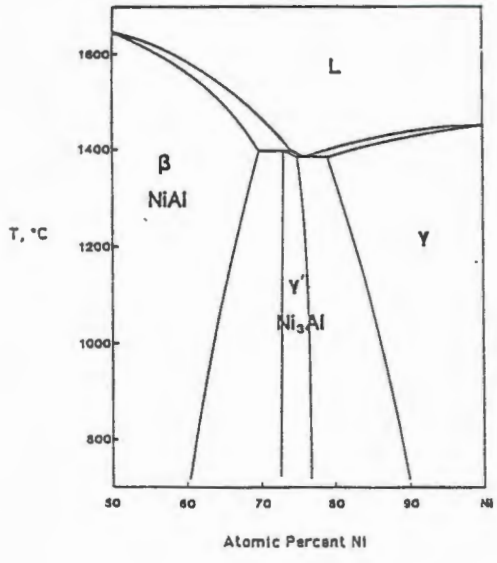

Figure 2.1. The Ni-Al Phase Diagram

In this compositional range, alloys consist of two phases, γ and γ'. The γ phase is a face centred cubic (fcc) solid solution of nickel and aluminium atoms and the γ' phase is an ordered intermetallic Ni_3Al with a $L1_2$ structure (Fig. 2.2). The face

centre sites of the γ' superlattice are occupied by nickel atoms and the corner sites are occupied by aluminium atoms. The gamma prime precipitates out within the γ matrix at temperatures below the γ' solvus temperature, usually with a high degree of coherency between the two phases, both having lattice parameters in the region of 3.58 Å[12,13]. The coherency plays an important part in the coarsening behaviour and strengthening properties of the precipitates.

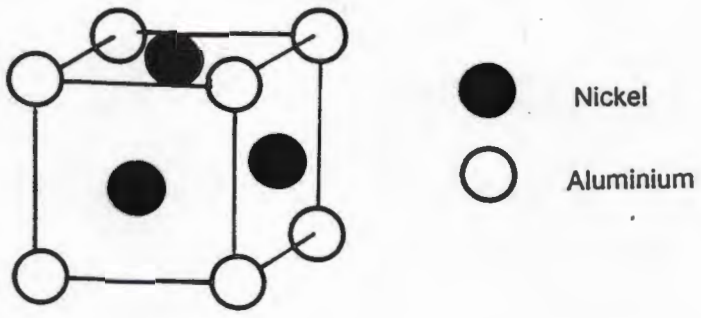

Figure 2.2. The $L1_2$ structure of the γ' phase with preferred atomic sites

Manipulation of these two phases through judicious alloying enables the microstructural and mechanical properties to be tailored to a particular purpose. The maximum solubilities of the alloying additions in pure nickel are listed in Table 2.1.

Element	Solid Solubility (at.%)	Temp. of Max. Solubility (°C)
C	2.7	1318
Cr	50	1345
Co	complete	-
Mo	27	1315
W	17.5	1500
Nb	14	1270
Fe	complete	>910
Ti	15	1287
Al	21	1385
Ta	15.4	1360
V	43	1200

Table 2.1. Maximum solid solubility of common alloying elements in nickel (Reference 14)

The elements are often classified as either γ' formers or γ formers, depending on their partitioning behaviour and the preferred lattice sites. Gamma prime precipitate formers (Al, Ti, Nb and Ta) partition preferentially to the γ' phase where they substitute for aluminium atoms in the γ' superlattice[15,16]. Similarly, γ formers (Cr, Co, Mo and Re) partition largely to the γ phase where they substitute for nickel in the FCC solid solution as well as in the γ' superlattice[15,16]. From Table 2.2.1 it can be seen that the elements with low solubility in nickel are predominantly γ' formers. As with any alloy system, however, some anomalies do exist, notably tungsten and cobalt. The partitioning behaviour of W appears to be a function of the alloy composition as it may partition strongly to either phase[13,17,18] or equally between phases[17]. It was previously assumed that Co substitutes largely for Ni in the γ', but there are indications that a surprising portion of the Co substitutes for aluminium in the precipitate. Thus, the γ' superlattice consists of atoms of Ni, Cr or Co on the cube faces and Al, Ti, Ta, W or Re on the cube corners.

A curious feature of γ' precipitates in nickel-base superalloys is the morphological changes which often occur during precipitate growth. It is well known that γ' precipitates may undergo shape changes from spherical to cuboidal to a rafted (lamellae), dendritic or rod like structure[19, 20]. The underlying reason for these shape changes is the balance between the surface energy:volume ratio and the elastic interaction between precipitates, which is governed by the lattice misfit. For example, where precipitates are small and spherical the coherency stresses between the particles are small and hence the minimisation of the surface energy is a driving force, leading to the spherical morphology. As the precipitate size increases, however, the coherency stresses increase and elastic interaction between particles begins to play an important role. Because the elastic modulus of the γ' is at a minimum in the (001) direction, the stress in this direction is also at a minimum and hence the elastic interactions cause the flattening of the precipitate faces in this plane, resulting in the characteristic cuboidal morphology of γ' precipitates. With a further increase in precipitate size the γ' may undergo rafting, ogdoadal or "dendritic" growth. These processes appear to be the result of resolved internal and applied stresses leading to directions of preferred growth.

2.1.2 The Eutectic γ-γ' Phase

The eutectic phase is formed in the final liquid zone as a result of solute rejection during solidification from the melt (see section 2.6.2) and is comprised of γ' precipitates arranged in a rosette or blocky structure. As will be seen in later sections, the eutectic is considered to be detrimental to mechanical properties.

2.1.3 Carbides

Carbides are generally found only in superalloys designed as polycrystalline alloys, where they serve as grain boundary strengtheners. The carbides are usually of the MC, M_6C or $M_{23}C_6$ type[21], where M may be Ta, Ti, Hf, Nb or Cr. The carbides may have a blocky morphology, but the MC carbide may also be script-like, and the $M_{23}C_6$ carbide may exist in a plate or geometric form. The M_6C carbide has been found in a Widmanstatten arrangement on rare occasions[21].

The MC carbide has a FCC structure and is usually formed during casting. Hf, Ta, Nb and Ti are known to be MC formers[14,15,22,23], although there is disagreement concerning the ranking of the elements as preferential MC formers[21,24]. There are at least three forms of MC carbide; MC-1, MC-2 and MC-3 with lattice parameters in the region of 4.39Å, 4.50Å and 4.59Å respectively[23,25]. The MC-1 carbide is rich in (Ti+Ta), the MC-2 carbide in (Ti+Ta+Hf) and MC-3 in (Hf+Ta). In Hf containing alloys there is a tendency for (Ta,Ti)C to decompose and form HfC during thermal treatment[23-25]. Thermal treatment may likewise result in decomposition of the MC carbide to the complex cubic $M_{23}C_6$ or M_6C type.

$M_{23}C_6$ carbides form when the chromium content is moderate to high and the carbide is rich in Cr, although Mo, Ni, Co, Ti, W or Nb may be present[14]. M_6C carbides are rich in W, Fe, Ni or Co (ref 14) and may be found when the Mo or W contents are above 6 at.% (ref.21).

2.2 Role of the Alloying Elements

Alloying additions to the fundamental Ni-Al system are used to alter the microstructural, mechanical and physical properties of the alloys. A delicate balance must be achieved for the desired properties, since the alloying elements may have opposing effects on any given property. A brief description of the role of some alloying elements is given below.

2.2.1 Solid Solution Strengthening

Tungsten, molybdenum, cobalt and chromium provide solid solution strengthening to the matrix of the superalloy[14,15,25]. The effective solid solution strengthening capabilities are listed in Table 2.2.

Element	% Change in Lattice Parameter of nickel per atom % solute	Change of flow stress (ε=0.0002) per atom % solute (MPa.at%$^{-1}$)
W	0.135	16.5
Mo	0.116	14.2
Ti	0.095	22.7
Cr	0.032	4.9
Fe	0.031	3.3
Co	0.005	0.3

Table 2.2. Effect of solutes on the solid solution strengthening of nickel. (Reference 15)

The refractory additions (W, Mo) have a large effect per atom solute, but it should be noted that Cr and Co may have a high strengthening effect because of the higher contents of these elements (~10 at.%). This may be further enhanced by a build up of chromium atoms around the interface of the γ-γ', which may increase the ability of chromium to oppose dislocation shear[16,26].

2.2.2 Gamma Prime Formers

The refractory elements, Ti, Ta and Nb, increase the volume fraction of γ' and raise the γ' solvus temperature, thus permitting higher service temperatures for the alloy[13,27]. Conversely, cobalt and iron lower the solvus temperature. There are indications that chromium raises the solvus temperature[28].

The precipitates are strengthened by the additions of Ti, Ta, W or Re, possibly through an increase in the anti-phase boundary energy[27]. Lattice mismatch and coherency strains are increased with the addition of refractory elements Ta, Ti, Nb or Mo (Ref. 13, 15, 29).

2.2.3 Grain Boundary Strengtheners

The propagation of rupture cracks along grain boundaries has led to the addition of the strengthening elements hafnium, boron, zirconium and carbon to the superalloy chemistry. Hafnium increases the volume fraction of eutectic γ-γ' found at the grain boundaries and interdendritic zones. However, it hinders grain boundary sliding and increases the strength of the grain boundaries[30] by raising the yield strength of the blocky eutectic γ' and promoting the formation of discrete carbides at the grain boundaries.

Zirconium and boron additions have increased rupture lives and ductility in superalloys. Both elements segregate to the grain boundaries and prevent the formation of carbide agglomerates, which would reduce grain boundary ductility. Zirconium removes sulphur impurities from grain boundaries by forming carbosulphides[15,21].

2.2.4 Surface Protection

Oxidation is of concern in any high temperature material and in superalloy components the surface protection is obtained from both coatings and the nickel, chromium and aluminium oxides formed by the alloying elements[31]. Chromium oxide provides effective oxidation protection at temperatures below 950°C, but above this temperature aluminium oxide is more effective.

Hot corrosion, the process in which contaminants on the surface of the alloy form a low melting point compound which eats into the material, is hindered by the presence of both chromium and titanium oxide layers[32]. Titanium oxide on the other hand is detrimental to oxidation resistance[27].

2.3 Heat Treatment of Nickel-base Superalloys

The heat treatment of nickel-base superalloys generally involves a solution heat treatment followed by one or more ageing heat treatments. Ideally, a solution heat treatment temperature above the γ' solvus but below the melting point of the alloy is used. Most modern superalloys have a γ' solvus temperature in the region of 1200°C to 1300°C. The ideal solution heat treatment should therefore dissolve all of the precipitates including the eutectic γ' phase, permitting the γ' to be re-precipitated in a controlled fashion during the ageing heat treatments. Chemical segregation can also be greatly reduced by the solution heat treatment.

The first or primary ageing treatment takes place at temperatures in the region of 1000°C to 1100°C for approximately 10 hours and serves two purposes. Firstly, it simulates a coating cycle (surface protection coatings are applied to components) and secondly, it serves to bring about nucleation and growth of the γ' precipitates. Growth of the precipitates occurs through Ostwald ripening and as a first approximation may be described by the Lifshitz-Slyozov-Wagner (LSW) relationship[33,34] where :

$$r^3 - r_0^3 = kt \qquad (2.1)$$

where r and r_0 are the final and initial γ' radii or cube lengths, k is a constant and t is the time at temperature.

It should be noted that the LSW theory is strictly applicable to low volume fraction precipitate systems where the matrix behaves as a fluid and there are no interaction stresses between matrix and precipitate. The theory therefore fails to predict the precipitate size distribution and incorrectly predicts a maximum precipitate size of 1.5r (references 29 and 35 for example). There have been a number of other theories[36,37,38] which have been reviewed by MacKay and Nathal[29], but a detailed discussion of γ' coarsening is beyond the scope of this text.

The secondary ageing heat treatment usually takes place at temperatures in the region of 870°C and has been shown to remove γ' formers from the matrix, thus

increasing the volume fraction of γ'. Additionally there are indications that the second ageing heat treatment forms a build-up of chromium atoms in the matrix at the γ-γ' interface, which may have a strong interface strengthening effect[26]. The ageing treatment serves, further, to alter carbide characteristics.

2.4 Incipient Melting

Incipient or localised melting may occur during solution heat treatment and can complicate heat treatment and degrade mechanical properties. Localised melting may lead to brittleness and premature failure (reference 39 for example) and serves as a limit to the solution treatment temperature, thereby reducing the amount of fine γ' that may serve as material strengtheners. The melting is associated with chemical segregation during the casting and solidification process, which results in the formation of low melting point compounds in the interdendritic areas of the alloy. The grain boundary strengthening elements Hf, C and Zr are the elements most commonly associated with incipient melting and the problem is thus most evident in polycrystalline alloys[39,40,41,42,43]. In modern single crystal alloys the grain boundary strengtheners are not present and the formation of low melting point compounds is much less likely. The segregation in the single crystal alloys can usually be removed, to a large extent, by the solution heat treatment.

Incipient melting is associated with Ni_5Hf, Ni_7Hf_2 and Ni_3Hf compounds, with melting temperatures covering a wide range, from about 1135°-1477°C (references 40,41,42). Compounds such as ZrS, NiZr intermetallic and TiS are also associated with melting at temperatures of 1170°C (reference 43). In some cases the low melting point compounds may be removed by a homogenization treatment at temperatures below the incipient melting temperature; for example a two step 1230°C/2h + 1260°C/2h solution treatment may be used for MarM247LC (reference 39). Yunrong et al[40,41] have described how Ni_5Hf may be transformed into eutectic γ-γ' and HfC, or dissolve into solid solution by an intermediate temperature dwell at 1150°C in the alloy DS MarM200 + Hf. They have also shown how the addition of carbon may facilitate the formation of HfC and thereby reduce the volume fraction of Ni_5Hf formed during solidification. The reduction in Ni_5Hf appears to raise the melting temperature by allowing the

compound to dissolve more readily during the heating stage of the solution treatment cycle.

The morphology of a region of incipient melting may range from cellular or blocky to a composite form, consisting of the Ni-Hf compound surrounded by a fine eutectic γ-γ' and MC carbides[39–41] (Fig.2.3).

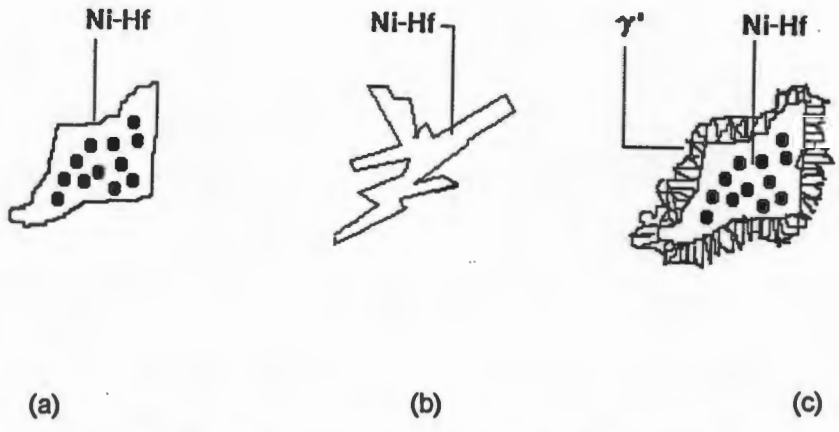

Figure 2.3. The morphology of incipient melting may be a) cellular, b) blocky or c) composite

The composite morphology of melting is formed when the Ni-Hf melts, forming a liquid pool that erodes the surrounding eutectic, causing it to melt partially. On cooling the Ni-Hf re-precipitates and a loop of eutectic γ-γ' forms around the compound. A reaction between Hf in the Ni-Hf compound and in the eutectic, and any carbon in the eutectic or surrounding carbides, may lead to Hf-rich carbides being deposited on the site of localised melting.

2.5 Directional Solidification of Nickel-base Superalloys

Superalloys were solely used in a conventionally cast (CC) equi-axed grain form until the mid to late 1960's. Pratt & Whitney introduced directionally solidified (DS) columnar grained alloys in military turbine engines in 1969 and in commercial engines in 1974 (Ref. 3, 4). The benefits of DS alloys were

increased creep rupture and thermal fatigue lives and ductilities. There are two primary reasons for the superiority of DS superalloys[1,27,44]; firstly the elimination of transverse grain boundaries removed a failure initiation site, thereby increasing ductility and creep lives. Secondly the columnar grained material exhibited a preferred low elastic modulus [001] texture which reduced thermal stresses and improved thermal fatigue properties. An extension of the columnar grain concept is the single crystal (SC) material developed by Pratt & Whitney (Ref. 3, 4). The relative benefits of single crystal and directional solidification over conventional casting are illustrated in Figure 2.4.

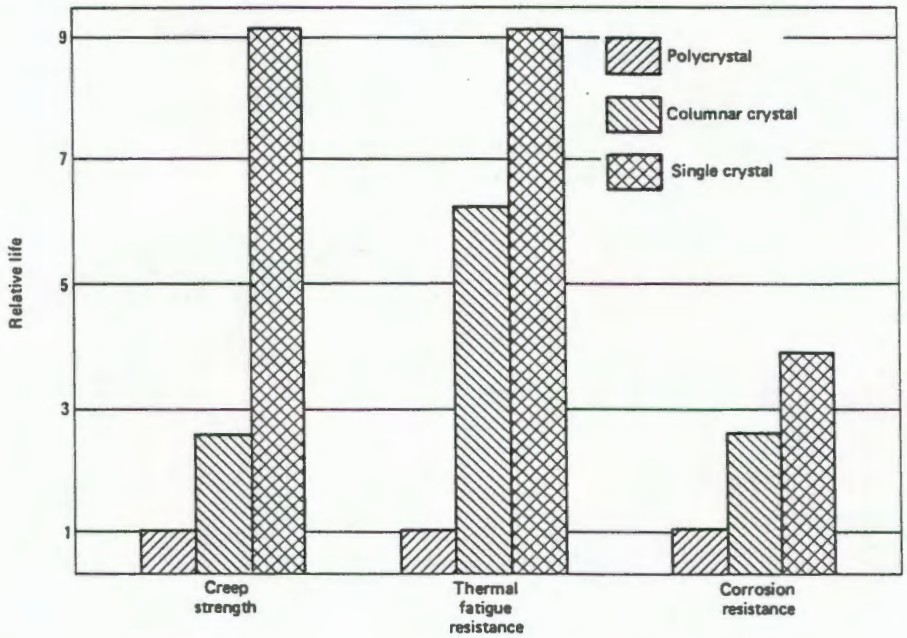

Figure 2.4. A comparison of Equi-axed, Columnar Grained and Single Crystal Superalloys (Reference 1)

Mclean[44] has noted that the alloys receiving the most benefit from the DS process have relatively low rupture ductilities in the CC form (e.g. MarM-200, MarM-246, IN-100). An extension of their ductility therefore results in increased rupture lives (Fig.2.5).

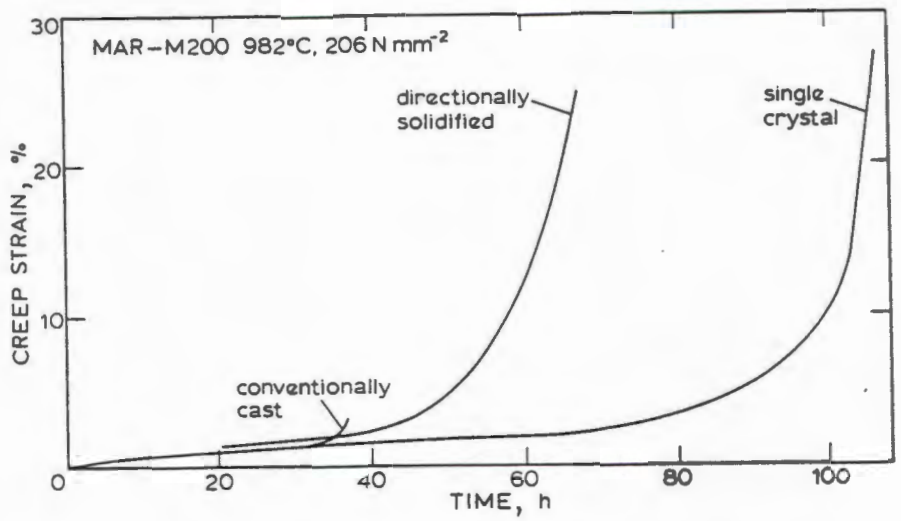

Figure 2.5. Creep curves for CC, DS and SC MarM-200 at 982°C and 206MPa (Ref. 44)

2.5.1 Production of Directionally Solidified Superalloys

The most commonly used method of producing DS alloys is the withdrawal or power down method, illustrated in Fig.2.6.

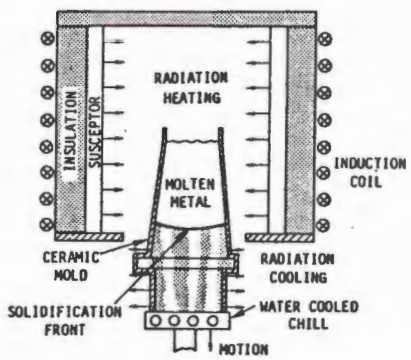

Figure 2.6. The withdrawal method used for the production of DS material (Ref.3).

The casting process in Fig.2.6 takes place under vacuum. Molten metal is poured into the ceramic mould which has been preheated to a temperature above the liquidus of the alloy. The mould is open-bottomed and is located on a water cooled copper chill plate. As the molten liquid contacts the chill plate solidification begins with the formation of equi-axed grains. Subsequently the

grains begin to grow vertically in the preferred [001] orientation. The vertical growth of columnar grains is promoted by a thermal gradient (G) maintained by the baffle and by withdrawing the mould vertically from the hot chamber at a velocity (V). The thermal gradient G and withdrawal velocity V are critical in the formation of columnar grained material (Fig. 2.7).

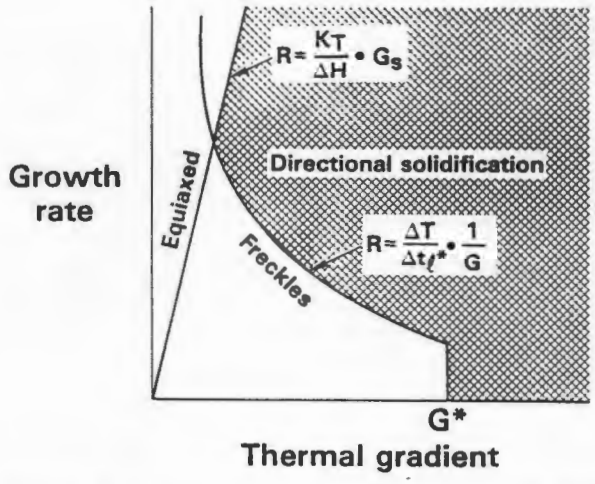

Figure 2.7. The effect of growth rate R and thermal gradient G on the formation of DS material. (Ref. 27)

If the ratio G/V falls below a certain value equi-axed grains will develop, i.e. the boundary conditions for DS casting may be demarcated firstly by the relationship:

$$R = K_t G/\Delta H \qquad (2.2)$$

where R is the solidification rate, K_t is the thermal conductivity of the solid and ΔH is the heat of solidification[27].

Freckle formation is the other boundary condition. This defect is brought about by the segregation of Al and Ti to the interdendritic liquid during casting. Consequently the liquid has a relatively low density and may rise in jets, breaking off dendrite tips in the process. The dendrite tips act as nuclei for equi-axed grains which then grow, defeating the purpose of the DS process. The boundary condition of freckle formation may be expressed as:

$$R = (\Delta T/\Delta t).(1/G_m) \qquad (2.3)$$

where ΔT is the temperature difference between the liquidus and solidus, Δt is the time for the mushy zone to pass a point in the casting (local solidification time) and G_m is the thermal gradient in the mushy zone[27]. Alloy chemistry can play an important role in freckle formation; for example, substituting Ta for W can reduce the likelihood of freckle formation since Ta segregates to the liquid and evens out the density differences. A more detailed description of the DS casting procedure may be found in reference 44.

2.6 Solidification Effects on the Microstructure of Nickel-base Superalloys

The solidification process has a profound influence on the microstructure and distribution of phases in superalloys. Segregation behaviour and the nucleation and growth characteristics of the phases are of particular importance. Under most conditions the phases are found in a dendritic structure which arises from industrial casting conditions. The dendrites are composed principally of the fine (<0.1μm) γ' precipitates enclosed in the γ matrix. On the periphery of the dendrite arm, as one moves from the dendrite core to the interdendritic zones, carbides may be found with either a Chinese-script or blocky morphology. A larger γ' precipitate may also be found in these regions (reference 45, for example). Within the interdendritic zone a eutectic γ-γ' phase composed of rosette shaped or blocky γ' precipitates may be found together with carbides. The development of this typical phase distribution is closely related to the solidification behaviour of the alloy.

2.6.1 Carbide Formation

As a generalisation, the process of solidification may begin with the formation of a dendritic front composed of γ, at temperatures in the region of 1300°-1400°C. Ahead of the dendrite tips, in the liquid zone, carbides may form[45,46,47]. These carbides are either driven ahead into the liquid zone by the solidification front or they may be engulfed within the dendrite, leading to the final location on the periphery of the dendrite or within the interdendritic zone. As solidification proceeds, these carbides in the liquid grow by Ostwald ripening, leading to the

large blocky or script carbides seen in the alloys. The thermal gradient (G) and the withdrawal velocity (V) may have an effect on the carbide morphology, as illustrated in Fig. 2.8. Carbides of different composition may develop by solid state reaction within the dendrites[45,47].

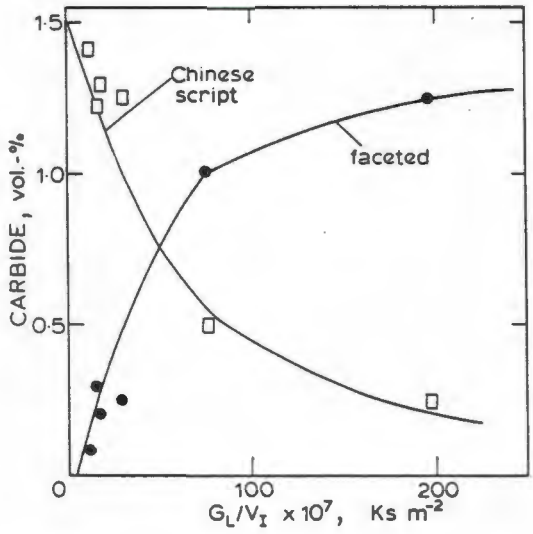

Figure 2.8. Volume fraction of Chinese script and blocky carbides as a function of G/V for DS IN-100 (Ref.47).

2.6.2 Eutectic γ-γ' and γ' Formation

As solidification proceeds, the dendrites solidify as γ, with the rejection of various solutes into the liquid zone. Investigation into the alloys MarM-002, MarM-200, MarM-247 and others indicate that elements such as Al, Ti, Ta, Mo and Hf tend to segregate to the interdendritic regions[30,48,49,50]. Cobalt segregates mainly to the dendrites but the behaviour of chromium and tungsten appears to depend on alloy composition[48]. The partitioning of the solutes leads to compositional differences between the dendrite core and the dendrite arm periphery and subsequent differences in γ' characteristics. The enrichment of γ' formers (Al, Ti, Ta) in the dendrite outskirts caused by solute rejection leads to the formation of the large primary γ' in these regions during subsequent cooling. Conversely, the dendrite cores contain relatively less γ' formers and hence the γ' precipitates that form are smaller. Further segregation in the final liquid zones leads to the formation of a eutectic composition and abrupt solidification in these regions with the formation of the rosette or blocky eutectic γ-γ'.

2.6.3 Solidification in MarM-002

Viatour et al[51] and Wills et al[48] measured the solidus of MarM-002 at temperatures of 1330°C and 1369°C respectively. The reasons for the discrepancy are unclear, but may be related to subtle compositional differences in the materials studied, as well as differences in the casting procedure and in the measuring techniques (directional solidification, thermocouple in the melt for Wills et al[48] and conventional casting and DTA for Viatour et al[51]).

Wills et al[48] found that carbides formed only in the liquid zone at temperatures below 1347°C and that the eutectic phase formed at 1254°C. On the other hand, Viatour et al[51] measured the liquid zone carbides to form at 1210°-1300°C and found the eutectic to form at 1180°-1220°C. They concluded that carbides formed within the dendrites at temperatures of 1325°-1375°C.

Despite these discrepancies there appears to be agreement that the solidification of MarM-002 proceeds by solidification of γ dendrites followed by the formation of carbides in the liquid phase, and terminates with the formation of the eutectic γ-γ'. Carbides may form in the dendrites prior to the liquid phase carbides by solid state transformation.

Thus the microstructure of MarM-002 consists of fine γ' within the dendrite cores and, depending on the individual casting conditions (solute rejection behaviour, temperature gradient, mould withdrawal rate etc.), there may be a coarser γ' on the dendrite arm periphery. The coarser γ' develops because of solute enrichment in these areas. Carbides are found in the interdendritic areas and are either blocky (Ta, Hf) MC carbides or Chinese script (Ta, Ti) MC carbides[52]. These carbides form in the liquid melt and are driven into interdendritic areas by the solid dendrite front. The carbides may decompose to M_6C carbides and a small, blocky Hf-rich MC carbide during heat treatment[52].

2.7 Strengthening Mechanisms in Nickel-base Superalloys

The strengthening mechanisms of superalloys are solid solution strengthening and precipitation hardening. Precipitation hardening in these alloys is primarily a function of the volume fraction, size and strength of the particles. Each

precipitate provides strength primarily through coherency strains and the existence of order. The stacking fault energy (SFE) , anti-phase boundary (APB) energy and differences in elastic moduli between γ and γ' also influence the deformation behaviour. A summary of the strengthening mechanisms follows below.

2.7.1 Solid Solution Strengthening

The contribution to solid solution strengthening by several elements is tabulated in section 2.2.1, but in a generalised form[53] may be expressed as :

$$\tau_c = \tau_o + (G\varepsilon^{4/3}c^{2/3}) / 550 \qquad (2.4)$$

where τ_c is the stress the dislocation is under, τ_o is the critical resolved shear stress of the pure metal, G is the shear modulus, ε is the misfit and c the concentration of solute atoms.

2.7.2 Precipitation Hardening

In precipitation hardened alloys deformation can occur through particle cutting or by the dislocation bypassing the precipitate through Orowan bowing or climb. The first phenomena, i.e. the cutting of an ordered precipitate by a dislocation, is a high energy process since an anti-phase boundary (APB) is formed. In low volume fraction alloys the contribution of order strengthening may be described as[54] :

$$\tau_c = (\gamma_o/2b) \quad [(4\gamma_o f r_s / \pi T)^{1/2} - f] \qquad (2.5)$$

where γ_o is the APB energy, b is the Burger's vector, f is the volume fraction, r_s is the precipitate radius and T is the dislocation line tension.

In alloys with a high volume fraction of precipitates the contribution is[55] :

$$\tau_c = \gamma_o/2b - (T/br_o) + (k/2)(\tau_o + \tau_p) \qquad (2.6)$$

where τ_p is the friction stress of the particle and k is a constant. Further strengthening arises from the coherency strains surrounding the precipitates and the increase in flow stress $\Delta\tau$ may be expressed as[56] :

$$\Delta\tau = AG\varepsilon^{3/2} (r_o f/b)^{1/2} \qquad (2.7)$$
$$\text{where } 9\pi f/16 < 3\varepsilon r_o/b < 1/2$$

Dislocation bypassing may proceed through Orowan bowing, climb or some other process. The increase in flow stress ($\Delta\tau$) attributable to Orowan bowing is[57] :

$$\Delta\tau = (Gb/2\pi L)\, \phi\, \ln(L/2b) \qquad (2.8)$$

where $\phi = (1/2)[1 + 1/1 - \upsilon]$, υ is Poisson's ratio and L is the interparticle spacing.

2.8 Tensile Deformation in Nickel-base Superalloys

Two slip systems are predominant in the γ' particles, the $\langle 110 \rangle\{111\}$ system and the $\langle 112 \rangle\{111\}$ system[58]. Cube slip on {100} planes may occur at temperatures above 400°C. Slip in the ordered precipitates takes place through dislocation superpartials separated by a superlattice intrinsic (SI) stacking fault, a superlattice extrinsic (SE) stacking fault or an anti-phase boundary (APB)[59,60,61]. The superlattice intrinsic and extrinsic stacking faults are produced by slip on the $\langle 112 \rangle\{111\}$ system and APB's arise from slip in the $\langle 110 \rangle\{111\}$ system. As discussed above, increasing the fault energies will increase the difficulty with which dislocations can cut into the precipitates. An additional complex fault (CF), a superposition of SI faults and APB's results from $a/6\langle 112 \rangle\{111\}$ shear.

A startling feature of pure γ' alloys is the peak in flow stress[62] exhibited at a temperature of approximately 760°C, as illustrated in Fig. 2.9. Yamaguchi et al[60] and Paidur et al[61] have correlated the APB energies and slip characteristics with this phenomena. They determined that the APB energy is greater for the {111} plane than the {100} plane and that $a/2\langle 110 \rangle$ superpartials are glissile on the {111} plane but not the {100} plane. Since the {100} plane has a lower APB energy, cross slip to this plane from the {111} plane is always favoured leading

to the anomalous rise in flow stress. In other words, glissile dislocations on the {111} plane cross slip to the {100} plane by thermal activation, where they are sessile and act as obstacles to moving dislocations. Above the peak temperature movement of the sessile dislocations becomes possible by thermal activation.

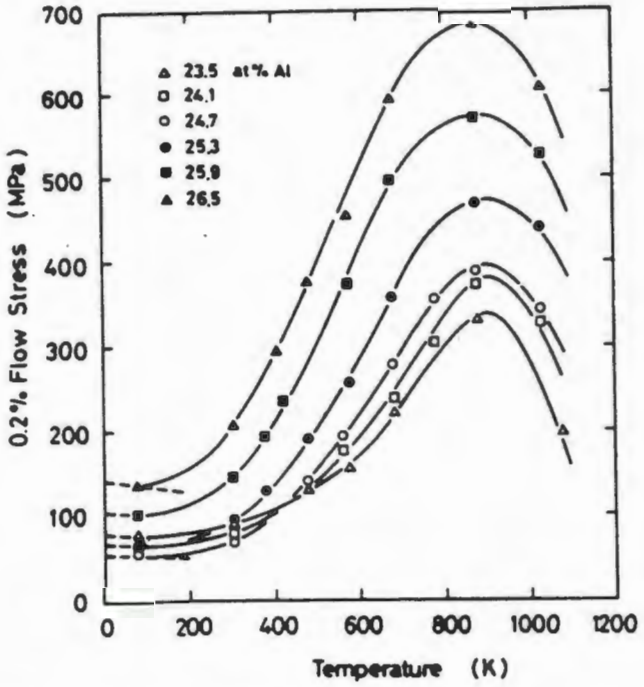

Figure 2.9. Flow stress in γ' as a function of temperature (Ref.63).

The peak in flow stress is, however, not as pronounced in two phase alloys (Fig. 2.10). Instead the flow stress remains roughly constant up to the peak temperature, above which the flow stress decreases[9,64]. In the two phase alloys deformation begins with slip in the matrix and the formation of dislocation networks at the γ-γ' interfaces[65]. The main obstacle to dislocation motion is not gliding through the γ' but entering the gamma prime[55,66]. Entry into the precipitates requires that the coherency strains be overcome and that an APB is created. Since the APB energy is relatively independent of temperature below the peak temperature, the stress required to create the APB is constant[67,68,69]. Above the peak temperature, however, the APB energy decreases and hence the flow stress decreases.

With regards to the effect of γ' characteristics on tensile behaviour, equations 2.5 to 2.7 suggest that the strength of the alloys will increase with increased volume fraction of precipitates. This effect has been confirmed in the alloys DS MarM-247 and DS CM247 LC (Ref.9). However, the effect of volume fraction is difficult to distinguish when comparing a series of alloys of different composition as well as different γ' volume fraction because of changes in coherency strains, APB energy and solid solution strengthening[70].

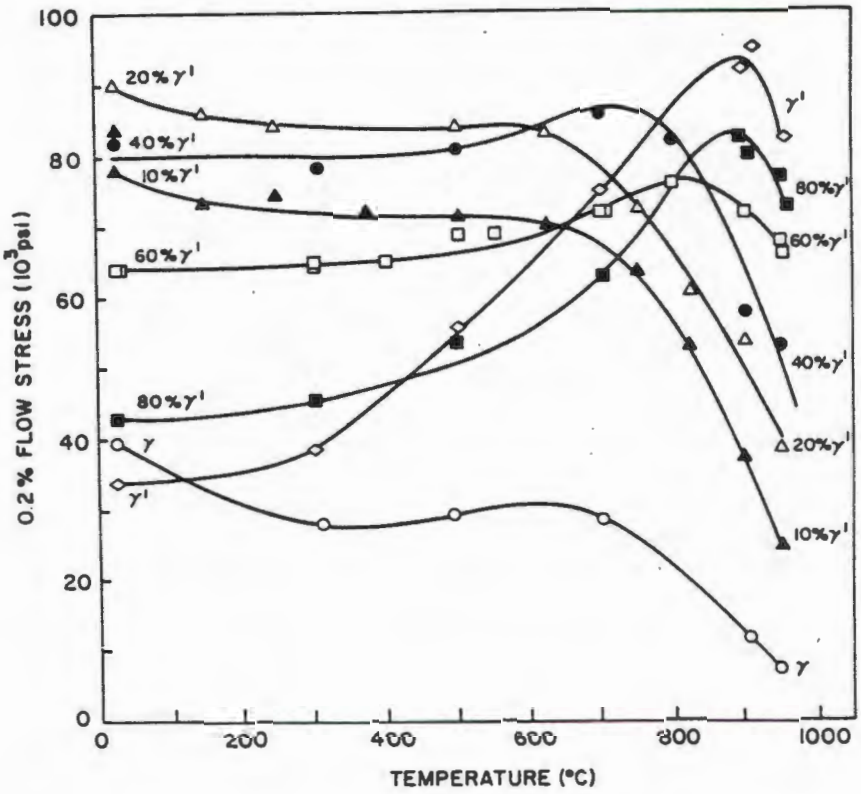

Figure 2.10. Change in flow stress as a function of temperature for Ni-Al-Cr γ-γ' alloys (Ref.64).

Gamma prime size does have an effect on tensile behaviour since the shear of γ' surfaces is a rate controlling step. Below the peak temperature of 760°C there is an inverse relationship between γ' size and yield strength (Fig. 2.11). The smaller the γ' size the greater the number of γ-γ' interfaces resisting shear and the greater the strengthening effect[71]. Above the peak temperature thermal activation of dislocations occurs and the tensile strengths decrease with increased temperature.

The presence of the γ-γ' eutectic reduces ductility due to slip bands impinging the phase and producing localised shear and premature failure[72]. Studies of the alloy PWA-1480 indicate that the yield strength is not affected by the presence of the eutectic, but when the eutectic is dissolved the ultimate tensile strength is seen to rise. Thus it appears that the eutectic γ-γ' initiates early failure in the material. Carbides are associated with failure in MarM-200 for similar reasons[73]. Porosity, however, did not appear to affect the tensile properties in PWA-1480 although it is well known that porosity leads to failure under fatigue conditions[74].

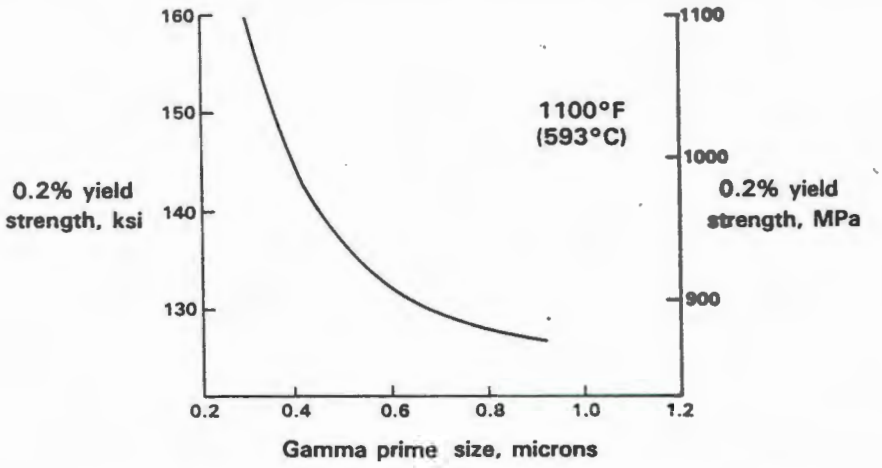

Figure 2.11. The effect of γ' size on the yield strength of PWA-1480 (Ref.27).

2.9 Creep Deformation

Creep may be defined as the plastic deformation of a material under constant load with the passage of time. This may take place at room temperature in the case of lead alloys or at elevated temperatures of 760°C and over for nickel-base superalloys. The mechanisms of creep are complex, but for simplicity one may examine the work of Sherby and Burke[75] who identified three categories of deformation mechanisms operating at low, intermediate and high stresses. At low stresses there is a linear relationship between the steady state creep rate and stress, such that $\dot{\varepsilon} = K_1 \sigma$ where K_1 is a constant. The deformation mechanism is primarily one involving the diffusion of vacancies from transverse

grain boundaries to longitudinal grain boundaries, either through volume diffusion (Nabarro-Herring creep) or through grain boundary diffusion (Coble creep).

At intermediate stresses the power law of creep is dominant, i.e. $\dot{\varepsilon} = K_2 \sigma^n$ where K_2 and n are constants. Deformation occurs through the processes of dislocation glide and climb, and recovery processes (e.g. dislocation annihilation, recrystallization) are slow in comparison with the dislocation glide. At high stresses, $\dot{\varepsilon} = K_3^m \exp(A\sigma)$, where K_3, m and A are constants. Deformation again proceeds through dislocation glide and climb, but the recovery processes are rapid, leading to the formation of a steady state dislocation structure.

In practice only dislocation creep is of importance in the creep behaviour of nickel-base superalloys. The operating conditions under which diffusional creep occurs is rarely applicable to the real-life usage of superalloys and hence will be discussed no further, but the dislocation mechanisms operative in superalloys will be discussed in a later section.

A typical creep strain-time curve (Fig. 2.12) consists of four regions; an incubation period (I) exhibiting no apparent strain with the passage of time, a region of steadily decreasing strain rate known as primary creep (II), a linear region known as secondary creep (III) and the region of tertiary creep (IV) comprised of a steadily increasing strain rate followed by failure.

Simplistically, the creep stages may be regarded as being controlled by the processes of dislocation work hardening and dislocation climb and annihilation. Thus the primary creep stage may be regarded as being dominated by the process of dislocation formation and work hardening, leading to the steadily decreasing creep rate, while the linear secondary stage may be considered as a region where the process of dislocation formation and work hardening are balanced by dislocation climb and annihilation. The tertiary stage of creep has been attributed to the accelerated strain due to necking, microstructural instability and cavity formation. It should be noted that in reality all three stages of creep deformation are not necessarily displayed by materials and one or more stages may be absent.

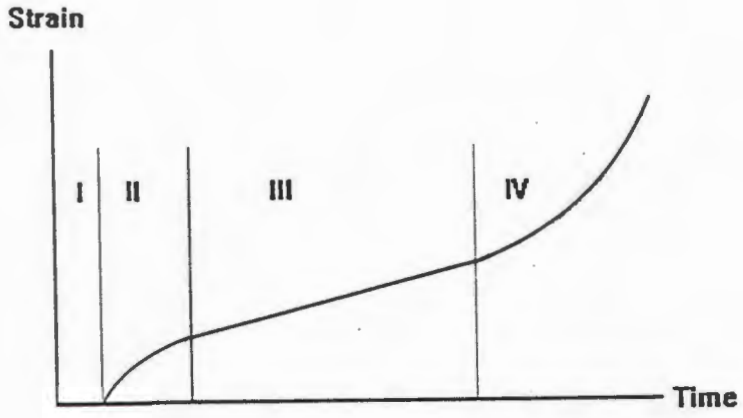

Figure 2.12. The classical creep curve consisting of primary, secondary and tertiary creep stages.

2.10 Creep Deformation of Nickel-base Superalloys

The primary, secondary and tertiary stages of creep, and occasionally the incubation stage, have been observed in superalloys over a range of temperatures from 760°C to 1038°C, and the deformation behaviour occurring within the material has been correlated to each creep stage in a number of studies[76,77,78,79,80,81].

2.10.1 Incubation Period

A review of the existing data indicates that during the incubation period a process of dislocation nucleation from a small number of sources occurs. The length of the incubation time has been shown to decrease with increasing temperature, indicating an activation energy process[82]. Deformation proceeds largely through ⟨110⟩{111} slip in the matrix of the material, but at high stress levels (about 760°C / 750MPa for alloys CMSX-2 or SRR-99) the γ' precipitates are sometimes cut by ⟨112⟩{111} dislocation pairs, separated by superlattice intrinsic stacking faults[80].

2.10.2 Primary Creep

During primary creep, dislocations begin to percolate through the material by cross slip and climb until a steady state dislocation network is formed surrounding the γ' precipitates[76-82]. The duration of primary creep is, therefore, the time required to form the dislocation network throughout the material. Deformation is largely confined to the matrix but again at high stress levels precipitate slip by the ⟨112⟩{111} systems may occur[77-80,83].

2.10.3 Secondary Creep

The formation of the steady state dislocation network signals the start of the secondary creep stage where deformation occurs homogeneously throughout the cross section of the material. At low stresses deformation is restricted to the matrix phase (e.g. 850°C / 552 MPa for CMSX-3) and occurs via the passage of (a/2)⟨110⟩ dislocations travelling on {111} planes. Pollock and Argon[84], using finite element analysis, calculated that in an alloy with negative γ-γ' misfit the resolved shear stress is much greater in the matrix than in the γ' precipitate, and hence, may not be sufficient for precipitate shear. Further, under a tensile load the stress in the horizontal γ channels was calculated to be greater than in the vertical channels, and thus explains the observed tendency of dislocations to move preferentially into horizontal channels in the initial stages of creep. At higher stresses precipitate shear occurs by (a/2)⟨110⟩ dislocation pairs in this stage of creep.

2.10.4 Tertiary Creep

Finally, during tertiary creep the strain build-up within the material causes widespread precipitate cutting and work hardening, leading to final fracture initiating from voids, eutectic γ-γ' regions, sites of incipient melting or brittle phases[52,77,85].

2.11 The Effect of Microstructure on Creep Behaviour

The creep life and strain rate within each creep stage is dependent on the microstructure of the alloy in question and hence the phases present. The γ'

size, shape, volume fraction and distribution, the γ solid solution strengthening, matrix-precipitate misfit, stacking fault energy and anti-phase boundary energy, as well as carbide characteristics and eutectic γ-γ' distributions appear to be the most important factors affecting creep behaviour. A brief discussion of some of these factors is presented below.

2.11.1 Precipitate Volume fraction

Resistance to plastic deformation may be enhanced by increasing the volume fraction of precipitates, thereby increasing the number of dislocation obstacles. The volume fraction of γ' may be increased by alloy composition design or in certain cases, by an improved heat treatment. Alloy design and evolution has seen the increase in γ' volume fraction in successive generations of superalloys. For example, the volume fraction has increased from 40% in IN-738 to 60% in the polycrystalline superalloy MarM-002 and to approximately 65 to 70% in the more recent single crystal superalloys[8,86,87] .

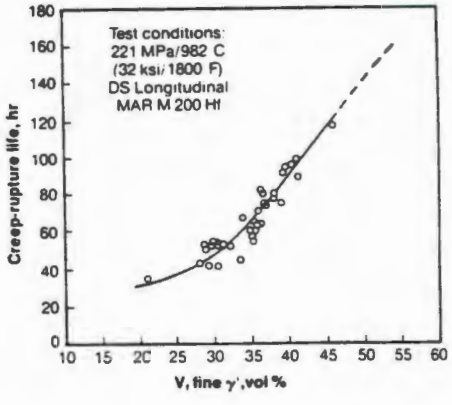

Figure 2.13. The Effect of Volume Fraction of Fine γ' on the Creep Life of DS MarM-200 + Hf (Reference 88)

The volume fraction in each alloy may be increased by optimising the heat treatment; Jackson et al[88] used a higher solution treatment temperature to dissolve the eutectic γ' and the large primary γ' in the alloy MarM-200 + Hf. This increased the volume fraction of the fine γ' from 30% to 45% and enhanced the creep life three-fold (Fig. 2.13). A second ageing heat treatment in the alloy SRR-99 at 870°C after the first 1050°C age has led to the increase in volume

fraction of γ' through the diffusion of γ' formers out of the matrix and into the precipitates, thereby resulting in increased creep lives[77].

2.11.2 Precipitate Size, Shape and Distribution

The size, shape and distribution of the γ' precipitates are factors which have a considerable effect on mechanical properties. Optimum gamma prime size varies according to the alloy studied; for example, Caron et al[79] reported that a γ' size of 0.45 μm yielded optimum results in the alloy CMSX-2, while Cetel and Duhl[8] investigated the alloy PWA-1484 and reported that a γ' cube size in the region of 0.25 to 0.35 μm resulted in optimum creep-rupture lives. Nathal[89], studying the effect of initial γ' size on the creep properties of two superalloys with compositions similar to MarM-200 and reviewing the work of other researchers, found that the optimum γ' size is dependent on the γ-γ' mismatch (Fig. 2.14). Where mismatch is greater than 0.5% an optimum size in the region of 0.1 μm was noted. If mismatch is between 0.1% and 0.5% the optimum size is approximately 0.45 μm. At levels of mismatch below 0.1% there is a weak dependence of creep life on γ' size, with the optimum size being 0.9 μm. The effect of mismatch on the optimum γ' size is attributed to several factors. Firstly the mismatch affects the size at which precipitates change from a spheroidal to cuboidal structure, hence affecting the size at which a well aligned cuboidal dispersion of γ' is obtained (this will be discussed in the section on γ' rafting below). Secondly the misfit influences the strength of the matrix-precipitate interface through both coherency strains and the misfit dislocations which develop at the interface. The greater the misfit the finer the dislocation network which then impedes shearing of the γ'.

It has been noted, however, by Caron and Khan[78] that in single crystal alloys the dependence of creep properties on γ' size is affected by the orientation of the crystal. Crystals of CMSX-2 grown in the [111] direction had an improvement in creep life as the γ' size decreased from 0.45 μm to 0.23 μm, whereas crystals in the [001] direction had improvements in creep life as the γ' size increased from 0.23 μm to 0.45 μm. With regard to the [001] single crystals, the 0.23 μm γ' size was associated with a decreased interparticle spacing between the γ' particles, thus hindering the Orowan bypassing mechanism. Precipitate shear by the passage of a/3 [112]{111} superpartial dislocations was then the dominant

deformation process. This deformation was localised and intense, resulting in high primary creep strains and increasing the effective stress during secondary creep. With a γ' size of 0.45 μm, Orowan bypassing of the precipitates was possible, thus permitting homogeneous [110]{111} slip in the matrix. The result was a low steady state strain rate.

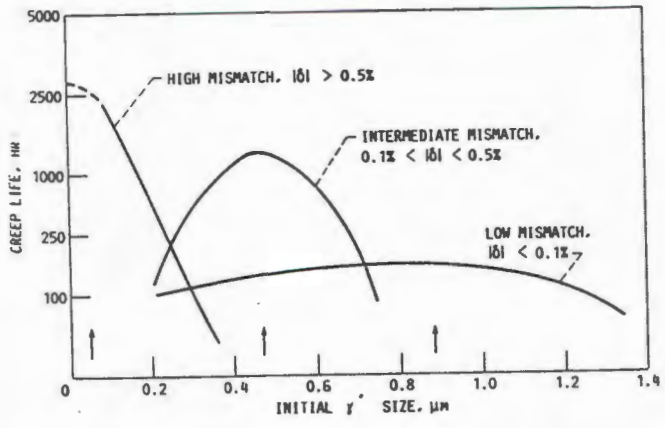

Figure 2.14. The effect of initial γ' size and misfit on the creep life of superalloys (Reference 89).

In the [111] single crystals the resolved shear stresses for both slip systems are always less for the [111] orientation. Hence the [111] crystal containing 0.23μm precipitates was subjected to a lower resolved shear stress than the [001] crystal and displayed a longer life. In the [111] crystal with the larger 0.45 μm γ', only the primary (111) slip plane was activated, resulting in heterogeneous deformation with little work hardening. Large primary creep strains and high secondary creep rates resulted.

2.11.3 Gamma Prime Rafting

A striking feature of nickel-base superalloys is that extended exposure to stress and high temperature coarsens the γ' with an accompanying change in shape to a lamella or raft. In materials with a negative γ-γ' misfit, the rafts form perpendicular to the tensile stress axis, but in positive misfit alloys the raft direction is parallel to the tensile stress axis[84]. This is attributed to the different stress states arising in the two different situations, i.e. in negative misfit alloys the pressure in the horizontal γ channels becomes positive and the pressure in

the vertical channels is negative[84]. Preferential stress assisted dissolution of γ formers occurs in the vertical channels and the elements diffuse to the horizontal channels, resulting in an increased γ thickness. Conversely, γ' formers dissolve in the horizontal channels and diffuse to the vertical channels, resulting in precipitate coalescence[84,90]. The reverse situation would occur with positive misfit alloys.

The raft formation may occur within a short space of time under conditions of high temperature and/or high stress and may be related to the initial formation of dislocations during the creep deformation. It appears that the dislocations act as vacancy sources and sinks as well as element conduits. The time required for rafting has been related to the diffusion of W, often the slowest diffusing element, in nickel[84]. Rafting has been shown to begin during the primary creep stage and is fully developed well into the secondary creep stage[71,91,92,93].

The perfection of the γ' lamellae plays an important role in the deformation behaviour of the material. A well aligned distribution of γ' rafts contains a large number of γ-γ' interfaces that present obstacles to dislocation climb and thus retard the deformation process[78,87,89,93]. Precipitate shear is then the operative deformation mode but is more difficult; firstly requiring that the dislocation passes through the dislocation network surrounding the precipitates, secondly the dislocation must transform from a single to a paired state as it travels through the precipitate, and thirdly the leading dislocation leaves an anti-phase boundary in its path. An imperfectly aligned rafted γ' distribution presents many more γ channels, thus facilitating dislocation climb.

The perfection of the distribution of γ' lamellae is dependent on the initial distribution and size of the precipitates (Fig. 2.15). Cuboidal precipitates situated shoulder to shoulder will coalesce to form more perfectly aligned rafts and present more obstacles to dislocation climb[78]. Unevenly sized precipitates with a morphology varying from spheroidal to cuboidal are less inclined to form aligned rafts.

Thickening of the rafts with the passage of time in the secondary creep stage has been seen in the single crystal superalloy NASAIR 100 (references 92, 93), but not in a Ni-Al-Mo-Ta model alloy studied by MacKay and Ebert[71,91]. The

latter have suggested that shear in γ' rafts promotes thickening by providing growth sites at shear ledges on the γ' surface. The higher mismatch in the model alloys would, however, inhibit shear to a greater degree since the misfit dislocation structure at the γ-γ' interface is finer. Additionally, there is slower diffusion in the model alloys as the refractory metal content is higher .

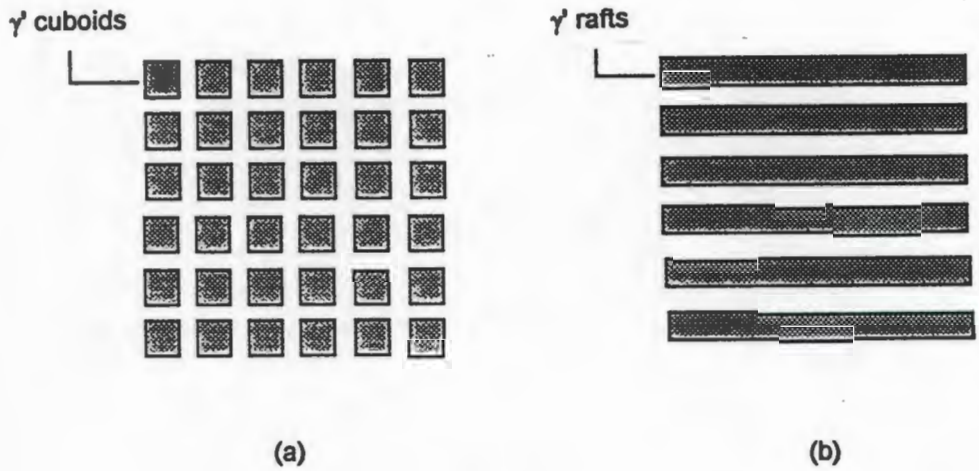

Figure 2.15. a) A well aligned distribution of cuboidal γ' leads to (b) well aligned γ' rafts

Large scale coarsening of the rafts may be associated with the onset of tertiary creep[92,93] but this is inconclusive and may be restricted to certain alloys. MacKay and Ebert[71,91] report that raft thickening occurred only after the onset of tertiary creep and only under high stress conditions (234 MPa and 179 MPa for temperatures of 982° and 1038°C respectively). No thickening was reported at low stress conditions (186 MPa and 147 MPa for the above temperatures). The reasons for this behaviour are unclear but may be related to the influence of shear ledges and stress assisted diffusion.

2.11.4 The Effect of the γ-γ' Eutectic on Creep Behaviour

Jackson et al[88] has shown that the presence of the eutectic γ' may be regarded as "tying up" precipitates which could be used as more effective strengthening γ' if it was redistributed as a finer precipitate below about 0.5μm in size.

The eutectic γ-γ' may also be regarded as a region of weakness, leading to final fracture in the material under creep conditions[52,85]. Final failure in this case is attributed to the formation of internal cavities at these regions and the linking up of these cavities.

2.11.5 The Effect of Carbides on Creep Behaviour

In polycrystalline superalloys, carbides have been regarded as grain boundary strengtheners. Discrete particles of carbides of either the MC, M_6C or $M_{23}C_6$ type act as "keys", pinning the grain boundaries in position. However, if a continuous film of carbide forms along the grain boundaries, premature intergranular fracture may occur. A further potential danger of carbides is that poor casting control may result in the formation of carbides with cracked surfaces, thus promoting cavitation during creep[94].

3. Materials

MarM-002 is an alloy designed for polycrystalline use in high temperature turbine applications, used mainly by Rolls-Royce. In this study, MarM-002 was received in both conventionally cast (CC) and directionally solidified (DS) forms. The nominal composition of MarM-002 is given in Table 3.1. The actual composition is given in Appendix I. Heat treatment and metallography was performed on both the CC and DS alloy, but mechanical testing took place only with the DS material. The CC MarM-002 was received in the as cast condition, but the DS MarM-002 had been previously heat treated at 1220°C/2h and quenched by an argon gas fan (GFQ). The heat treatment served to stress relieve the DS material, thus preventing recrystallization during subsequent rough handling or exposure to heat. Additionally, the heat treatment was supposed to serve as a partial solution heat treatment, but as will be seen in section 5.2 , the temperature was not high enough for full precipitate dissolution and the quench rate was not rapid enough to prevent the formation of γ' precipitates on cooling. The microstructures of the as cast CC and as received DS materials will be discussed in sections 5.1 and 5.2.

Element	Composition (wt%)
Ni	60
Al	5.5
Ti	1.5
Ta	2.5
Cr	9.0
Co	10.0
W	10.0
Hf	1.5
Zr	0.05
B	0.015
C	0.14

Table 3.1. The nominal composition of MarM-002

4. Experimental Approach

4.1. Heat Treatment

Heat treatment of the materials was carried out in a vacuum furnace under either an argon atmosphere for solution heat treatments or a vacuum of 10^{-4} torr for the ageing heat treatments. The argon atmosphere was used to prevent the loss of Al or Ti from the alloy at the high solution treatment temperatures, but was also found to result in minor surface oxidation, possibly due to impurities in the gas. In the argon atmosphere heat treatments, a vacuum of 10^{-4} torr was attained prior to the introduction of argon into the furnace. Ageing heat treatments were conducted under vacuum, since the specimens used for mechanical testing were machined prior to the ageing treatment and the final dimensions would have been altered by oxidation. The temperature was monitored by a Type R platinum-13% rhodium thermocouple and the furnace was controlled by a Eurotherm controller.

4.1.1. Solution Heat Treatment

The solution heat treatment was performed in accordance with two concepts. The first involved the conventional heat treatment procedure of heating at the maximum heating rate to a dwell temperature of 1220°C and a dwell time of two hours. As will be seen in later sections this heat treatment does not dissolve all of the γ'.

The second procedure involved heat treatment at 1220°C, 1240°C and 1260°C, using a process known as the Varied Rate Solution Heat Treatment (VRSHT), postulated by Ault[95]. The VRSHT is illustrated in Fig. 4.1 and may be regarded as a technique which permits maximum γ' dissolution without incipient melting. The process consists of heat treating at a series of constant heating rates to several successively higher temperatures (T_1, T_2, T_3, T_4 in Fig.4.1). As seen in the illustration, the temperature is always maintained below the incipient melting temperature, represented by the dashed line. The incipient melting temperature increases as the heat treatment progresses since segregation is reduced by diffusion and low melting point phases decompose to more stable phases. The

benefit of the VRSHT is that the maximum temperature is maintained without melting, thus providing the maximum energy for diffusion and solid state reactions. Additionally, the VRSHT decreases the homogenisation time compared to heat treatments using dwell periods at intermediate temperatures. Establishing the VRSHT for any material involves measuring the incipient melting curve for the alloy and heat treating below those temperature-time points. This is done through repetitive heat treatment-microstructure studies and was performed for MarM-002 in this study.

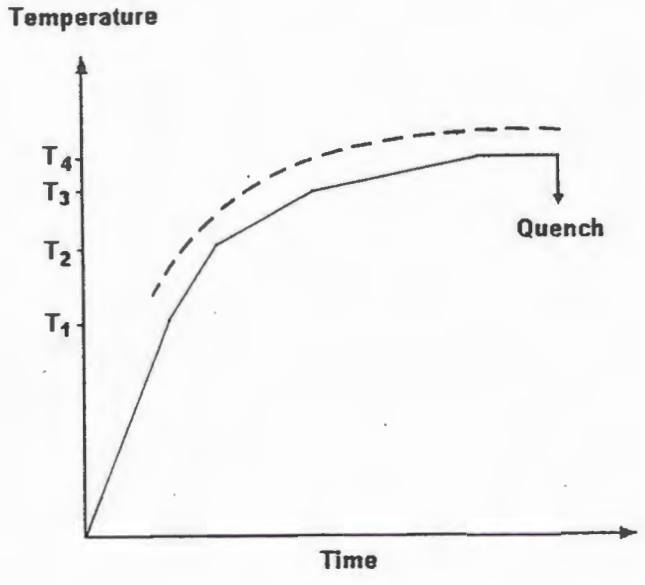

Figure 4.1. The Varied Rate Solution Heat Treatment (VRSHT) depicted on a time-temperature graph. The dashed line represents incipient melting and the solid line indicates the heat treatment schedule used.

The "target" temperatures selected (represented by T_1, T_2, T_3, T_4 in Fig.4.1) were 20°C increments above 1180°C. The heating rates were determined by a trial-and-error process, which involved heating to the target temperature at an arbitrary rate. If the resulting specimen showed signs of incipient melting the heating rate was reduced and the experiment repeated until eventually no melting was detected in the specimen. The procedure was then repeated for the next target temperature. It is demonstrated in section 5.5 that the maximum solution temperature attained using the VRSHT for MarM-002 was 1260°C. However, in order to compare the benefit of solution treatment temperatures, varied rate solution heat treatments terminating at 1220°C and 1240°C, as well

as at 1260°C, were used. Irrespective of the solution temperature, a dwell period of two hours was used at the solution temperature. In the following sections of this dissertation, the specimens will be referred to by the solution treatment that they have undergone. For example, the VRSHT 1220°C specimen will have undergone solution treatment at 1220°C using the VRSHT, and the 1220°C/2h specimen will have been "conventionally" solution treated at 1220°C for two hours.

In order to determine the effect of the solution heat treatment on the microstructure, the metallographic specimens were water quenched following the solution treatment. This allowed the microstructure to be "frozen" in place, but also caused quench cracking. Quench cracking was not acceptable in the specimens prepared for mechanical testing and the "freezing" of the microstructure was not necessary; therefore an argon gas quench was used for these mechanical test specimens following the solution treatment and ageing treatments.

4.1.2. Ageing Heat Treatments

An ageing heat treatment of 1050°C/12h + 870°C/16h was used for all of the mechanical test specimens. The 1050°C step simulated the coating cycle applied to components, as well as serving as the primary age.

4.2. Metallography

The microstructures of specimens in the as cast condition (i.e. the CC material) and the as received condition (the DS material) were examined. The microstructures were also examined after both solution treatment and ageing, as well as after mechanical testing.

When studying the effect of the solution heat treatments on the microstructure of the materials, the metallographic specimens of the conventionally cast MarM-002 were cubic in shape with a cube length of approximately 10 mm. The specimens of the DS MarM-002 were cut from the runners of the tensile and creep test specimens and were approximately 10 mm in diameter and 15 mm in

length. The microstructure parallel to the columnar grains was studied for the DS material.

The materials were prepared according to conventional metallographic techniques, being initially ground on silicon-carbide paper and mechanically polished with a final diamond paste of 0.25 μm. An electrolytic etchant composed of 10% phosphoric acid - 90% water was used under conditions of 2V, 0.2 A/cm^2 for 10 seconds. The etchant attacked the γ matrix, leaving the γ' and carbides standing proud. The specimens were examined by both light microscopy and scanning electron microscopy (SEM). For electron microscopy, a mixture of predominantly backscattered and secondary electrons was used for imaging, under an accelerating voltage of 30 kV. This relatively high voltage was used to maximise the back scattered electron yield. The mix of electrons was found to be beneficial for the identification of phases and the incipient melting sites. This is due to the atomic compositions and surface topography of the various phases. The gamma prime precipitate, for example, has a high concentration of the relatively low atomic mass elements Al and Ti in the superlattice, although the heavier Ta and W are also present. The matrix tends to be rich in Cr, Co and W, which are slightly heavier in atomic mass. Contrast between the two phases is enhanced because the difference in atomic mass is sufficient to produce variations in the back scattered electron yield. Topographical contrast may also play a role since the matrix is preferentially etched, leaving the gamma prime precipitates to stand proud. Because the back scattered detector has no voltage bias to attract electrons, electrons from the "taller" precipitates are more likely to be detected, thereby enhancing phase contrast. In fact it was found that a relatively severe etch was required for optimum phase identification, lending support to the importance of surface topography.

Gamma prime sizes were measured after the ageing heat treatments by the linear intercept method. The cube lengths were measured when the precipitates were cuboidal and the diameters were measured in the case of spheroidal precipitates. If the gamma prime adopted a raft (or lamellae) morphology, the raft thickness was measured. A minimum of 100 precipitates were measured for each specimen from at least three micrographs. The field of view of the micrographs encompassed an area of approximately 8 x 5 μm, where the

precipitates may vary from 0.2 μm to 1 μm in size. In some cases, therefore, there were up to 400 precipitates per micrograph.

The volume fraction of the phases (γ', eutectic and carbides) was measured from three to five light micrographs or SEM micrographs per specimen using a Joyce-Loebl image analyser. The light micrographs were used to measure the volume fraction of eutectic γ' and γ'. The field of view covered by the micrographs was approximately 200 x 290 μm for the eutectic measurements, where the width of a dendrite is about 70 μm. For the γ' analyses the field of view was 100 x 140 μm. Image analysis was more effectively performed on the light micrograph negatives than prints, since the negatives generally displayed more contrast between the phases. The volume fraction of undissolved γ' (not including the eutectic γ') was measured only in the dendritic areas and not the interdendritic regions. The field of view used for analysis covered both the centre and the outer region of the dendrite arm, since the γ' tended to dissolve to a greater extent in the centre of the dendrite arms. Analyses taken over the one area only (e.g. the centre) would therefore show a biased measurement. All confidence intervals stated in this text refer to the sample standard deviations measured by the various techniques.

Volume fraction measurements of the carbides were based on SEM micrographs, since the carbides were readily identifiable as white particles (on a grey background) and were easy to threshold. The micrographs used for carbide analysis covered areas approximately 350 x 450 μm in size, where the average dendrite width is about 70 μm.

4.3. Segregation

Casting segregation was measured in the SEM using energy dispersive spectroscopy (EDS) by measuring ten interdendritic sites and ten dendritic sites for both the as cast CC and as received DS material. All of the EDS analyses were performed at an accelerating voltage of 20 kV, working distance of 20mm and a specimen tilt of 30°. The real time aquisition period in all cases was 100 seconds. The voltage of 20 kV was found to best approximate the background radiation, which is beneficial for accurate background radiation subtraction

during the calculation of composition. The specimen tilt and working distance were chosen to provide good specimen resolution while still maximising the x-ray yield collected by the silicon detector. The detector was equipped with a beryllium window which precluded the detection of x-rays from elements with an atomic mass below sodium. This was not a serious drawback since the majority of the elements in MarM-002, apart from carbon and boron, are relatively heavy in atomic mass.

There was some overlap of the tungsten and tantalum peaks in the EDS spectra, which introduced some error into the measurement of these two elements. The remainder of the elemental peaks were well separated. A standardless semi-quantitative software routine was used to calculate the compositions. Although not strictly a quantitative process, the above procedure permits comparison of the compositions under identical conditions, which is adequate for this study.

4.4. Mechanical Testing

Mechanical testing consisted of tensile and creep testing at temperatures of 900°C under normal atmospheric conditions. The specimens were cast to near-net shape and subjected to final machining. Prior to the machining the specimens were solution treated, and after the machining they were aged. Dimensions of the specimens are illustrated in Fig.4.2. Three specimens were tested for each of the different heat treated conditions. Specimens were tested in five different heat treated conditions:

1. The as received condition
2. 1220°C/2h + 1050°C/12h + 870°C/16h
3. VRSHT 1220°C + 1050°C/12h + 870°C/16h
4. VRSHT 1240°C + 1050°C/12h + 870°C/16h
5. VRSHT 1260°C + 1050°C/12h + 870°C/16h

Following mechanical testing, creep and tensile specimens were sectioned parallel to the stress axis direction and prepared for metallographic analysis.

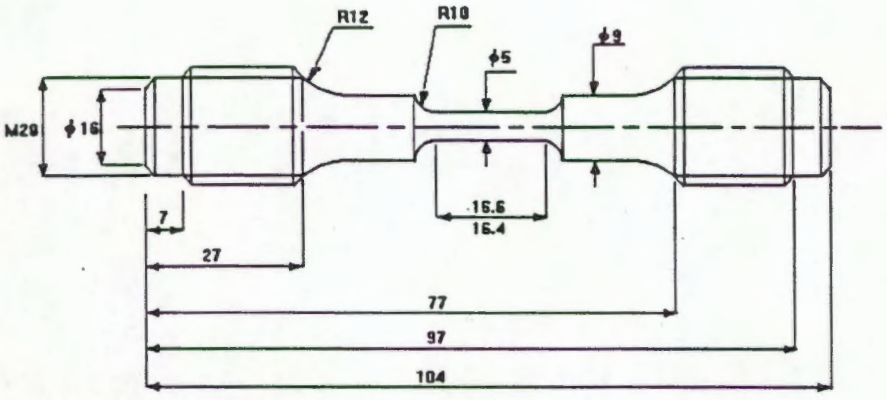

(a)

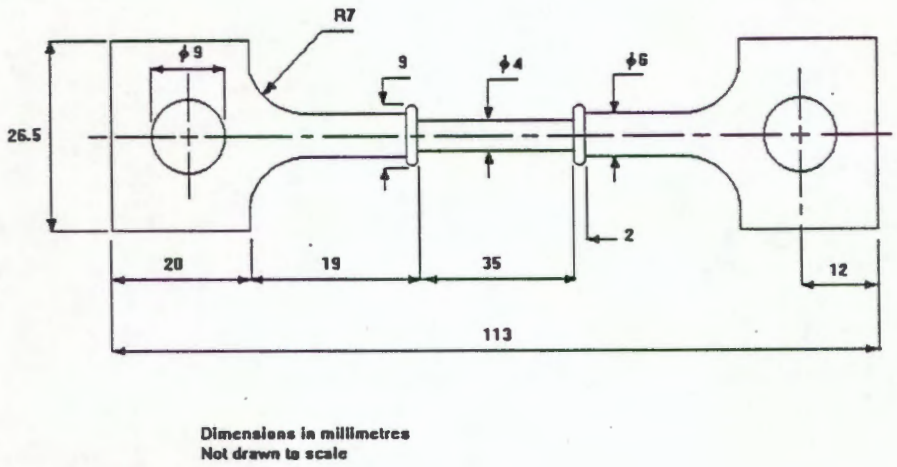

(b)

Figure 4.2. Dimensions of (a) the tensile specimens and (b) the creep specimens

4.4.1. Tensile Testing

Tensile testing took place in an Instron servo-hydraulic machine at an initial strain rate of 5×10^{-3} s^{-1}. Elongation was measured in the elastic range by

alumina extensometer arms. To prevent breakage of the brittle extensometer arms during final fracture of the specimen, the extensometer arms were removed following yield and the additional elongation was measured by the cross head displacement. Prior to testing, two dimples were spark eroded into the gauge length of the material, 12 mm apart, to provide locating dimples for the alumina arms. The load and elongation was recorded by both computer and chart recorder. The 0.2% yield strength was calculated from the chart. Following failure the elongation of the specimen was measured manually, with the aid of vernier callipers. Figure 4.3 reveals the testing apparatus immediately after the conclusion of a test.

Figure 4.3. The picture reveals the Instron servo-hydraulic machine immediately after the completion of a tensile test. The tensile testing equipment includes (A) alumina extensometer arms, (B) hinged furnace, (C) superalloy grips.

4.4.2. Creep Testing

Creep testing took place in constant load machines, under a nominal load of 300 MPa at a temperature of 900°C. The load was applied by dead weights, using a leverage ratio of 1:10. The temperature was monitored at the top, middle and bottom of the furnace hot zone and the temperature of the specimen was measured using a Type R thermocouple at the centre of the gauge length. The elongation was measured by arms attached to the ridges enclosing the gauge length of the specimen, which transferred movement to linear variable differential transformers (LVDT's). The LVDT's convert the mechanical movement of the specimen into electronic signals which are recorded by a computer. The extension was recorded every 30 minutes until final failure.

5. Results

5.1 Microstructure of the As Cast CC MarM-002

As cast CC MarM-002 has a dendritic structure (Fig. 5.1) composed of the four phases : γ, γ', eutectic γ-γ' and carbides. The carbides are visible in the SEM micrograph (Fig. 5.1) as white coloured script or blocky structures, situated predominantly at the interdendritic regions. A volume fraction of 2.0 ± 0.7 % was measured for the carbides. As discussed in sections 2.6.1 and 2.6.3, the location of the carbides arises from their nucleation and growth in the liquid melt, ahead of the dendrite tips, during the solidification of the alloy. Since the carbides are driven ahead of the solidification front, their final locations are in the interdendritic areas. It may be seen in Fig. 5.1 that carbides may, on occasion, be found in the dendrite arms. This may occur through the solidification front engulfing the carbides or the formation of carbides through solid state transformations.

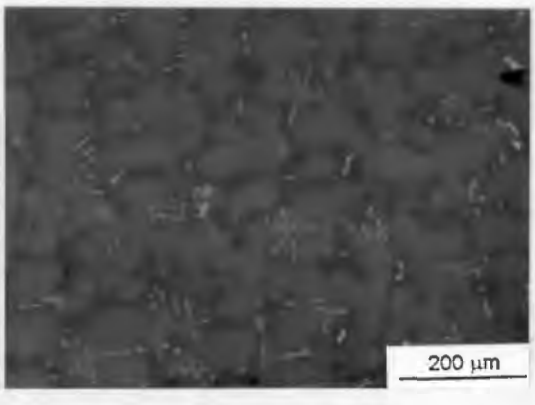

Figure 5.1. MarM-002 has a dendritic structure with the carbides visible as white particles.

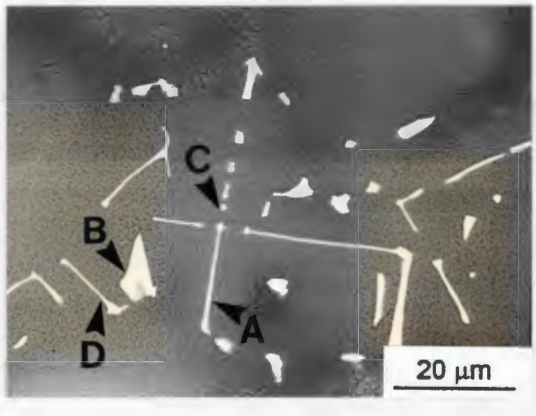

Figure 5.2. A carbide colony consisting of (A) script, (B) blocky, (C) diamond shaped and (D) arrowhead script morphologies.

Figure 5.2 illustrates a typical carbide colony in MarM-002. The morphology of the carbides may be (A) script shaped, (B) blocky, (C) diamond-shaped or (D) arrowhead-script shaped. Interconnecting script carbides are often seen with specific angles of approximately 70° or 90° between the scripts. Baldan and Benson[23] have suggested that the morphology of the carbides is dependent on

the crystallographic orientation, surface to bulk energy ratio and aspect ratio, as well as the casting conditions. They postulated that the free energy decreases as the shape changes in the series : script, short rods (lower aspect ratio), blocky and diamond shaped with edges along the ⟨001⟩ direction. Thus, the carbides adopt a preferred morphology as they decompose during the solidification process and any subsequent heat treatment. Casting conditions play a strong role on carbide morphologies and the effect of some parameters can be seen in Fig. 2.8. Composition, of course, has an effect and EDS investigation reveals that the script carbides are rich in Ta and Ti while the blocky carbides are rich in Ta and Hf; a result that supports the work of Burt et al[52]. No γ' envelopes are seen around the carbides in this condition.

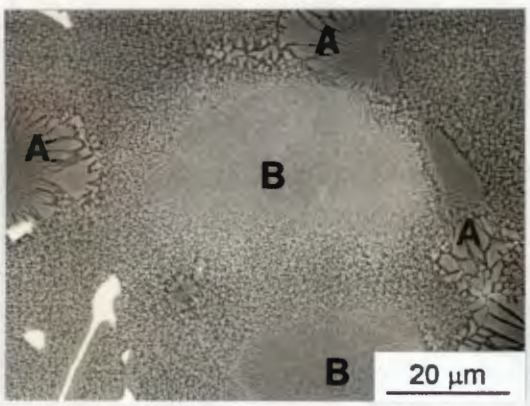

Figure 5.3. Eutectic γ-γ' is found in the interdendritic areas (A) and cuboidal γ' precipitates are found in the dendrites (B).

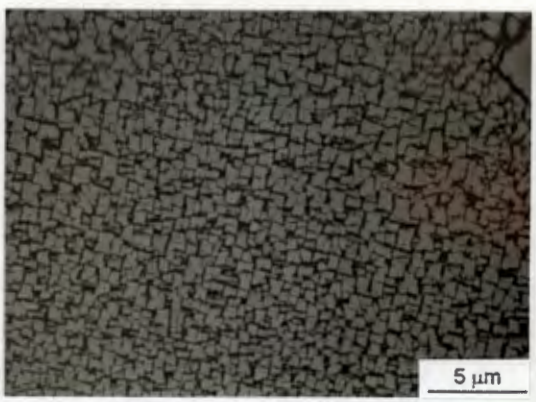

Figure 5.4. The γ' adopts a cuboidal morphology in the as cast material .

A higher magnification micrograph (Fig. 5.3) reveals the eutectic γ-γ' in the interdendritic regions and the γ' precipitates within the dendrite arms. The gamma prime precipitates are cuboidal, with a cube length in the region of 0.5 μm (Fig. 5.4). There appears to be a slight variation in size between precipitates in the centre of the dendrite and those on the outskirts. This difference results from the segregation of γ' formers to the liquid melt during solidification, as discussed in section 2.6.2. Consequently the interdendritic areas are richer in the γ' forming elements and thus the γ' precipitates in the dendrite centres are smaller than those on the periphery of the dendrite arms. Precipitates sizes varied from about 0.4 μm in the dendrite centre to approximately 0.8 μm in the

dendrite periphery adjacent to the eutectic phase. The volume fraction of γ' precipitates within the dendrites was measured at 62.5 ± 3.1 %.

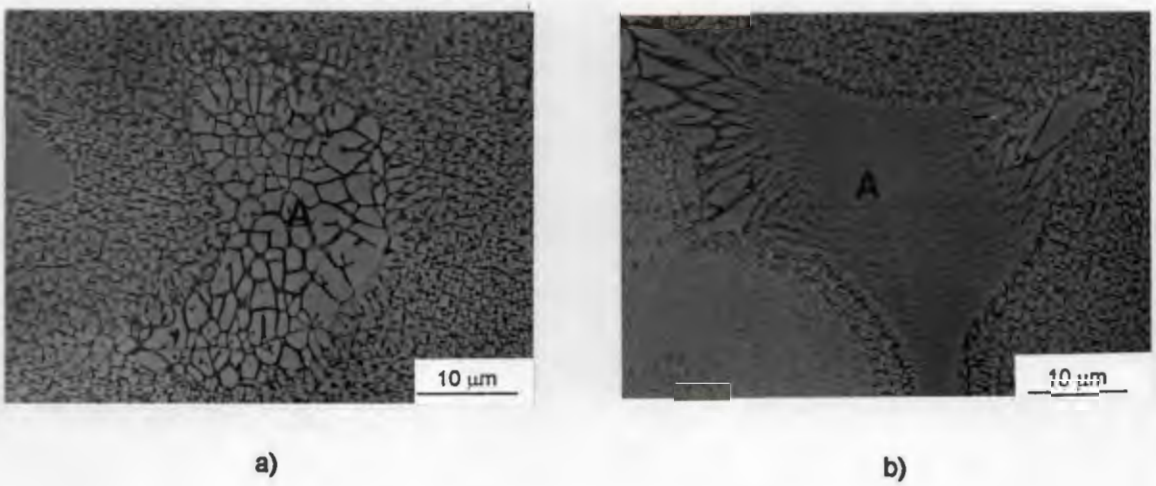

a) b)

Figure 5.5. The eutectic (A), found in the interdendritic regions, may be composed of (a) blocky γ' or (b) lamellae γ' arranged in a rosette structure.

The eutectic γ-γ' consists of either blocky or lamellae shaped γ' arranged in a rosette formation (Fig. 5.5). The volume fraction of the eutectic γ' is approximately 17.4 ± 2.0 %.

5.2 Microstructure of the As Received DS MarM-002

The dendritic structure of the directionally solidified MarM-002 has a preferred orientation arising from the casting process. The dendrites parallel and perpendicular to the growth direction may be seen in Fig. 5.6. The same phases are present in the material, although the morphologies may differ slightly from that seen in the CC alloy. The volume fraction of the eutectic γ-γ' is 15.0 ± 1.3 %, essentially the same as the CC material, and they are again composed of blocky or lamellae γ' in a rosette structure (Fig. 5.7).

However, in the DS alloy the γ' exists in two distinct forms; a large "primary" γ' that is found in the interdendritic regions and a smaller, cuboidal "secondary" γ' located within the dendrites (Fig. 5.8). The primary γ' appears to be oblong at low magnifications, but at magnifications in the region of 4000X it can be seen

that the edges of the precipitates have multiple protrusions (Fig. 5.9). This is probably due to the tendency of the gamma prime precipitates to split and form ogdoads (eight smaller cubes) linked by a central precipitate during Ostwald ripening[19,20]. The average size of the primary γ' is approximately 0.92 ± 0.27 μm. The volume fraction of the γ' in the regions composed of the primary γ' varies widely, but is approximately 51.5 ± 10.3 %.

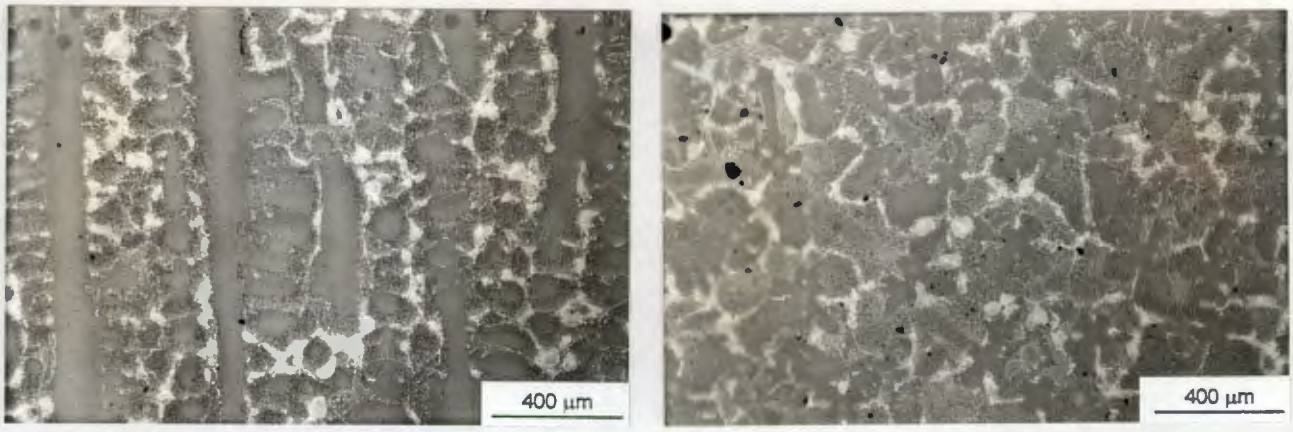

a) b)

Figure 5.6. The dendritic structure parallel (a) and perpendicular (b) to the growth direction is shown in these light micrographs.

The secondary γ' is smaller and cuboidal in shape with an average cube length in the region of 0.27 ± 0.06 μm (Fig.5.10). The volume fraction of γ' measured in the areas of the secondary γ' is about 58.2 ± 1.9 %. It may be seen in Fig. 5.10 that the precipitates are not aligned "shoulder-to-shoulder" as depicted in Fig. 2.15.

The carbides occupy a volume fraction of 2.5 ± 0.7 % in the material, and are again situated in the interdendritic region and associated with the primary γ' (Fig. 5.11). Extensive carbide colonies consisting of blocky and script carbides may be found in some regions (Fig. 5.12). Close examination reveals that most of the carbides have begun to decompose into fragments (Fig. 5.13), and in some cases the degree of fragmentation is advanced. This process is due to the stress relieving heat treatment that was applied following the casting of the alloy. Decomposition of the Ti- and Ta- rich carbides leads to the release of Ti and Ta

into the areas surrounding the carbide and the consequent formation of γ' envelopes around the carbides, since these elements are strong γ' formers. As in the CC alloy, and despite fragmentation, the script carbides are rich in Ti and Ta and the blocky carbides in Ta and Hf. Energy dispersive x-ray maps revealing the tantalum and hafnium rich blocky carbides may be seen in Fig. 5.14.

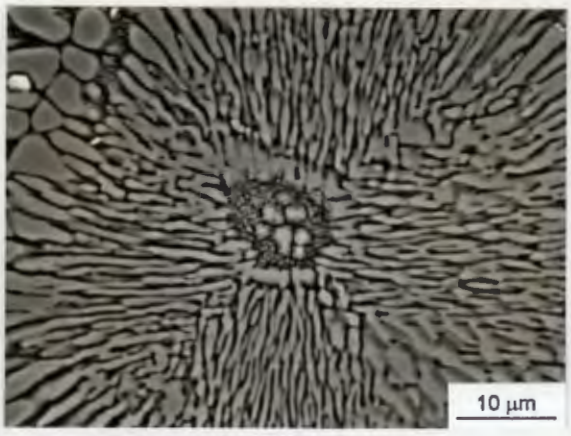

Figure 5.7. The lamellae γ' structure of the eutectic γ-γ' is shown in the characteristic rosette.

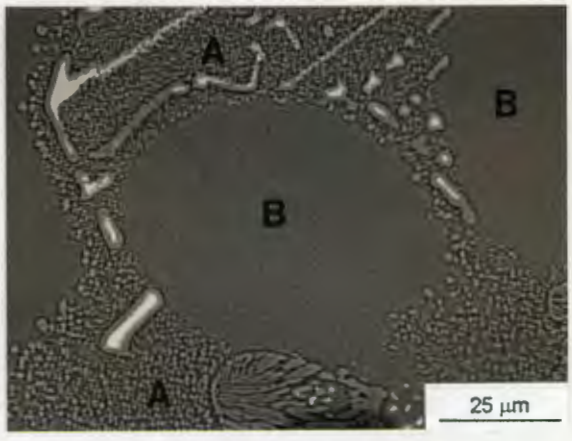

Figure 5.8. The γ' exists as a large primary interdendritic γ' (A) and a smaller γ' in the dendrite (B).

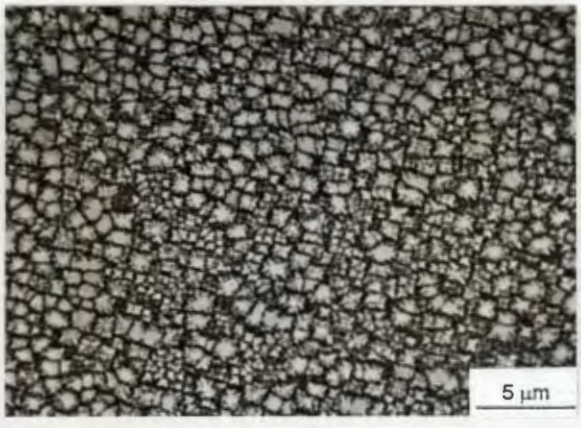

Figure 5.9. The primary γ' has a shape that is reminiscently "ogdoadal" and oblong.

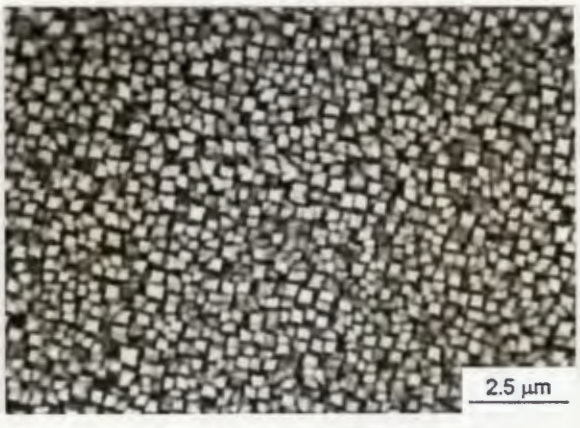

Figure 5.10. The secondary γ' is cuboidal and located in the dendrites.

An interesting feature of the carbides in the as received DS MarM-002 is the presence of the small HfC carbides, which probably formed during the stress relieving heat treatment. These carbides are found scattered throughout many of the eutectic zones, since hafnium segregates to the interdendritic regions during solidification (Fig. 5.15). The formation of HfC in this alloy appears to be

associated with the decomposition of the Ti- and Ta- rich carbides. Presumably, the fragmentation of the carbides releases both carbon and hafnium for the formation of the HfC, which is the more stable form of MC carbide. The HfC is not enclosed in a γ' envelope, supporting the proposal that the release of titanium and tantalum from fragmenting MC carbides leads to the formation of the envelopes.

Figure 5.11. Carbide colonies are situated in the interdendritic regions amongst the primary γ'.

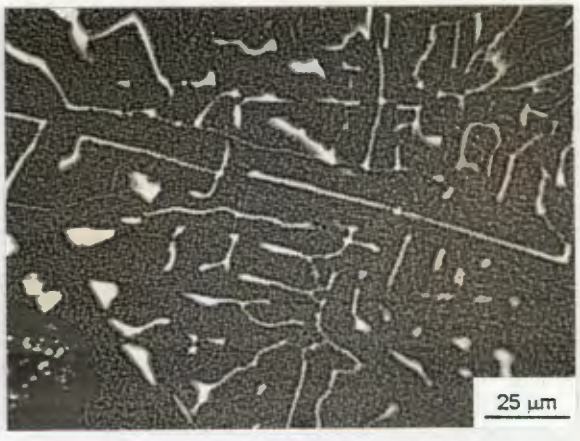

Figure 5.12. An example of the often extensive script and blocky carbides found in a colony.

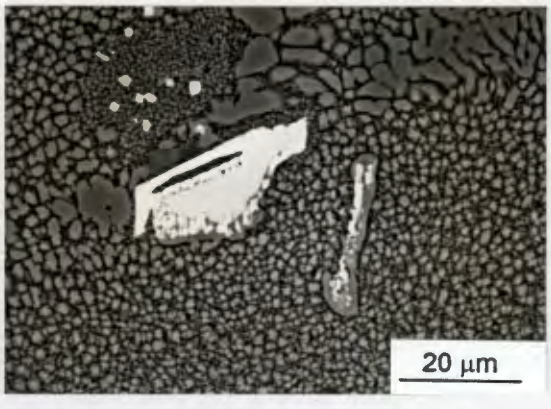

Figure 5.13. Carbide fragmentation in the DS MarM-002.

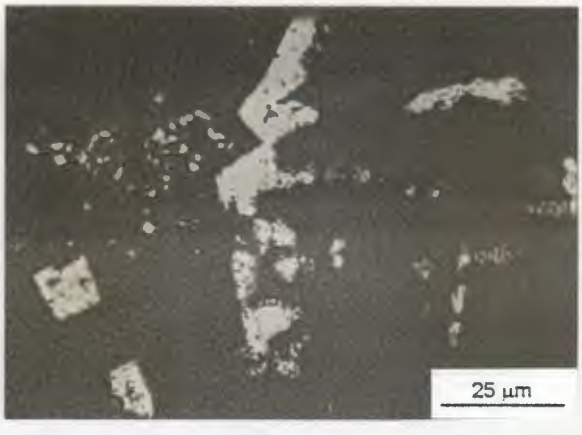

Figure 5.14a) Blocky carbides exhibiting varying degrees of fragmentation.

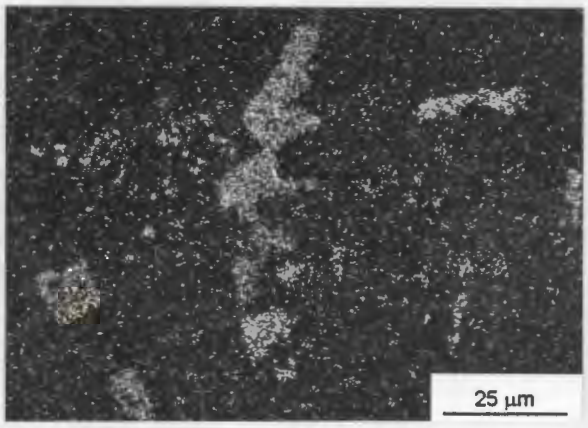

Figure 5.14b). X-ray map of the blocky carbides showing the concentration of Hf in the carbide.

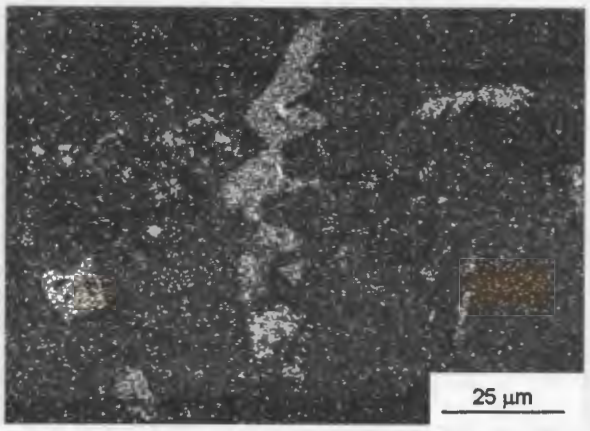

Figure 5.14c). X-ray map of the blocky carbides showing the concentration of Ta in the carbide.

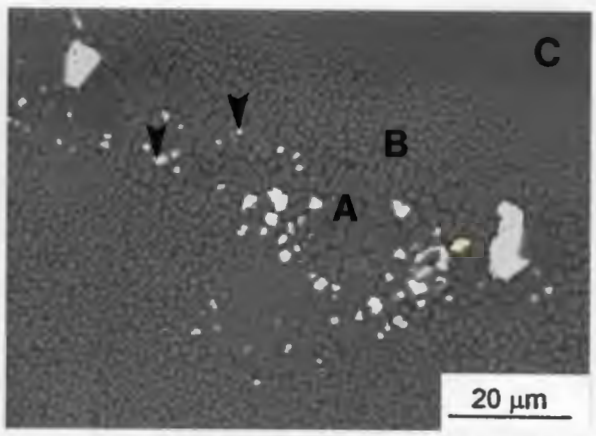

Figure 5.15. Small HfC (arrowed) is found dotted around the eutectic phase (A). Primary γ' (B) and secondary γ' (C) may also be seen.

5.3 Segregation in the As Cast and As Received Materials

Segregation of the elements between the dendritic and interdendritic regions of the as cast CC MarM-002 and the as received DS MarM-002 is tabulated in Tables 5.1 and 5.2. An area scan covering approximately 5 μm by 5 μm was analysed for each measurement, encompassing both the eutectic γ-γ', γ' and γ phases.

It may be seen in both alloys that the gamma prime formers, Al and Ti, segregate to the interdendritic regions, and thus account for the presence of the larger γ'

precipitates and the extensive eutectic γ' lamellae and blocky γ' found in these areas. Tantalum, a γ' former, appears to segregate preferentially to the interdendritic regions in the CC material but not the DS material. Unfortunately, in the EDS spectra used to calculate the compositions there is some overlap between the Ta and W peaks which makes accurate analyses of these elements difficult. Hafnium is seen to partition strongly to the interdendritic regions. Low melting point (Ni-Hf) phases would, therefore, be expected to form primarily in the interdendritic regions. These, of course, are potential sites of incipient melting in the material.

The gamma formers, Cr, Co and W segregate to the dendritic regions, aiding the formation of the smaller cuboidal γ' seen in these areas.

Element	Interdendritic Region	Dendrite	Partitioning Ratio
Ni	61.6 ± 2.7	59.6 ± 0.3	1.03
Cr	7.0 ± 2.7	7.8 ± 0.2	0.89
Co	8.3 ± 1.2	10.6 ± 0.1	0.78
Al	5.3 ± 0.7	4.0 ± 0.1	1.32
Ti	1.7 ± 0.3	0.5 ± 0.03	3.51
Ta	5.9 ± 2.1	4.7 ± 0.1	1.26
W	5.0 ± 0.9	12.0 ± 0.2	0.42
Hf	5.1 ± 3.4	0.7 ± 0.2	6.94

Table 5.1. The compositions (weight percent) of the dendritic and interdendritic areas of CC MarM-002 in the as cast condition are presented in this table. The partitioning ratios of the elements (interdendritic composition divided by the dendritic composition) is also presented here. The compositions were measured by EDS.

Element	Interdendritic Region	Dendrite	Partitioning Ratio
Ni	63.1 ± 2.5	58.6 ±1.0	1.08
Cr	6.3 ± 2.0	8.8 ± 0.6	0.71
Co	9.3 ± 1.1	11.1 ± 0.4	0.83
Al	4.5 ± 0.5	3.5 ± 0.2	1.30
Ti	1.3 ± 0.2	0.8 ± 0.1	1.65
Ta	5.6 ± 0.4	5.4 ± 1.0	1.04
W	7.8 ± 1.0	10.6 ± 0.6	0.73
Hf	2.1 ± 0.6	0.8 ± 0.2	2.48

Table 5.2. The compositions (weight percent) of the dendritic and interdendritic areas of DS MarM-002 in the as received condition are presented in this table. The partitioning ratios of the elements (interdendritic composition divided by the dendritic composition) is also presented here. The compositions were measured by EDS.

5.4 Incipient melting in MarM-002

The incipient melting temperature was measured by heating samples of MarM-002 to temperatures above 1220°C at the maximum furnace heating rates of 900°C/hour up to 1100°C and 600°C/hour above 1100°C. No signs of melting were found at temperatures of 1220°C, but at 1240°C the microstructure revealed the onset of incipient melting in both CC and DS alloys. The regions of melting are shown in Fig. 5.16 and consist of a cellular morphology, Ni-Hf rich compound in the centre, surrounded by a fine eutectic. Hafnium carbides are situated in the Ni-Hf compound, suggesting that they have formed from excess hafnium and carbon, as postulated by Yunrong et al[40,41]. The exact composition of the Ni-Hf compound is unknown, but is unlikely to be exactly the same as that examined by Yunrong et al[40,41], since the melting temperature is in the region of 1240°C, compared with the temperature range of 1135°-1180°C measured by Yunrong et al[40,41]. Low melting point phases such as Ni_5Hf had not been found in either the as cast CC nor the as received DS MarM-002. This suggests that the low melting point Ni-Hf phases are present in amounts less than 2%, since the carbides compose 2% of the volume fraction of the materials, yet are readily visible.

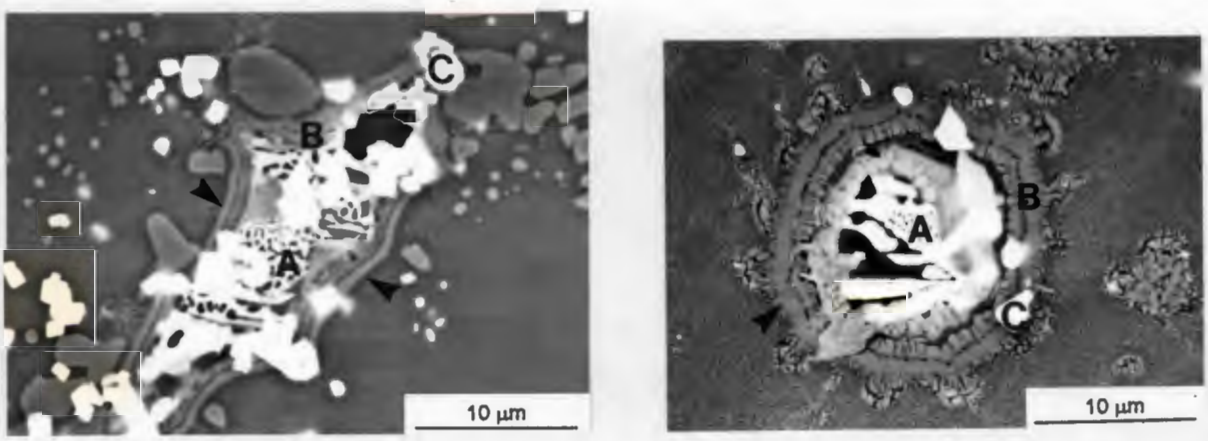

(a) (b)

Figure 5.16(a) and (b). Incipient melting in MarM-002 (arrowed) consists of a cellular Ni-Hf compound (A) surrounded by eutectic phase (B). Hafnium carbides (C) are found in the Ni-Hf and the fine eutectic.

Interestingly the sites of melting were relatively easily distinguished in the SEM using a mixture of back-scattered and secondary electrons for viewing, but were much less noticeable when using only secondary electrons (Fig. 5.17).

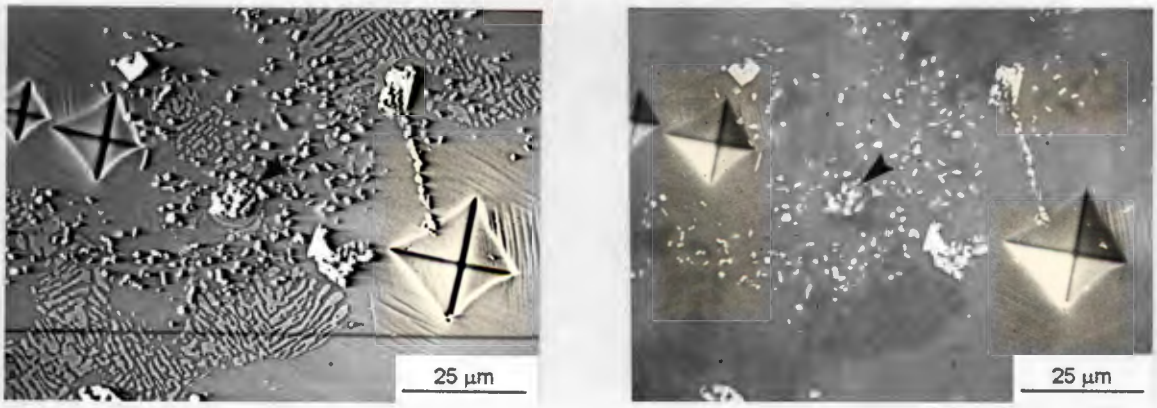

(a) (b)

Figure 5.17. Incipient melting (arrowed) viewed using (a) a back-scattered and secondary electron mixed image in the SEM is more visible than an image composed of (b) pure secondary electrons.

5.5 The Varied Rate Solution Heat Treatment for MarM-002

The varied rate solution heat treatment, used to overcome the problem of incipient melting and still achieve maximum γ' dissolution, was determined for both the CC and DS MarM-002 through repetitive heat treatment-microstructure studies. The final heat treatment schedule is presented below in Table 5.3.

Altough the maximum temperature attained without incipient melting was 1260°C, three different VRSHT's terminating at 1220°C, 1240°C and 1260°C were used in this study. This permitted investigation into the correlation between solution treatment temperature and the extent of γ' and eutectic γ' dissolution. For each of the three VRSHT's, a dwell period of two hours was used at the respective maximum temperature, to provide sufficient time for γ' dissolution. The effect of the varied rate solution heat treatment and the "conventional" 1220°C/2h solution heat treatment on the microstructure of the alloys is presented in the following sections.

Heating Rate (°C/h)	Temperature (°C)	Dwell Period (h)
900	1180	0.0
12.0	1200	0.0
4.8	1220	0.0
2.0	1260	2.0

Table 5.3. The varied rate solution heat treatment schedule for MarM-002 is presented here. For this study three varied rate solution heat treatments terminating at 1220°C, 1240°C and 1260°C were used. The above heating rates were used for each solution treatment, to the relevant maximum temperatures.

5.6 The Effect of the Solution Heat Treatment on the Microstructure of the Conventionally Cast Material

5.6.1 1220°C/2h

The microstructure of the CC material following the 1220°C/2h solution heat treatment is shown in Figure 5.18. The heat treatment temperature is not high enough to completely dissolve the γ' precipitates and a volume fraction of approximately 16.1 ± 2.2 % remains undissolved in the dendrites. The remaining precipitates have a morphology that varies from equi-axed and spheroidal to elongated (Fig. 5.19). This suggests that the dissolution process is influenced markedly by the surface: volume ratio, as well as the elastic interaction stresses between the precipitates. Thus, it appears that the initially cuboidal particles become spheroidal as dissolution proceeds, thereby reducing the surface:volume ratio. At the same time the precipitates may coalesce to form rods and thereby reduce both the surface energy and the elastic interaction energy between neighbouring precipitates. The distribution of the γ' varies from a random distribution to linear arrays (Fig. 5.18). The alignment of the precipitates to form the linear arrays is again due to the need to lower the interaction energy during the dissolution process, and is, therefore, most common where there is a greater number of γ' precipitates.

The eutectic phase (Figs. 5.18 and 5.20) was not greatly affected by the solution heat treatment and remains undissolved. The volume fraction of eutectic γ' was

measured at 15.1 ± 0.5 %. Gamma prime lamellae and blocky particles that are found in the eutectic do not appear to have coarsened or coalesced appreciably.

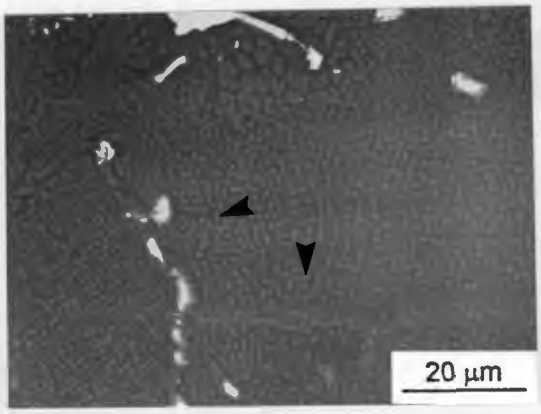

Figure 5.18. Conventionally cast MarM-002 following the 1220°C/2h solution heat treatment. The γ' precipitates (examples arrowed) are not completely dissolved.

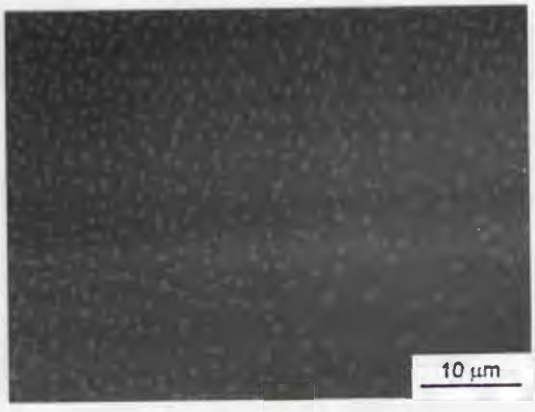

Figure 5.19. The γ' has a morphology that varies from equi-axed to rod shaped because of the need to reduce the surface:volume ratio and the interaction stresses.

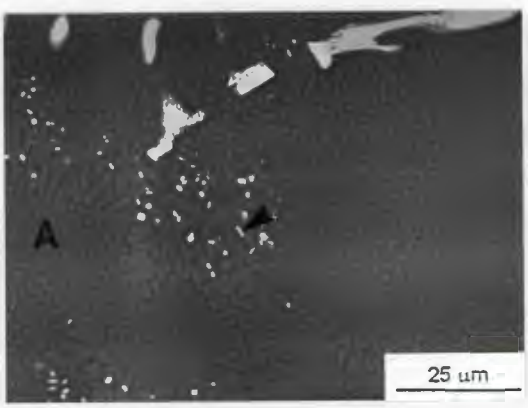

Figure 5.20. The eutectic phase (A) is not dissolved by the 1220°C/2h solution treatment and the γ' lamellae and blocky precipitates have not coarsened. HfC (arrowed) is sprinkled throughout the eutectic γ phase.

An interesting consequence of the solution heat treatment is the formation of Hf-carbides located in the eutectic phase. These carbides are enclosed in the γ matrix phase, unlike the Ta- and Ti-rich script and blocky carbides which are enclosed in a γ' envelope. Script and blocky carbides have begun to undergo fragmentation to various degrees. All of these carbides are surrounded by the γ'

envelopes, suggesting that even where no fragmentation is yet visible, titanium and tantalum have begun to diffuse out of the carbide.

5.6.2 VRSHT 1220°C

The varied rate solution heat treatment to a maximum temperature of 1220°C has a similar effect as the single step 1220°C/2h solution heat treatment (Fig. 5.21). Thus, the precipitates are not completely dissolved, with 15.0 ± 3.3 % remaining. The morphology of the γ' is again equi-axed or coalesced and the distribution varies from linear arrays of γ' to randomly scattered precipitates, depending on the distribution density.

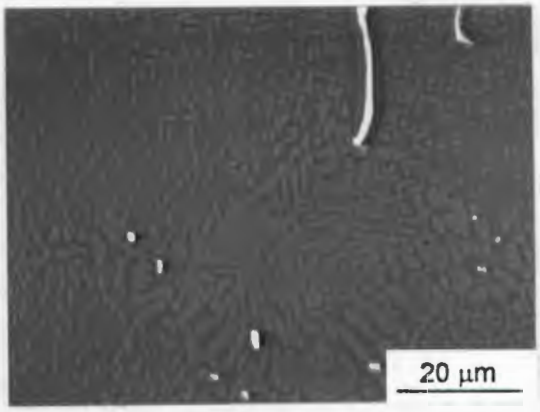

Figure 5.21. Heat treatment to 1220°C using the VRSHT does not completely dissolve the γ'. Note the coarsening of the eutectic γ' lamellae.

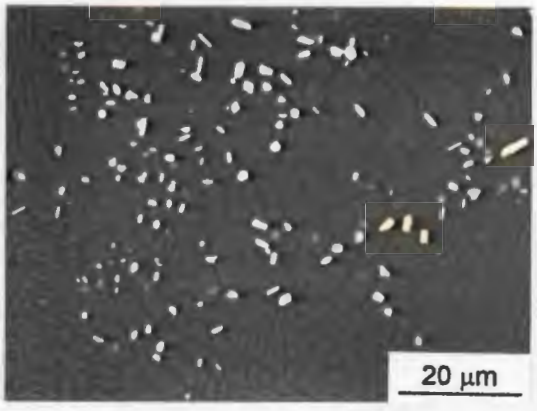

Figure 5.22. The blocky eutectic γ' precipitates have coarsened and coalesced. HfC is found in the γ regions of the eutectic.

Script and blocky carbides have fragmented and are surrounded by the γ' envelopes (Fig.5.21). Hf-carbides are found in the γ phase of the eutectic.

The eutectic γ' has undergone morphology changes, however, as a consequence of the greater time required to reach the solution temperature. The blocky and lamellae γ' have coarsened, largely through a process of particle coalescence. Thus, qualitatively, the lamellae appear to be thicker and more continuous (Fig. 5.21). Similarly, the blocky eutectic γ' precipitates are larger and less discrete (Fig. 5.22). No dissolution of the eutectic γ' is apparent and the volume fraction of the eutectic γ' is 15.9 ± 3.5 %.

5.6.3 VRSHT 1240°C

Gamma prime dissolution during the 1240°C dwell is more extensive than at 1220°C. Thus, approximately 2.2 ± 1.0 % of the γ' remains present in the dendrites (Fig. 5.23). It should be noted, however, than the measurement of the remnant γ' is to some extent subjective, since the γ' is completely dissolved in some regions but not in others (Fig.5.24).

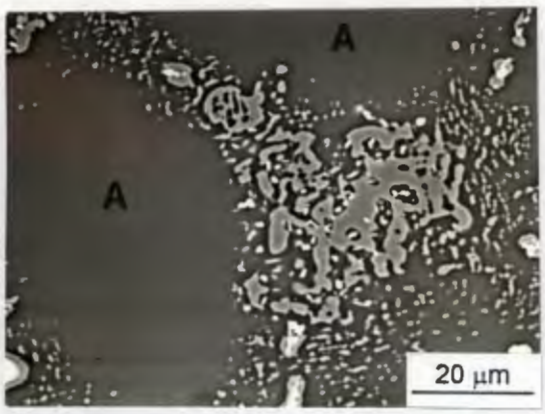

Figure 5.23. The γ' is almost completely dissolved (Region A) after heat treatment to 1240°C using the VRSHT. The eutectic γ' may have coarsened considerably.

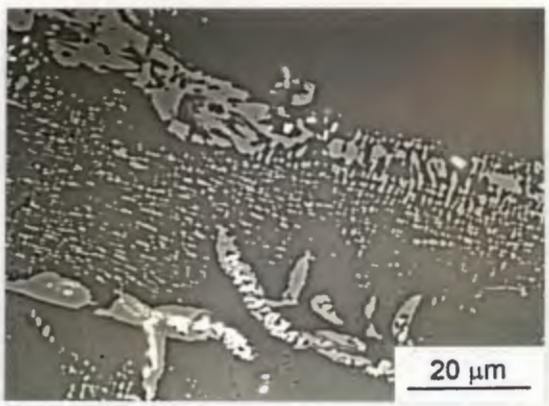

Figure 5.24. Some areas display a greater degree of γ' dissolution than others after the VRSHT 1240°C treatment. Here, for example, a greater measure of γ' is undissolved than illustrated in Fig. 5.23.

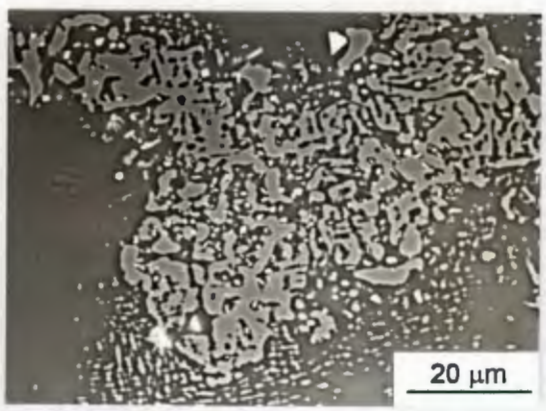

Figure 5.25. The eutectic has coarsened to form several interconnected agglomerations of γ' during the VRSHT 1240°C.

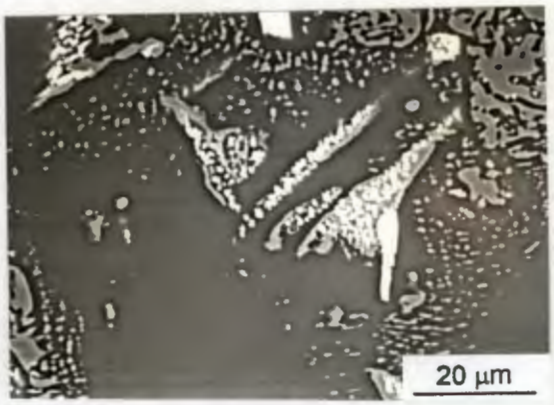

Figure 5.26. Carbides have undergone extensive fragmentation due to the long period of exposure to high temperatures.

The eutectic γ' has coarsened considerably during the long exposure to high temperatures, and may form an interconnected mass, as seen in Figs. 5.23 and 5.25. A volume fraction of about 16.1 ± 1.3 % remains, indicating that no eutectic γ' has been dissolved. The period of high temperature exposure has led to the extensive fragmentation of the Ta-, Ti-rich carbides (Fig. 5.26), but they remain enclosed in γ' envelopes, notwithstanding the relatively high solution heat treatment temperature.

5.6.4 VRSHT 1260°C

Solution treatment at 1260°C, using the VRSHT technique, results in complete dissolution of the γ' within the dendrites and a considerable decrease in the volume fraction of the eutectic phase (Fig. 5.27). The remnant eutectic phase occupies a volume fraction of 2.9 ± 1.3 % following this heat treatment. The former location of many of the dissolved eutectic γ' precipitates is indicated by the position of the Hf-carbides, which were previously associated with the eutectic phase. The remaining eutectic γ' has, once again, coarsened to form large agglomerations of precipitate.

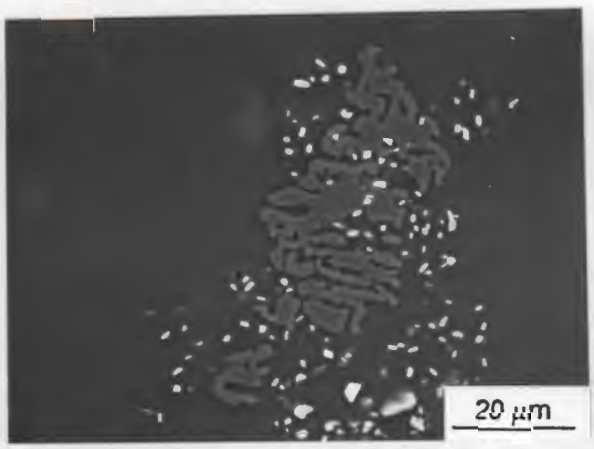

Figure 5.27. Solution treatment at 1260°C dissolves the dendritic γ' completely and the eutectic γ' substantially. Less than 3% eutectic phase remains.

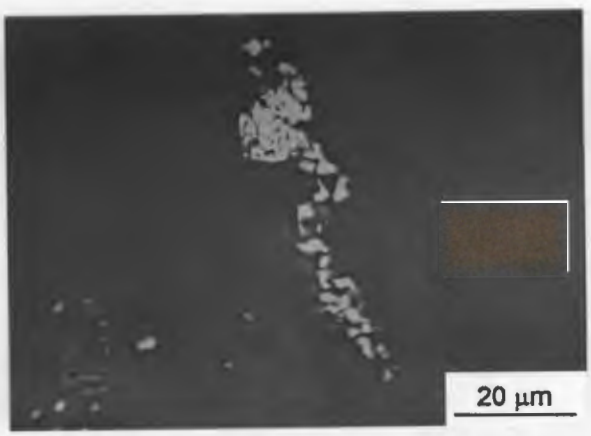

Figure 5.28. Carbide fragmentation continues at 1260°C and the γ' envelopes are now dissolved.

Carbide fragmentation continues at this heat treatment temperature, but still does not result in complete fragmentation of all the Ta-, Ti-rich carbides. Presumably, longer exposure to high temperatures would be required for complete fragmentation of all of the carbides. The temperature of 1260°C is

sufficient to dissolve the γ' envelopes which surround these carbides at lower temperatures (Fig. 5.28).

At a solution treatment temperature of 1280°C the eutectic γ' is completely dissolved, but incipient melting occurs.

5.7 The Effect of the Solution Heat Treatment on the Microstructure of the Directionally Solidified Material

In many respects the response of the DS material to the solution heat treatment is similar to that of the CC alloy. The degree of γ' and eutectic γ' dissolution are comparable in most cases, and the details of the dissolution process are described in the following sections.

5.7.1 1220°C/2h

Directionally solidified MarM-002 responds in a similar way as the conventionally cast MarM-002 to the 1220°C/2h solution heat treatment. Thus, the γ' is not completely dissolved and approximately 15.2 ± 2.2 % volume fraction of γ' within the dendrite remains (Fig. 5.29). The greatest proportion of γ' dissolution takes place within the dendrite arms where the secondary γ' is found. Less dissolution occurs in the interdendritic regions where the primary γ' is located. The secondary γ' in the DS material is, in many regions, cuboidal and aligned (Fig. 5.30); more so than the CC material in the same heat treated condition. This may be due to local compositional variations forming γ and γ' phases of a slightly greater misfit and thus greater elastic interaction stresses and pronounced cuboids. There would consequently be a greater driving force to lower the elastic interaction energy by forming the aligned cuboids. Additionally, γ' composition variations would mean that certain precipitates possess a solvus temperature greater than 1220°C. These precipitates would then coarsen instead of dissolve, further increasing the misfit strains.

The primary γ' retains an equi-axed morphology, but no longer displays the ogdoadal characteristics seen in the as received condition.

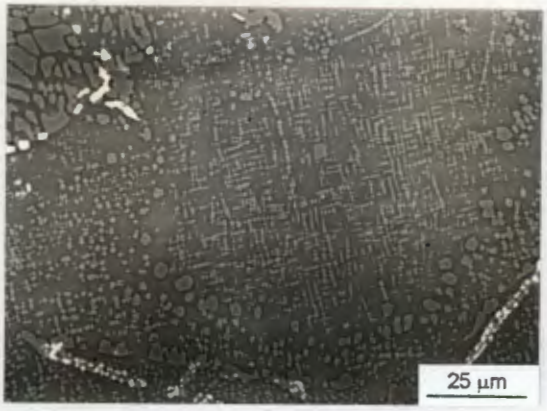

Figure 5.29. The microstructure of DS MarM-002, following the 1220°C/2h solution treatment, exhibits undissolved γ'.

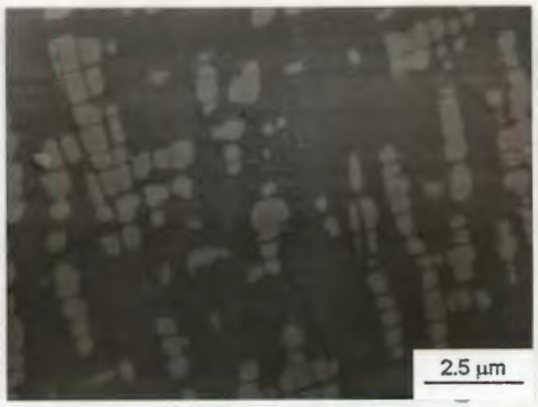

Figure 5.30. The secondary, undissolved γ' remains cuboidal and displays a relatively high degree of alignment.

The eutectic γ-γ' phase does not appear to be significantly affected by the solution heat treatment. Large-scale coarsening of the eutectic γ' has not occurred and the lamellae and blocky γ' remain discrete particles (Fig. 5.31). Volume fraction measurements suggest that the volume fraction has decreased from about 15.0 ± 1.3 % (in the as received condition) to 11.1 ± 2.5 %. When the microstructure is viewed qualitatively, however, there appears to be little dissolution of the eutectic γ'. The significance of this discrepancy between qualitative and quantitative observations is arguable if the error associated with the measurements are considered.

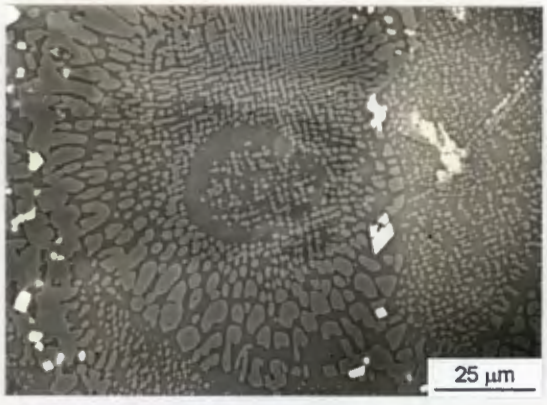

Figure 5.31. The eutectic γ' has not coarsened significantly and the lamellae and blocky particles remain discrete.

Carbide characteristic are not significantly altered by the solution heat treatment. The Ta-, Ti-rich carbides remain enclosed in γ' envelopes and continue to fragment. Likewise, HfC is commonly encountered in the γ phase of the eutectic γ'.

5.7.2 VRSHT 1220°C

The primary and secondary γ' is not completely dissolved by this heat treatment and approximately 16.0 ± 2.3 % of the γ' remains (Fig. 5.32). The secondary γ' is distributed in linear arrays and is relatively equi-axed in morphology, although lingering traces of the cuboidal shape are still evident. The γ' in the eutectic phase has coarsened to form thicker, interconnected lamellae or coalesced blocky particles of γ' (Fig. 5.33). The volume fraction of the eutectic phase is unchanged from the as received condition and was measured at 15.6 ± 2.1 %.

Carbides appear largely unaffected by the heat treatment; fragmenting carbides remain enclosed in the γ' envelopes and HfC is found dispersed in the eutectic phase.

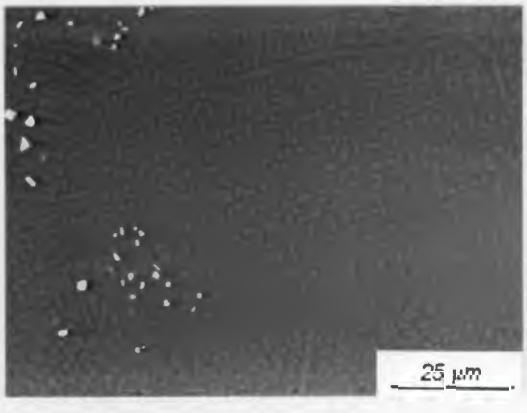

Figure 5.32. The microstructure of DS MarM-002 following the VRSHT at 1220°C.

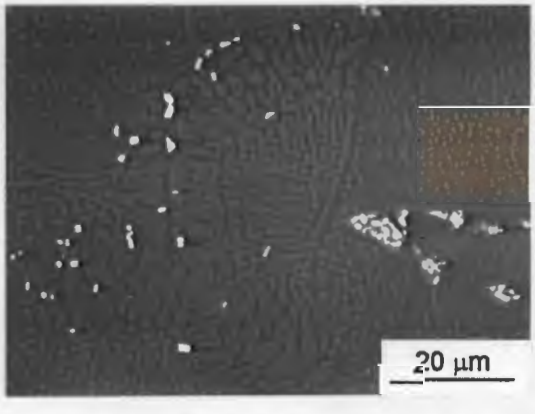

Figure 5.33. The blocky eutectic γ' particles have coalesced and the lamellae have thickened to form interconnected networks of γ'.

5.7.3 VRSHT 1240°C

Gamma prime precipitates are almost completely dissolved after solution treatment at 1240°C (Fig. 5.34). The precipitates are dissolved in many dendrite arms, but not all, and a precipitate volume fraction of approximately 2.6 ± 2.2 % remains. The relatively large confidence interval in this measurement reflects the range of γ' dissolution. The more advanced degree of dissolution than the 1220°C solution treatment has led to the "rounding off" of the cuboidal morphologies and the precipitates have a more spheroidal shape.

The eutectic γ' may have undergone some dissolution since the volume fraction has decreased to 10.4 ± 2.3 %. This is unexpected considering that the eutectic γ' in the CC material only began dissolving at 1260°C. If this γ' is indeed dissolving, it may be due to the casting conditions forming a eutectic γ' of a slightly different composition with a slightly lower solvus temperature. On the other hand, it is not inconceivable that there may have been less eutectic phase in this particular volume of material, with correspondingly more primary γ' occupying the interdendritic regions.

Carbide characteristics do not appear significantly different from the as received condition although, qualitatively, there may be a greater degree of fragmentation and more HfC situated in the eutectic γ phase.

Figure 5.34. The microstructure of DS MarM-002 following solution treatment at 1240°C is shown here. The γ' is almost completely dissolved and the eutectic γ' has coarsened.

5.7.4 VRSHT 1260°C

Gamma prime precipitates are completely dissolved by solution treating at 1260°C. Similarly, the eutectic γ' has dissolved to a large extent and only 2.4 ± 0.6 % remains (Fig. 5.35). Coarsening of the eutectic γ' has been common in the VRSHT process and the remaining eutectic γ' often forms large, interconnected particles.

Most, but not all, of the γ' envelopes surrounding carbides has been dissolved and, qualitatively, the fragmentation of carbides is advanced, compared with the as received condition.

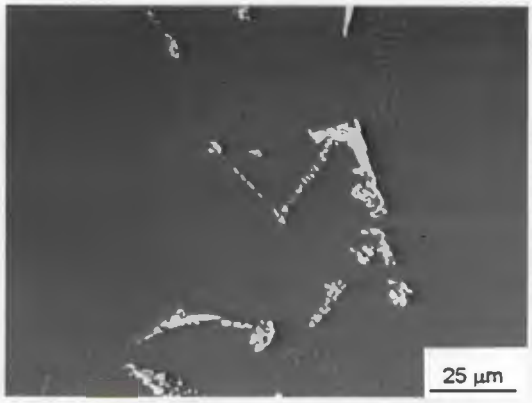

Figure 5.35. Solution heat treatment at 1260°C has dissolved all of the γ' and most of the eutectic γ' and carbide envelopes.

5.8 Effect of the VRSHT on the Gauge Length Microstructure of the Mechanical Test Specimens

The mechanical test specimens were composed of DS material only, and in order to verify the response of the microstructure of the mechanical test specimens to heat treatment, creep specimens were sectioned longitudinally after heat treatment to 1240°C and 1260°C using the VRSHT. The micrographs of these specimens are shown in Figs. 5.36 and 5.37. Unfortunately the manual polishing of these specimens during metallographic preparation prevented the removal of all the grinding scratches, but the microstructures are still clearly visible.

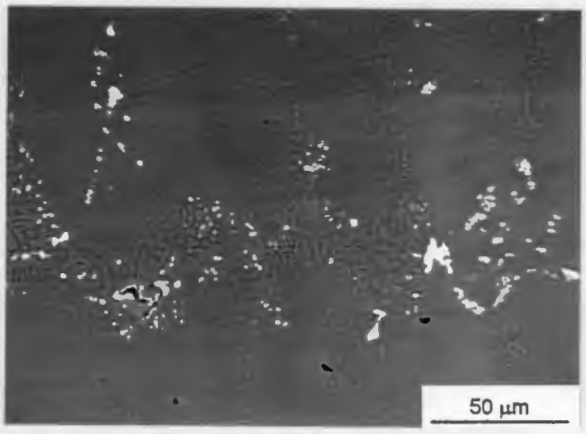

Figure 5.36. The microstructure of the specimen solution treated at 1240°C is shown here. The γ' is almost completely dissolved.

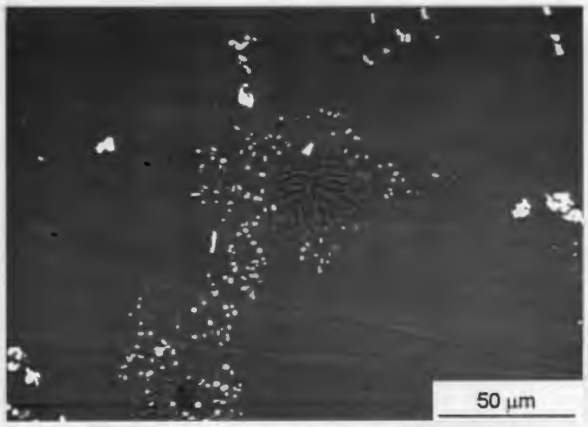

Figure 5.37. The microstructure of the specimen solution treated at 1260°C is shown here. The γ' is completely dissolved and much of the eutectic has been dissolved.

It can be seen that the microstructure of the gauge lengths of the specimens is identical to that seen previously in sections 5.7.3 and 5.7.4. Thus, in the creep specimen solution treated at 1240°C, the γ' is almost completely dissolved, particularly within the dendrite arms, but the eutectic γ' remains undissolved (Fig. 5.36). The carbides are fragmenting and enclosed in the γ' envelopes while HfC is found in the eutectic γ phase.

The microstructure of the creep specimen solution treated at 1260°C reveals that the γ' is completely dissolved and the eutectic γ' is almost completely dissolved (Fig. 5.37). Coarsening of the eutectic γ' is evident, both in this specimen and the specimen solution treated at 1240°C. The carbides in the alloy solution treated at the higher temperature are fragmented, but no longer surrounded by the γ' envelopes, which have been dissolved. Positions that were formerly occupied by the eutectic are marked by the location of the HfC.

5.9 Response of the DS alloy to the Ageing Heat Treatment

Following the solution treatment of the DS alloy, the material was aged at 1050°C/12h + 870°C/16h to bring about nucleation and growth of the

precipitates. The effect of the ageing heat treatment on the microstructure of the solution treated alloy will be presented below.

5.9.1. 1220°C/2h

The microstructure of the specimen aged after the 1220°C/2h solution heat treatment is shown in Fig. 5.38. Cuboidal precipitates with an average cube length of 0.25 ± 0.08 μm are found throughout the material; in the dendrites as well as between primary γ' particles and between the eutectic lamellae (Fig. 5.38). The cuboids are relatively well aligned in "rows" of precipitates, as desired for optimum mechanical properties (Fig. 5.39). The precipitates that were not dissolved by the solution heat treatment constitute the larger, primary γ' dispersed amongst the secondary, cuboidal precipitates. The primary γ' is found mainly in the interdendritic regions, but is commonly encountered within the dendrite arms, as seen in Fig. 5.40. The morphology of the primary γ' varies from cuboidal-oblong to equi-axed with a "diameter" of 1.2 ± 0.33 μm. Coalescence of the primary γ' is evident in some precipitates (Fig. 5.41).

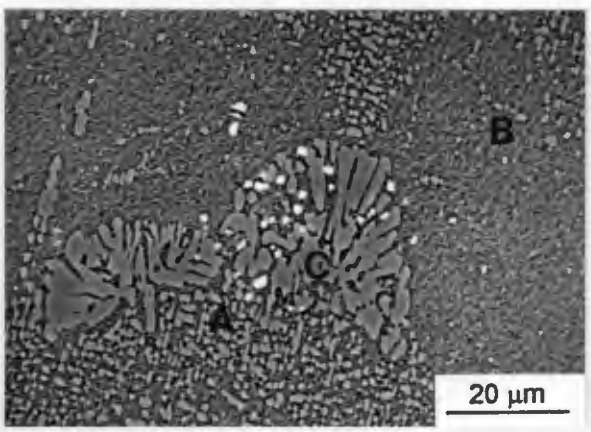

Figure 5.38. The microstructure of the material solution treated at 1220°C/2h and aged at 1050°C/12h + 870°C/16h is shown. Primary γ' (A) and secondary γ' (B) are visible, together with the eutectic γ' (C).

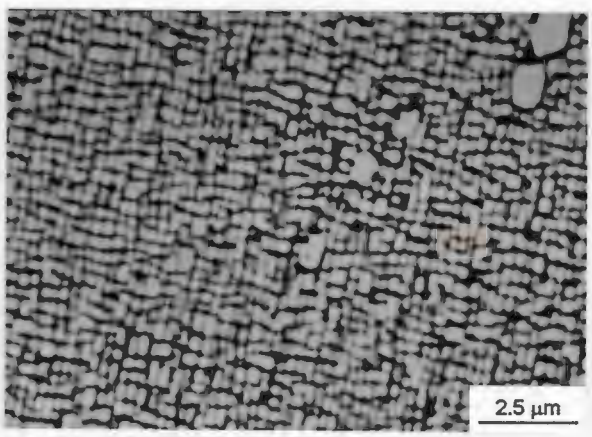

Figure 5.39. The secondary γ' is relatively cuboidal and aligned.

It appears that the eutectic γ' has coarsened during the ageing heat treatment, with the associated thickening of γ' lamellae and coalescence of the blocky γ'. Qualitatively, the extent of coarsening does not appear to be as severe as that seen in the material subjected to the VRSHT.

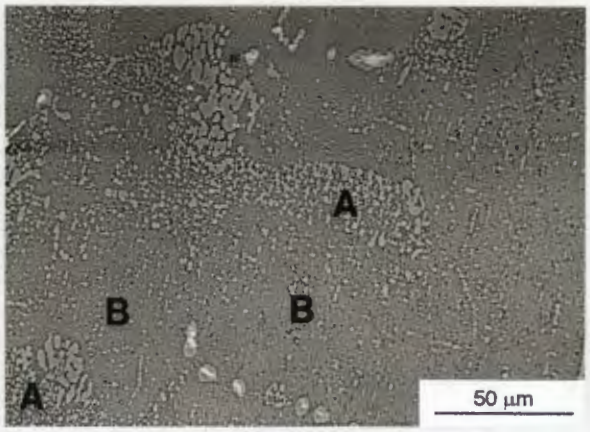

Figure 5.40. Large, primary γ' is commonly found in the interdendritic areas (A), as well as within the dendrite arms (B).

5.9.2. VRSHT 1220°C

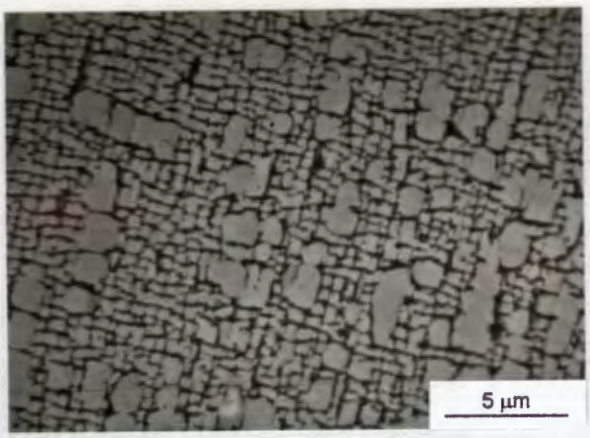

Figure 5.41. After ageing the VRSHT 1220°C, the secondary γ' size is 0.35 ± 0.11 μm and the primary γ' size is about 1.2 ± 0.41 μm.

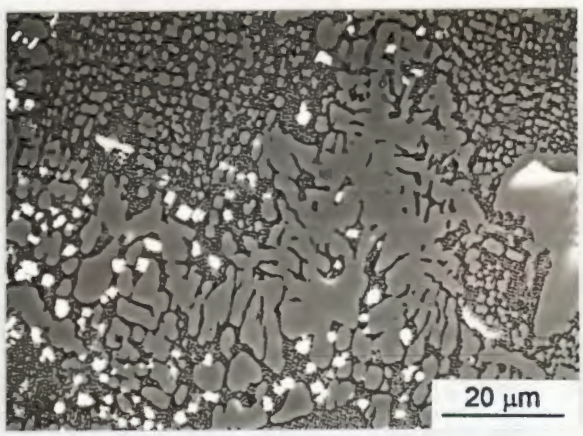

Figure 5.42. The eutectic γ' viewed here has coarsened dramatically.

The ageing heat treatment has resulted in a secondary, cuboidal γ' size of 0.35 ± 0.11 μm, with a distribution that is well aligned in linear rows. The primary γ' is found within the dendrites and in the interdendritic areas with a cuboidal-oblong morphology (Fig. 5.41). Coalescence of this larger γ' is evident, arising from

both the solution and ageing heat treatments. Within the dendrites the primary γ' is found in linear rows, presumably along the ⟨001⟩ direction[19,20]. Alignment along the ⟨001⟩ direction is commonly seen in superalloys, since the elastic modulus is the lowest in this direction and the elastic stresses between neighbouring precipitates are minimised in this plane. The primary γ' seems to be present in greater quantity within the dendrite arms of this specimen than the specimen solution treated at 1220°C/2h and aged.

Coarsening of the eutectic γ' may be quite extensive (Fig. 5.42); this is not surprising considering the long periods of exposure to high temperatures.

5.9.3. VRSHT 1240°C

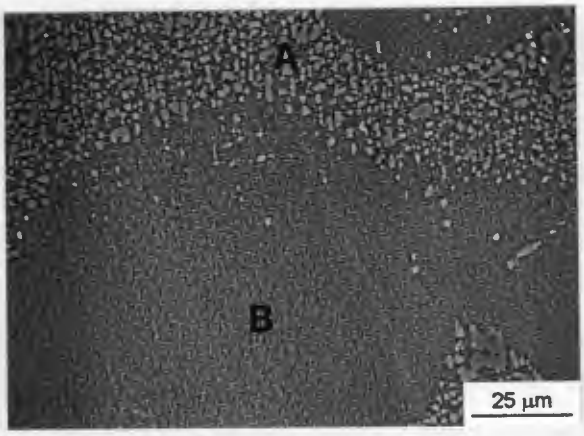

Figure 5.43. In the specimen solution treated at 1240°C and aged, the primary γ' is found almost only in the interdendritic areas (A). The dendrites (B) contain the secondary γ'.

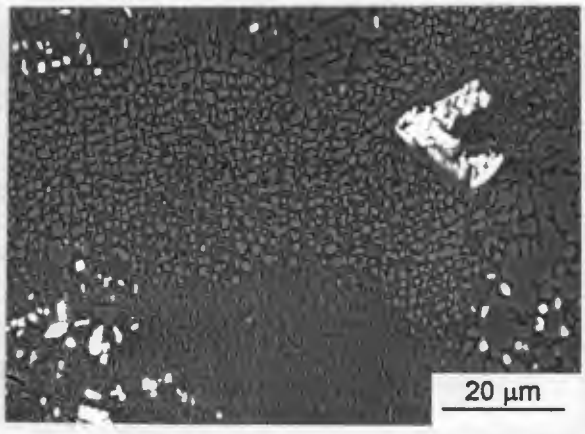

Figure 5.44. The coalesced eutectic, primary γ' and carbides of the aged material can be seen in this micrograph.

The microstructure of the VRSHT 1240°C specimen, following ageing, is shown in Figs. 5.43 and 5.44. The secondary γ' is well aligned (presumably along the ⟨001⟩ directions), with a cube length of approximately 0.24 ± 0.06 μm. Primary γ' is found largely in the interdendritic regions and is very seldom encountered within a dendrite. This, of course, reflects the greater extent of γ' dissolution in the dendrites during the solution heat treatment, since the primary γ' is formed by γ' undissolved by the solutionizing process. The primary γ' has a "diameter" of 1.3 ± 0.5 μm. Overall, the VRSHT 1240°C could be described as having a more

"refined" microstructure than the material solution treated at 1220°C, since the likelihood of finding primary γ' within the dendrites is much reduced.

5.9.4. VRSHT 1260°C

The γ' in this specimen, apart from the eutectic γ' remnant, is found only in the cuboidal form and is approximately 0.26 ± 0.14 μm in cube length. Microstructures of this specimen are shown in Fig. 5.45. Many of the γ' envelopes surrounding the carbides were dissolved during the solution heat treatment, but some carbides remain enclosed in γ'. These envelopes were either not dissolved by the solution heat treatment, or were formed during the ageing heat treatment.

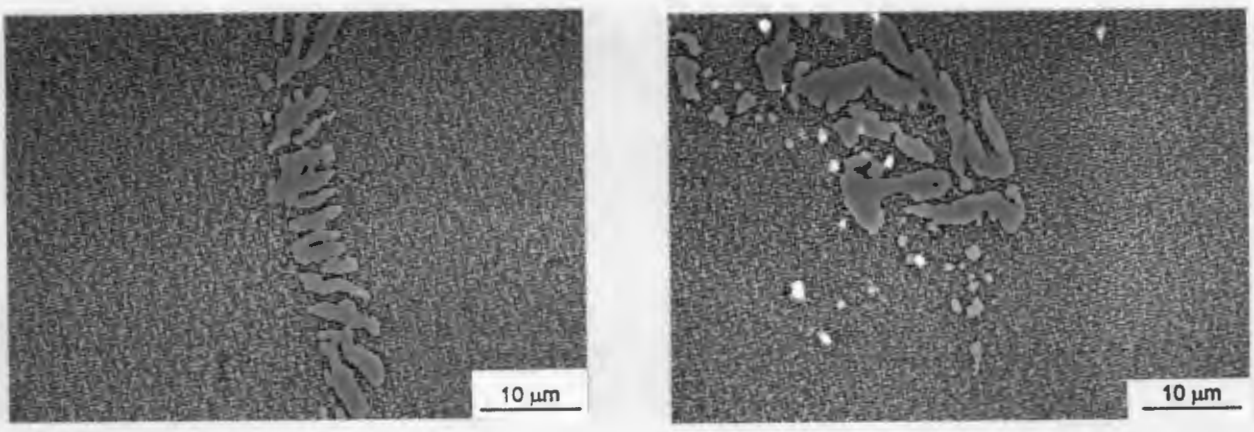

a) b)

Figure 5.45. The microstructure of MarM-002 following a 1260°C solution treatment and the 1050°C/12h + 870°C/16h ageing heat treatment is shown in these micrographs.

5.10. Mechanical Properties

5.10.1. Tensile Behaviour

The results of the tensile tests performed on the DS MarM-002 at 900°C are shown in Figures 5.46 and 5.47. It is shown (Fig. 5.46) that there are significant variations in tensile strength between the different solution heat treatments. The

material tested in the as received condition and the VRSHT 1220°C specimens display the lowest tensile strengths of 760-797 MPa. Intermediate tensile strength levels of 810-836 MPa are exhibited by the 1220°C/2h and the VRSHT 1240°C material. The highest strength levels are displayed by the VRSHT 1260°C (Test 1) specimens at 916-929 MPa. The high tensile strengths seen in the VRSHT 1260°C specimens were confirmed by repeating the tests on a further three specimens (Test 2). The Test 2 specimens exhibited slightly lower tensile strengths (891-901 MPa) than the Test 1 specimens, but the strengths were still higher than DS MarM-002 in the other heat treated conditions.

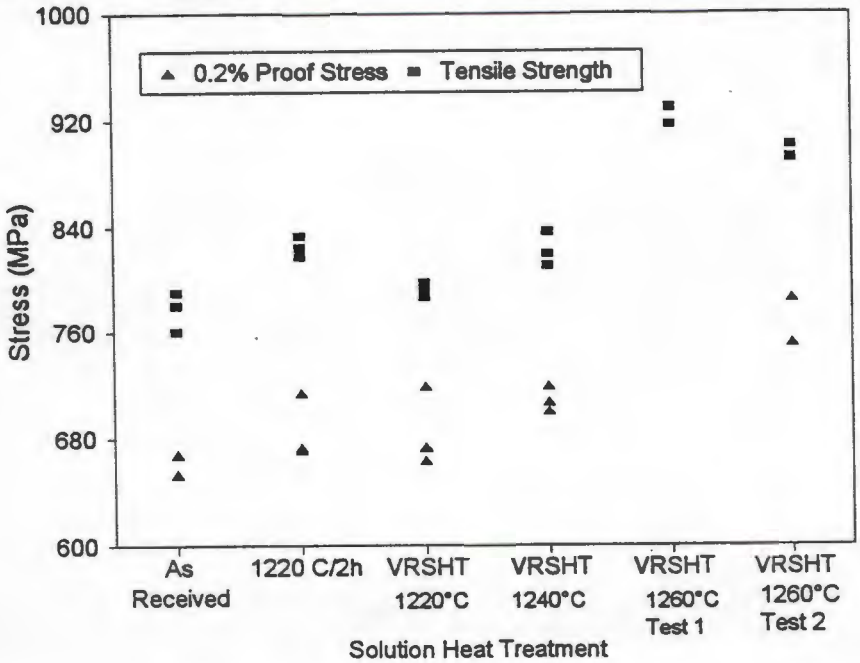

Figure 5.46. The tensile strength and the 0.2% proof strength of DS MarM-002 tested at 900°C at a strain rate of 5×10^{-3} s^{-1} is shown in this diagram. The X-axis indicates the solution treatment used for the specimens.

The 0.2% proof strengths displayed less marked trends, but the trend was nevertheless similar to that exhibited by the tensile strength values. Thus, the as received material had the lowest 0.2% proof stress of 653-668 MPa. Intermediate strength levels were exhibited by the materials solution treated at 1220°C/2h, as well as the VRSHT 1220°C and VRSHT 1240°C specimens. There was greater scatter in the 1220°C/2h and VRSHT 1220°C specimens (670-719 MPa) compared with the VRSHT 1240°C material (700-719 MPa). Unfortunately, equipment malfunction of the chart recorder prevented the calculation of the 0.2% proof stress for the VRSHT 1260°C Test 1 specimens.

The proof strengths of the Test 2 specimens were, however, recorded, and are seen to be greater (751-785 MPa) than the material solution treated at lower temperatures.

There was little significant difference in the elongation of the specimens (Fig.5.47); the greatest scatter, and possibly the lowest ductility (10% elongation), was exhibited by the 1220°C/2h and the VRSHT 1260°C Test 1 specimens. The VRSHT 1220°C, 1240°C and 1260°C Test 2 materials had the highest ductility values (15-18%).

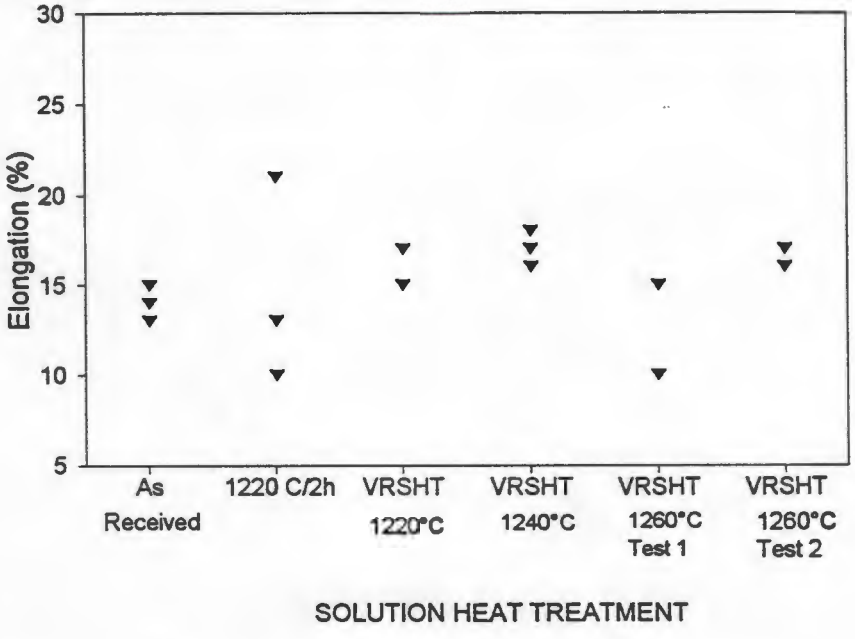

Figure 5.47. The elongation of the 900°C tensile test specimens are shown in this diagram. The X-axis indicates the solution treatment used for the specimens.

Failure Initiation Sites

Metallographic specimens, prepared from the tensile test specimens sectioned parallel to the tensile axis, were examined to find the areas where fracture is initiated. Despite the differences in tensile strength of material solution treated at different temperatures, the initiation of failure in all of the cases occurs at the carbides, either within a cabide or at the carbide interface. This is illustrated in Figs. 5.48 and 5.49. Although it seems clear that fracture begins mainly at the carbide sites, it is difficult to separate the effect of the eutectic phase, since the

carbides are commonly associated with the eutectic. If the crack path is followed, however, it is found that the crack often (but not always) follows the interface of the eutectic γ' on the outskirts of the eutectic rosette (Fig. 5.50). Thus it appears that the eutectic γ' / γ matrix interface is a secondary point of weakness in the material. On some occasions, cavities have been seen to initiate at the interface of the primary γ' and the γ matrix (Fig. 5.51), but the incidence of these cavities is low in comparison with the cavity formation at the carbide interfaces.

Cracks initiating on the surface of the specimen and propagating inwards are commonly seen but are heavily oxidized, thus preventing identification of the initiation sites. It is not unexpected, however, that such cracks would develop where the carbides or eutectic phase intersects the surface.

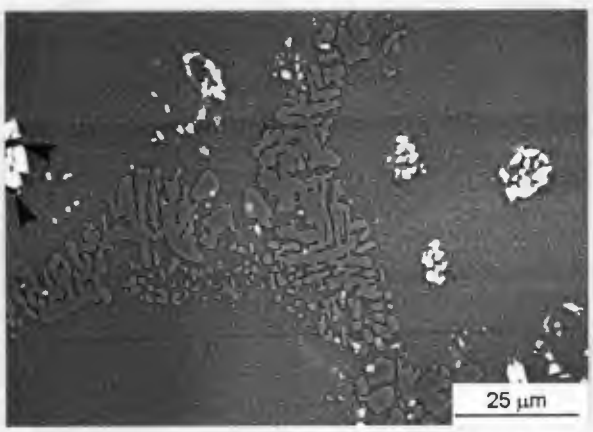

Figure 5.48. Fracture in the VRSHT 1260°C specimen initiates at the carbide interface or within the carbide. The cavity initiation sites are arrowed in this micrograph.

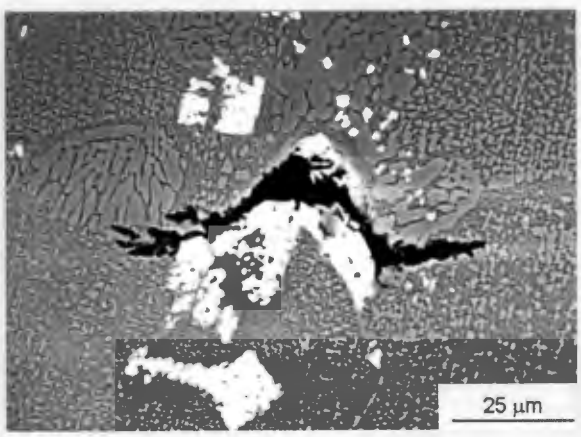

Figure 5.49. Fracture in the VRSHT 1220°C specimen is seen to initiate at the carbide sites. The crack appears to traverse the edge of the eutectic γ' before propagating at 90° to the stress axis (the stress axis is top-bottom in this photograph).

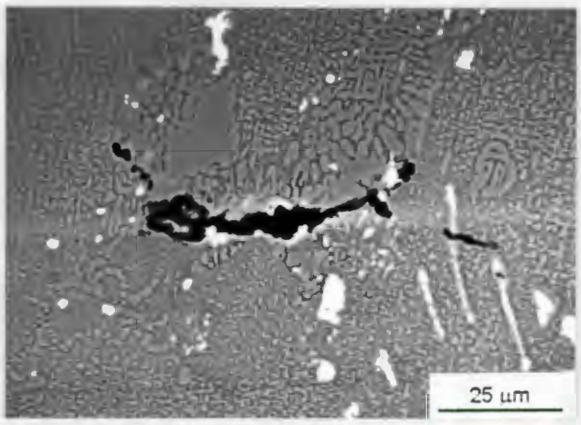

Figure 5.50. This cavity in the VRSHT 1220°C specimen appears to have initiated at the carbides and is propagating around the outskirts of the eutectic rosette, along the eutectic γ'-γ matrix interface.

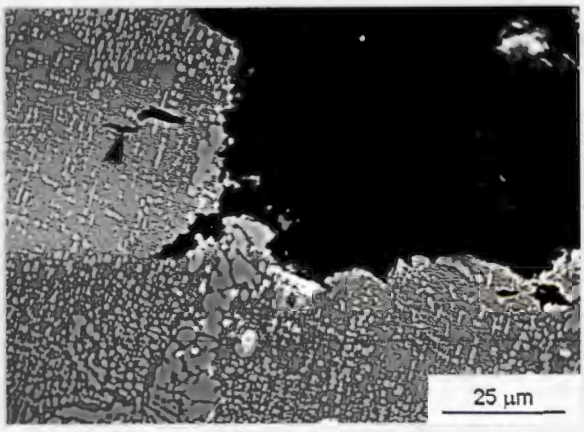

Figure 5.51. Crack initiation at the primary γ'- γ matrix interface (arrowed) has occurred in the VRSHT 1220°C specimen. The main fracture surface may also be seen.

5.10.2. Creep Behaviour

The creep behaviour of DS MarM-002 in the different heat treated conditions is shown in Fig. 5.52. There appears to be little correlation between the solution treatment temperature and the creep life. Instead, in all the specimens solution treated at 1240°C and below, there was a wide range in creep life between specimens of the same heat treated conditions. The as received condition (Fig.5.52a) exhibited the greatest range in creep life, from 75 hours to 400 hours, and, in fact, the as received condition displayed the shortest and longest creep lives of all the specimens. The creep lives of the 1220°C/2h and the VRSHT 1240°C specimens were approximately the same, and ranged from about 250 hours to 350 hours (Figs. 5.52b,d). The greatest consistency in creep life (260 hours) was displayed by the VRSHT 1260°C specimens (Fig. 5.52e). Specimen 1 in Figure 5.52c (VRSHT 1220°C condition) did not undergo creep to fracture because of furnace failure, but if the shape of the existing curve is considered the specimen is not expected to have lasted more than 150 hours. Thus, the scatter in creep life of the VRSHT 1220°C specimens was also quite wide, and can be said to vary from an estimated 150 hours to 360 hours.

All of the creep specimens had a wide scatter in creep strains; for example the as received condition had a fracture strain that varied from 10% to about 27%.

Even the VRSHT 1260°C material exhibited a fracture strain that ranged from 10% to 25%.

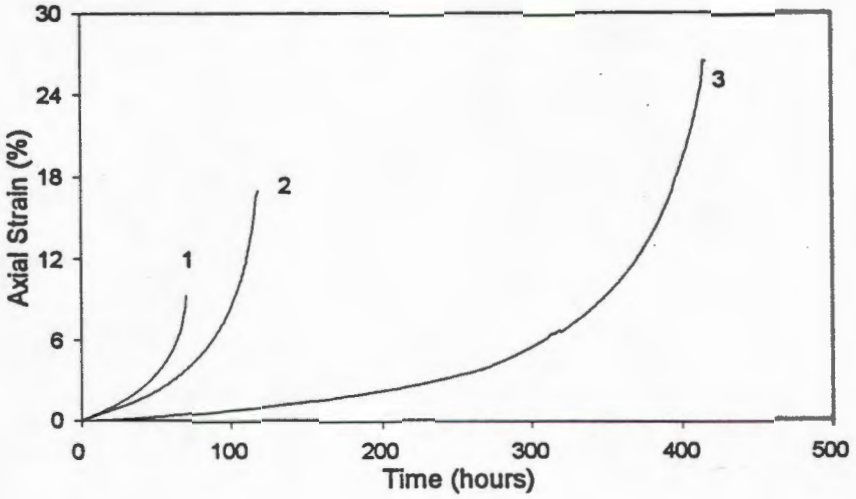

Figure 5.52(a).

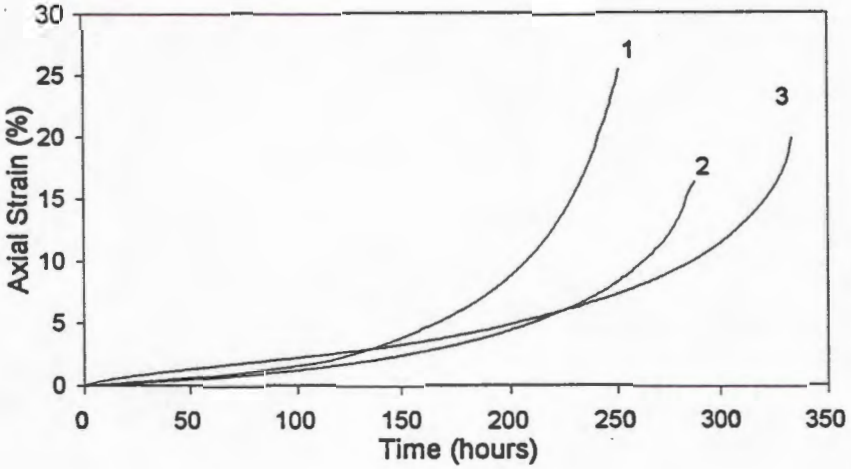

Figure 5.52(b)

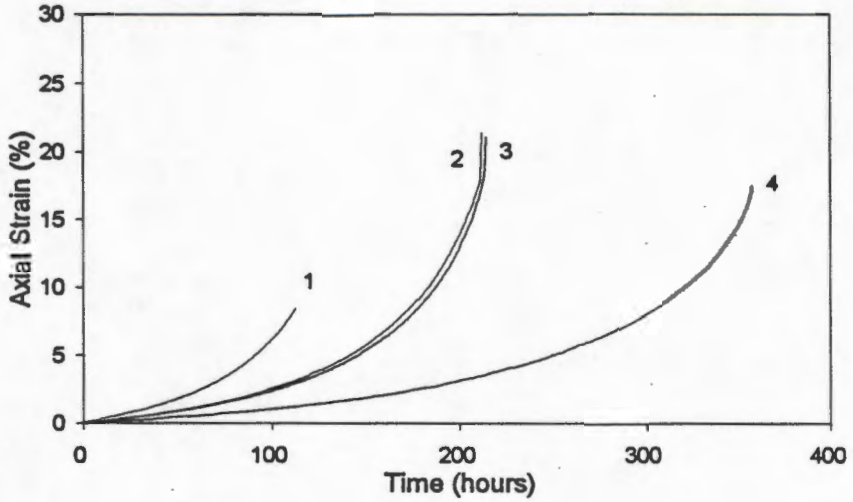

Figure 5.52(c).

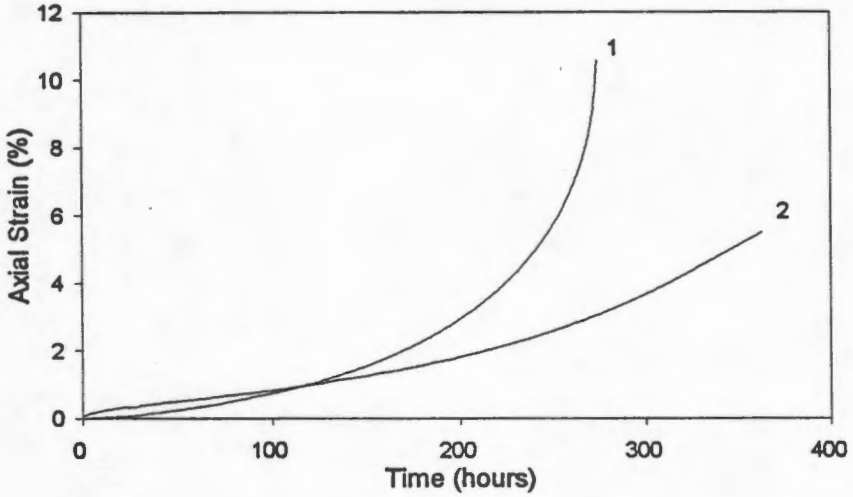

Figure 5.52(d).

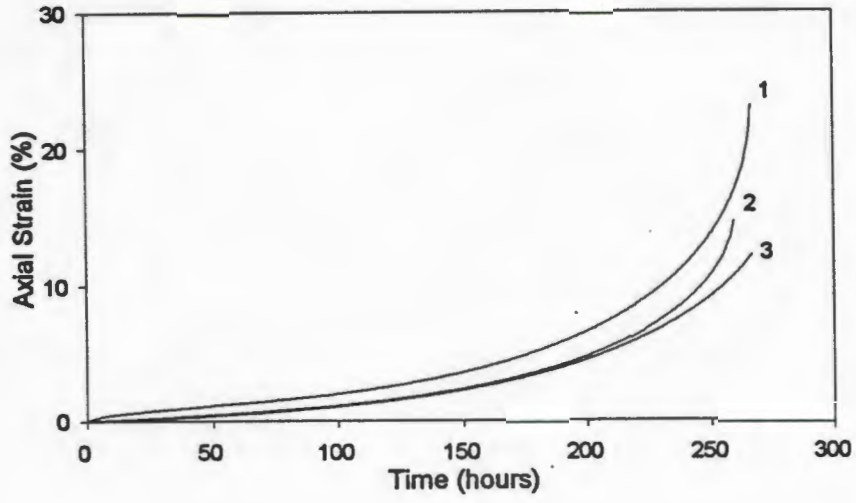

Figure 5.52(e)

Figure 5.52. The creep curves of DS MarM-002 tested at 900°C/300MPa are shown for (a) the as received condition, (b) the 1220°C/2h, (c) the VRSHT 1220°C, (d) the VRSHT 1240°C and (e) the VRSHT 1260°C specimens.

5.10.2a Shape of the Creep Curves

An interesting feature of the creep curves is that in most cases the curves are dominated by tertiary creep and therefore display a steadily increasing strain rate for most of the creep life. Yet, for the 1220°C/2h, VRSHT 1240°C and 1260°C specimens, one curve in each graph exhibits the classical primary, secondary and tertiary stages of creep (specimens 3, 2 and 1 in Figs 5.52(b), (d), and (e) respectively). The creep stages can be seen fairly readily in the respective 1220°C/2h, VRSHT 1240°C and VRSHT 1260°C specimens, although the tertiary creep stage is not as pronounced in the VRSHT 1240°C specimen (Fig. 5.52d).

The curves displaying primary, secondary and tertiary creep stages are re-plotted as incremental strain versus time graphs in Figs. 5.53(a) to (c), where the incremental strain is defined as the increase in strain over every 30 minute interval. There is considerable "noise" in these curves, but the overall trend is one in which the curve decreases during primary creep (decreasing creep rate), remains horizontal during secondary creep (constant strain rate) and increases

during tertiary creep. The primary, secondary and tertiary creep stages are readily distinguished in the 1220°C/2h and the VRSHT 1260°C specimens (Figs. 5.53a and c), but the distinction between secondary and tertiary creep is more difficult to distinguish in the VRSHT 1240°C specimen (Fig. 5.53b). This is because tertiary creep in this specimen is composed of a more gradual increase in strain rate. However, in the strain-time curve (Fig. 5.52d) it is readily apparent that the secondary creep stage begins after about 25 hours and ends after approximately 125 hours. For the 1220°C/2h, VRSHT 1240°C and the VRSHT 1260°C specimens (Figs. 5.53a, b and c), the primary creep stage is seen to occupy about 25 hours of the creep life before the transition to secondary creep, which lasts 75 to 100 hours.

The secondary creep strain rate was measured to be approximately 5.5×10^{-6} s^{-1} for the 1220°C/2h and VRSHT 1260°C specimens and 2.8×10^{-6} s^{-1} for the VRSHT 1240°C specimens. It is interesting to note that these curves displayed the greatest creep lives of the specimens in the three heat treated conditions. This is indicative of rapid strain hardening in the primary creep stage which results in a low secondary creep strain rate and a long creep life.

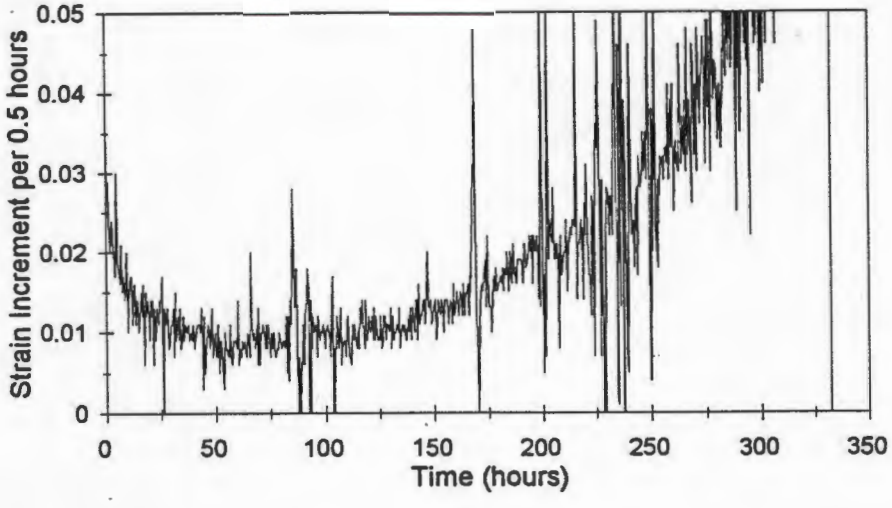

Figure 5.53a).

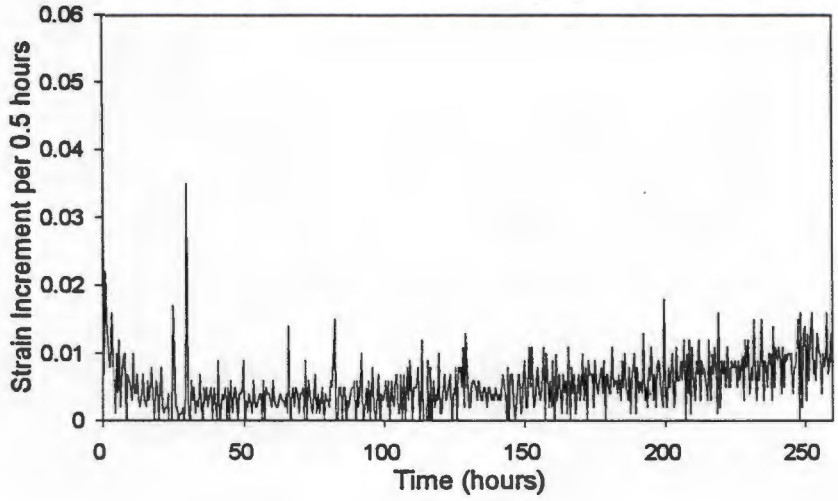

Figure 5.53b).

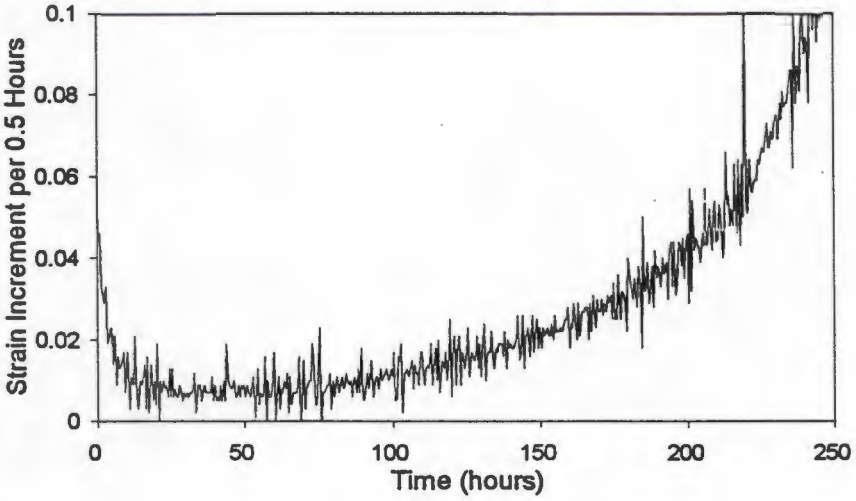

Figure 5.53c).

Figure 5.53. The increase in strain with the passage of time during creep is shown for (a) the 1220°C/2h specimen, (b) the VRSHT 1220°C, (c) the VRSHT 1240°C and (d) the VRSHT 1260°C specimen.

5.10.2b The Microstructure of the Failed Creep Specimens

Following creep failure the creep specimens were sectioned parallel to the stress axis and the microstructures were examined. The results of this investigation are detailed below.

(i) The As Received Specimen

The microstructure of the as received specimen is shown in Figs. 5.54 to 5.57. The most obvious feature of all of the fractured creep specimens is the γ' rafting which occurred during the creep process. The secondary γ' precipitates have coalesced and coarsened to form long rafts or lamellae oriented at right angles to the stress axis (Fig. 5.55). These rafts are not ideally aligned but are "wavy", and hence not optimally shaped to prevent dislocation cross slip and climb. The thickness of the γ' rafts is approximately 0.53 ± 0.26 μm. The relatively large error associated with this figure is not only indicative of the variation in γ' thickness, but also arises from the many, large junctions where two rafts intersect each other. This latter detail is in fact applicable to all of the specimens discussed. The primary γ' precipitates have also coarsened to form rafts, although their initial oblong morphologies may still be discerned (Fig. 5.56).

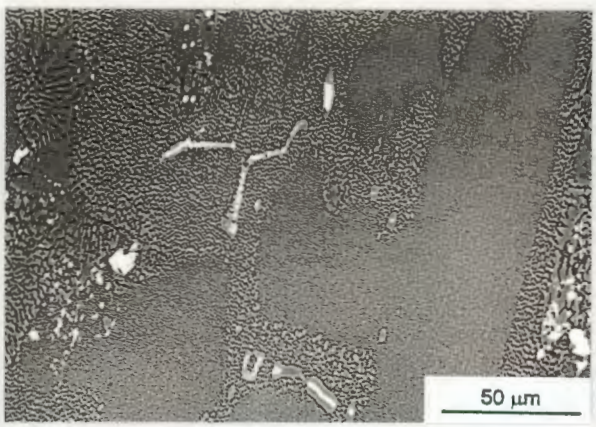

Figure 5.54. The microstructure of a failed creep specimen tested in the as received condition is shown here. The secondary γ' and the primary γ' have undergone rafting .

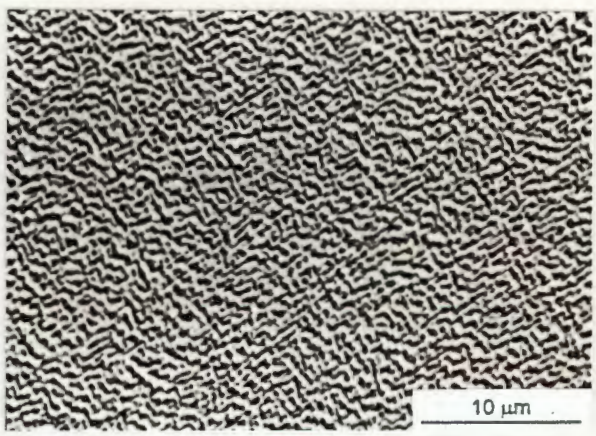

Figure 5.55. The γ' rafts of the as received creep specimen are seen to be wavy, but oriented at right angles to the stress axis. The stress axis is top-bottom in this micrograph.

Creep cavities were found to be almost always associated with carbides. It is not entirely clear, but it appears that cavities initiate largely at the carbide / γ' envelope interface. Smaller, less developed cavities were also seen to initiate at

the eutectic γ' / γ matrix interface and the primary γ' / γ matrix interface (Fig. 5.57), but these fractures appear to be of secondary importance.

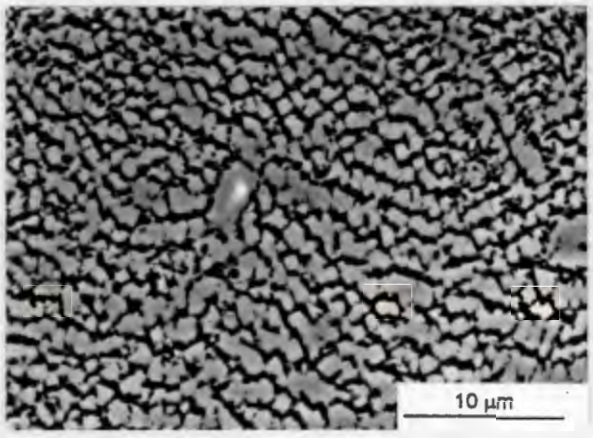

Figure 5.56. The primary γ' of the as received creep specimen has rafted but is generally oblong in morphology.

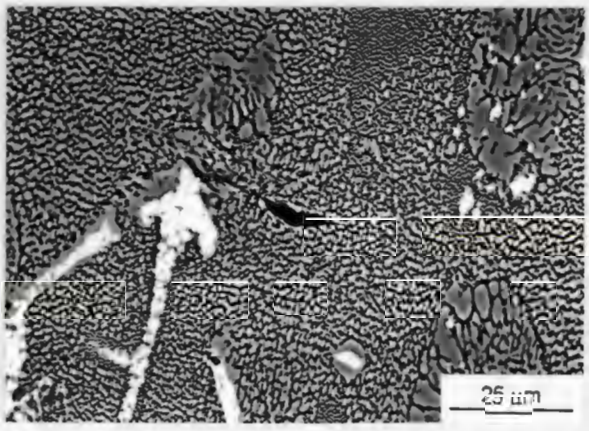

Figure 5.57. A creep cavity has initiated along the primary γ' - matrix interface.

(ii) 1220°C/2h

The microstructure of the 1220°C/2h specimen is shown in Figs. 5.58 to 5.61. The secondary γ' precipitates have coalesced and coarsened to form long rafts or lamellae oriented at right angles to the stress axis (Fig. 5.59). These rafts are again not ideally aligned but are "wavy". The degree of alignment is, however, greater than that seen in the as received specimen. The thickness of the γ' rafts is approximately 0.50 ± 0.27 µm. The primary γ' retains its oblong, blocky shape and coalescence is common amongst the particles (Fig. 5.60), but no significant γ' rafting has occured.

Creep cavities were found to be commonly associated with carbides (Fig. 5.61), but cavities were seen along the γ' / matrix interfaces of the eutectic γ' and primary γ'.

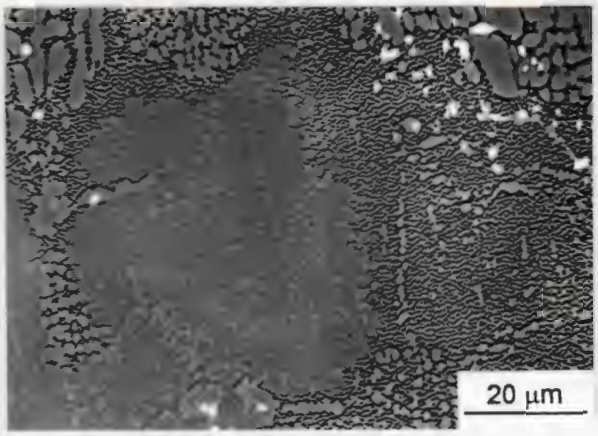

Figure 5.58. The microstructure of a failed 1220°C/2h creep specimen is shown here. The secondary γ' has formed rafts and the primary γ' has coalesced.

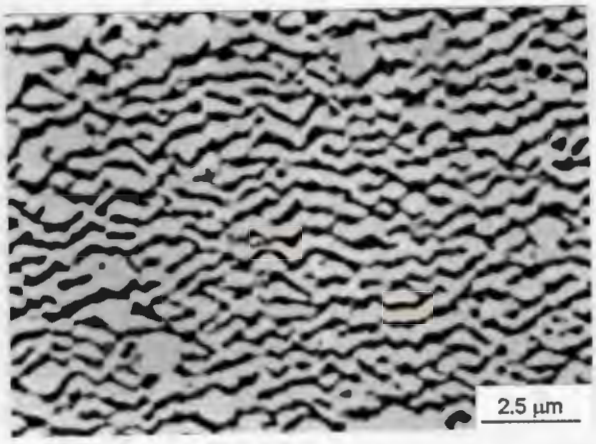

Figure 5.59. The γ' rafts of the 1220°C/2h creep specimen are seen to be wavy, but oriented at right angles to the stress axis. The stress axis is top-bottom in this micrograph.

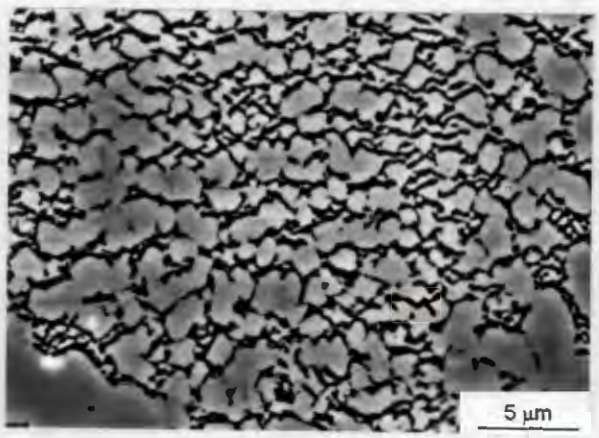

Figure 5.60. The primary γ' of the 1220°C/2h creep specimen has coalesced but is generally oblong in morphology.

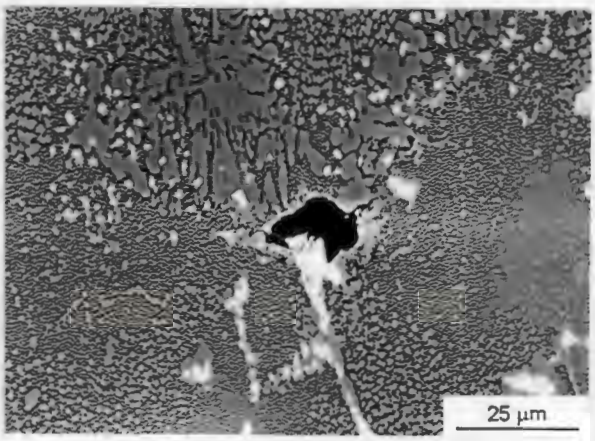

Figure 5.61. Cavity formation is associated primarily with the carbides. Secondary points of cavity initiation are along the γ'-matrix interface of the eutectic γ' and primary γ'.

(iii) VRSHT 1220°C

The γ' rafts formed from the secondary γ' (Figs. 5.62 and 5.63) are approximately 0.50 ± 0.26 μm in thickness and, qualitatively, exhibits a degree of waviness comparable with the 1220°C/2h creep specimen. The primary γ' remains oblong, but particles have begun to combine and there seems to be some alignment of these precipitates in directions parallel and perpendicular to the stress axis (Fig. 5.63). Cavitation is associated with the carbides, eutectic γ' and primary γ'

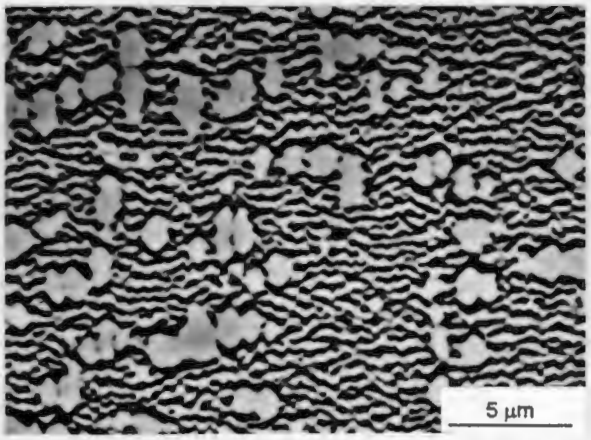

Figure 5.62. Rafted secondary γ' and unrafted primary γ' is visible in the VRSHT 1220°C specimen.

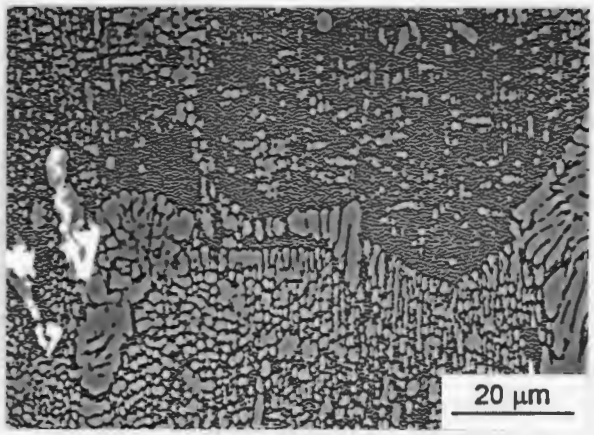

Figure 5.63. Gamma prime rafting and partial alignment of the primary γ' may be seen in the VRSHT 1220°C specimen.

(iv) VRSHT 1240°C

Micrographs of the VRSHT 1240°C specimen may be seen in Figs. 5.64 to 5.66. Creep cavitation is observed initiating within carbides, along the γ' envelope / matrix interface, primary γ' / matrix interface and possibly the secondary γ' / matrix interface in Fig. 5.64.

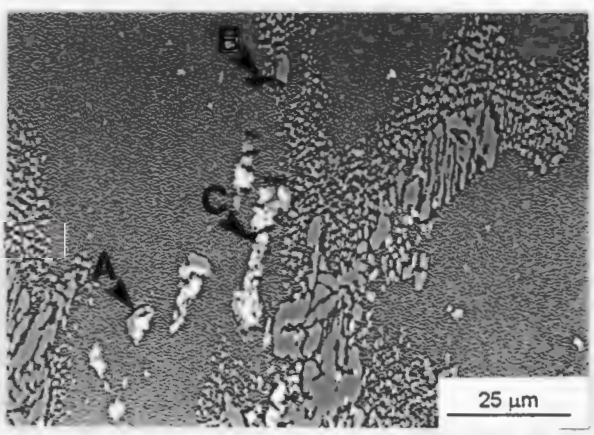

Figure 5.64. In this micrograph of the VRSHT 1240°C specimen, creep cavities are seen initiating along the carbide envelope-matrix interface (A), primary γ'-matrix interface (B) and within carbides (C).

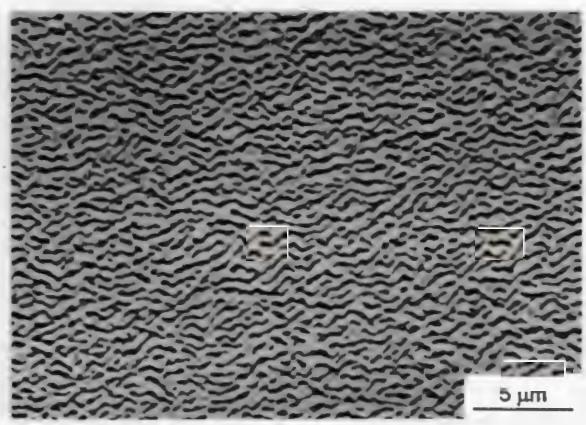

Figure 5.65. Gamma prime rafts in the VRSHT 1240°C specimen are about 0.36 μm thick and are slightly wavy in morphology.

The secondary γ' raft thickness is 0.36 ± 0.18 μm and the waviness of the rafts is not dissimilar to the 1220°C/2h and the VRSHT 1220°C creep specimens (Fig. 5.65). The primary γ' has not rafted, although there is some particle coalescence (Fig. 5.66).

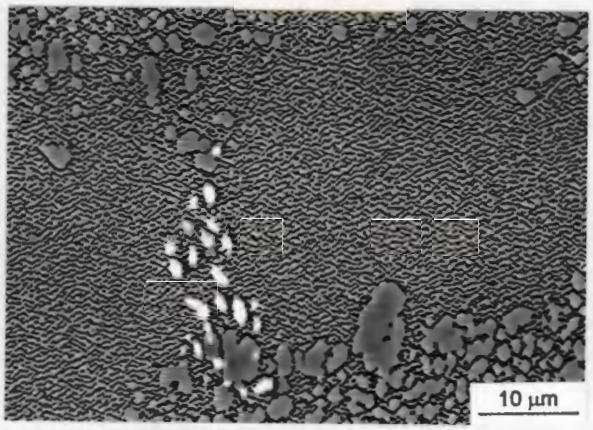

Figure 5.66. Although rafting of the secondary γ has occurred in the VRSHT 1240°C specimen, the primary γ' has not undergone rafting.

(v) VRSHT 1260°C

Initiation of creep failure was associated with carbides (Fig. 5.67), as well as the eutectic γ'-matrix interface. Additionally, there seemed to be a higher incidence of cavitation within the dendrites than in specimens that were solution treated at lower temperatures (i.e. cavitation initiating along the γ' raft-matrix interface). The gamma prime rafts may be seen in Fig. 5.68 and are approximately 0.45 ± 0.11 μm in thickness. The degree of alignment (or waviness) of the rafts is similar to that seen in the VRSHT 1220°C, 1240°C and 1220°/2h specimens.

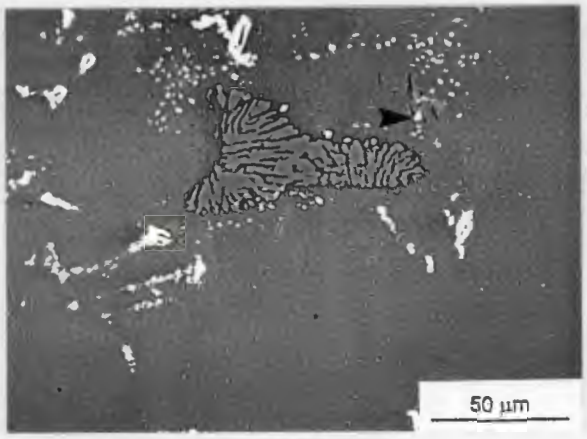

Figure 5.67. Cavitation (arrowed) associated with Hf-carbides and possibly along the γ' raft-matrix interface is seen in this micrograph of the VRSHT 1260°C specimen. The stress axis is left-right in this micrograph.

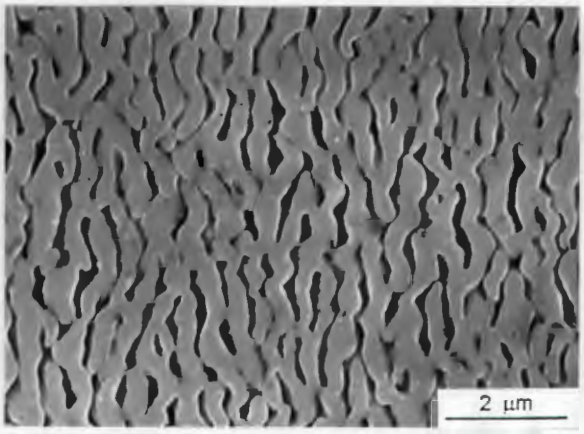

Figure 5.68. The gamma prime rafts of the VRSHT 1260°C specimen are about 0.45 µm thick. The microstructure was recorded in the SEM using secondary electrons and the stress axis is left-right in this photograph.

6. Discussion

6.1 Microstructure and Heat Treatment of MarM-002

The effect of the solution and ageing heat treatments on the microstructure of MarM-002 are discussed below, together with the incipient melting behaviour.

6.1.1 Solution Heat Treatment

(i) Gamma Prime Dissolution

The response of the gamma prime precipitates to the solution treatment temperatures of 1220°C, 1240°C and 1260°C indicates that the γ' solvus is 1260°C (Fig. 6.1). Gamma prime precipitates begin to dissolve at 1220°C and the remaining precipitates are completely dissolved by 1260°C. On a more local scale, there is a difference between the γ' solvus temperatures of the dendritic and interdendritic regions. Dissolution begins in the dendritic regions at 1220°C and is completed in these regions by 1240°C. However, precipitates in the interdendritic areas persist to 1260°C. The difference in local γ' solvus temperature is attributed to the chemical segregation that occurs during the solidification of the material. Gamma prime formers (Al, Ti and Ta) segregate to the interdendritic regions during solidification (Tables 5.1 and 5.2). Since these elements raise the γ' solvus temperature[13], precipitates in these areas are the last to dissolve. Conversely, the gamma formers Cr, Co and W segregate to the dendritic regions and lower the local solvus temperature.

Two factors that influence the dissolution process are the surface:volume ratio and the elastic interaction stresses between neighbouring precipitates. A reduction in these parameters is a driving force for precipitate dissolution. The surface:volume ratio and the elastic interaction stress may be altered by morphological changes, particle coalescence and precipitate distribution. Morphological changes occur by cuboidal precipitates becoming spheroidal, in order to decrease the surface:volume ratio. Coalescence of neighbouring precipitates may occur to decrease the number of γ-γ' interfaces and lower the surface:volume ratio and the interaction stresses. In regions containing a relatively high density of precipitates, the γ' particles arrange themselves into

linear arrays to reduce the interaction stresses between precipitates. The precipitates are typically aligned along the [001] directions, since the elastic modulus and the interaction stresses are at a minimum along this direction[19,20]. Cube faces of the precipitates are also aligned along the [001] directions.

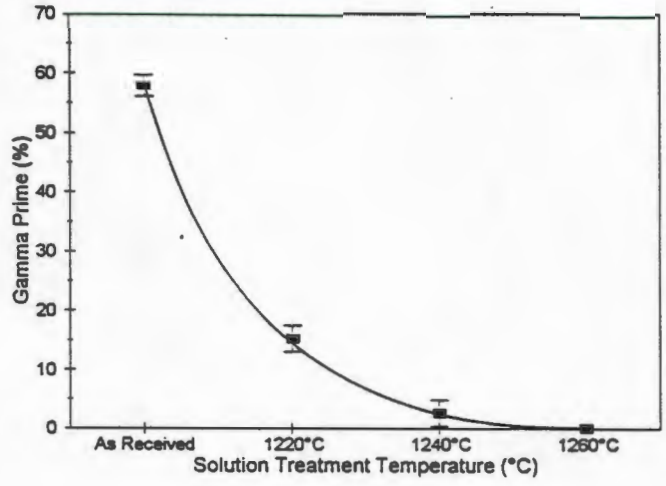

(a)

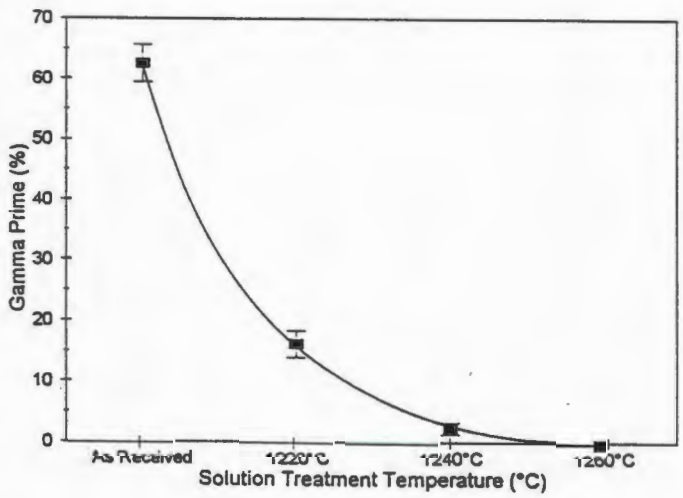

(b)

Figure 6.1. The effect of solution treatment temperature on the dissolution of gamma prime in (a) DS MarM-002 and (b) CC MarM-002

The DS alloy solution treated at 1220°C contains a greater number of cuboidal precipitates arranged in linear arrays than the CC material. Precipitates in the CC alloy are more spheroidal. This suggests that the precipitate-matrix misfit of

the DS alloy is higher than that of the CC alloy, since cuboidal precipitates typically have a higher misfit than spheroidal precipitates[19,20]. In turn, this indicates that the phase chemistries of the DS and CC alloys may be different, as misfit is dependent on the lattice parameters of the phases and the phase chemistry. The difference in phase chemistry may be caused by the different casting processes used for the two alloys. These differences are minor however, as the solvus temperatures of the materials do not differ.

(ii) Eutectic γ' Dissolution

By definition, a eutectic phase should dissolve at one specific temperature, but in this case the composition of the eutectic varies sufficiently for it to dissolve over a range of temperatures. The eutectic γ' has a higher solvus temperature than the γ' precipitates, since it begins to dissolve at temperatures in the region of 1260°C (Fig. 6.2). At this temperature the volume fraction of eutectic γ' decreases from an initial 15% to 2%. The eutectic γ' is completely dissolved at temperatures of approximately 1280°C, but incipient melting is noted at this temperature. The solvus temperature of the eutectic γ' may be considered to be 1280°C.

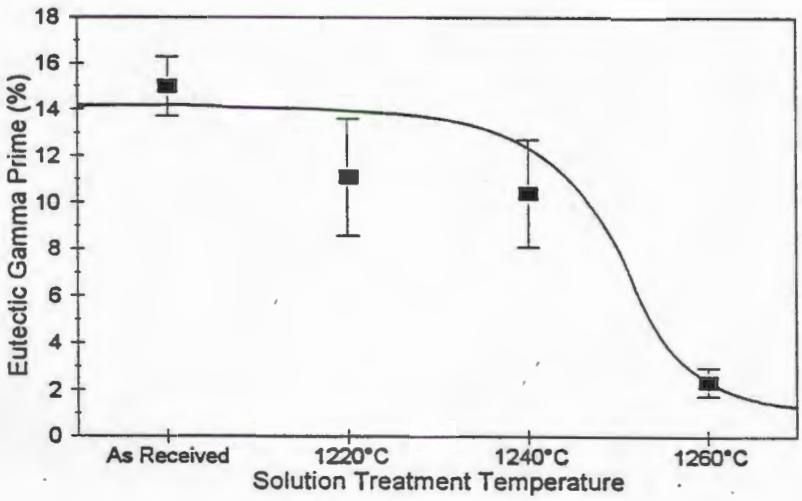

Figure 6.2(a)

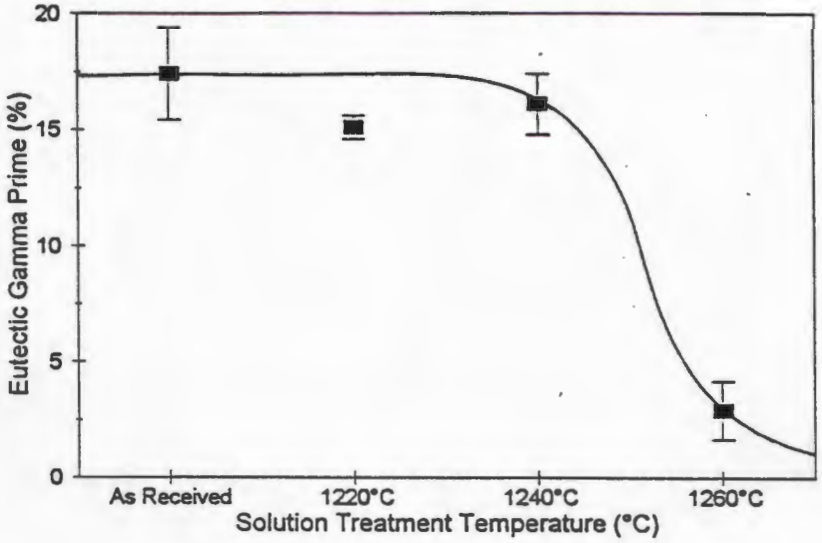

Figure 6.2(b)

Figure 6.2. The effect of solution treatment temperature on the dissolution of eutectic γ' in (a) DS MarM-002 and (b) CC MarM-002

Below 1260°C no eutectic γ' dissolves. Instead the eutectic γ' coarsens through particle coalescence and Ostwald ripening. Coarsening can occur to such an extent that the eutectic γ' forms an interconnected mass.

(iii) Carbide Fragmentation and Formation

Carbides in the as cast MarM-002 are of the blocky type (Ta and Hf rich) and the script type (Ta and Ti rich). These are the MC-1 and MC-2 carbides commonly found in polycrystalline nickel-base superalloys[23-25]. In as cast CC MarM-002, it was seen that the MC-1 and MC-2 carbides are not surrounded by γ' envelopes and are not fragmented. This is in contrast to the as received DS material and all the solution treated CC and DS specimens, where carbide fragmentation and the γ' envelopes are observed. Additionally, the MC-3 hafnium carbide is found in the DS and solution treated CC alloys. The difference in carbide characteristics arises because the DS MarM-002 had been previously heat treated, whereas the CC material was not. On exposure to heat, the MC-1 and MC-2 carbides break down through a process of fragmentation, thereby liberating carbon and hafnium for the production of the MC-3 hafnium carbide.

MC-3 formation is thermodynamically favoured because hafnium is a stronger carbide former than tantalum or titanium[24]. HfC forms in the γ phase of the eutectic γ-γ', since both hafnium and the script and blocky carbides are located preferentially in the interdendritic regions. Thus, fragmentation of carbides and the presence of HfC is seen in heat treated MarM-002 but not in the as cast MarM-002. Fragmentation of the carbides is displayed over the entire range of solution temperatures investigated (1220°-1280°C), without any noticeable carbide dissolution.

Titanium and tantalum are released by the fragmenting carbides to form γ' envelopes around the carbides, since they are strong gamma prime formers. The γ' solvus temperature is raised by these two elements and hence the envelope can persist to 1260°C before dissolving.

6.1.2 Incipient Melting

Incipient melting in as cast MarM-002 occurs at 1240°C and is due to the presence of a low melting point cellular Ni-Hf compound. The presence of low melting point Ni-Hf phases is expected in polycrystalline superalloys, particularly since hafnium segregates strongly to the interdendritic regions. The exact composition of the Ni-Hf phase seen in MarM-002 is unknown. Melting is accompanied by the formation of HfC and a fine eutectic γ-γ'. The HfC is formed from hafnium and carbon released by the melting process and is found within the Ni-Hf compound. Partial decomposition of the Ni-Hf compound and interaction with the surrounding material results in the formation of the fine eutectic γ-γ' around the Ni-Hf compound. Similar effects concerning HfC and eutectic γ-γ' formation are reported by Yunrong et al[40,41].

The varied rate solution heat treatment enabled solution treatment at 1240° and 1260°C without incipient melting. Presumably the VRSHT removed the Ni-Hf compound by transforming the Ni-Hf compound to eutectic γ-γ' and HfC, and by dissolving the Ni-Hf compound. Above 1260°C incipient melting occurred even with the VRSHT. This suggests that more time at temperatures below 1280°C is needed for complete breakdown of the Ni-Hf phase. The time required for this would unfortunately be impractical for heat treatment practice (40+ hours of total solution heat treatment time).

6.1.3 Ageing Heat Treatment

Nucleation and growth of the gamma prime precipitates is caused by the 1050°C/12h + 870°C/16h ageing heat treatment. The average γ' cube length for almost all of the specimens was approximately 0.25 μm. This is virtually identical to the 0.27 μm cube length seen in the as received material. Only the VRSHT 1220°C specimen had a larger precipitate size of 0.35 μm. However, the confidence interval for all of the different specimens was 0.50 to 0.11 μm, and therefore the significance of this difference in γ' size is arguable.

The eutectic γ' which had not been previously dissolved during the solution treatment was coarsened by the ageing heat treatment. Minor eutectic γ' coarsening had occurred during the solution treatment of the 1220°C/2h specimens, but following the ageing heat treatment the eutectic γ' had coalesced to form large blocky particles and lamellae. Coarsening of the eutectic γ' in the VRSHT specimens occurred during solution treatment, and the ageing heat treatment served to ripen the particles further.

6.2 Microstructure-Tensile Properties

6.2.1 Tensile Strength

There are significant differences in the tensile strength of DS MarM-002 solution treated at different temperatures. The VRSHT 1260°C specimens displayed a tensile strength ranging from 891-929 MPa. This indicates a 10% strength advantage over the specimens solution treated at lower temperatures. The superior tensile properties of the VRSHT 1260°C specimens may be attributed to the high temperature solution treatment that was used. The greatest effect of the VRSHT at 1260°C is the large scale dissolution of eutectic γ'. This decrease in eutectic γ' can lead to three effects; firstly the volume fraction of fine, more effectively strengthening γ' is increased, secondly the number of failure initiation sites is reduced, and thirdly precipitates with poor strengthening properties are removed. These factors are discussed below.

(i) Increased Volume Fraction of Fine γ'

As the amount of fine γ' increases, the number of dislocation obstacles increases and the tensile strength consequently increases[9]. Equation 2.7 indicates that the flow stress is proportional to $(f)^{1/2}$, where f is the volume fraction of precipitates. It can be shown that $(f)^{1/2}$ for the VRSHT 1260°C material is approximately 13% greater than that of material solution treated at lower temperatures. This figure more or less corresponds to the difference in tensile strength. The correspondence between $(f)^{1/2}$ and tensile strength may simply be fortuitous, but may be calculated as follows: MarM-002, in the as received condition, can be considered to be composed of 15% eutectic γ' and 2% carbides. The remainder of the material (83%) is made up of γ' and γ, where the γ':γ ratio is 0.6:1. Therefore the γ' comprises 50% of the total alloy. If the volume fraction of eutectic γ' decreases from 15% to 2%, a difference of 13%, the volume fraction of fine γ' can be said to increase by 13%, to 63% of the alloy. Then $(f)^{1/2}$ is $(0.63)^{1/2} = 0.79$ for the VRSHT 1260°C specimens, and $(0.5)^{1/2} = 0.70$ for the as received material. The $(f)^{1/2}$ for the VRSHT 1260°C specimens is, thus, 13% greater than the as received condition, or any condition where the solution treatment does not dissolve the eutectic γ' to any significant extent. This is approximately the tensile strength difference between the two conditions.

(ii) Decrease in the Number of Failure Initiation Sites

The second consequence of eutectic γ' dissolution is the decrease in the number of failure initiation sites[72]. Failure in MarM-002 initiates at both carbides and the eutectic γ'. The decrease in the amount of eutectic γ' decreases the number of failure initiation sites, thereby delaying the onset of tensile failure. The tensile strength is increased in this way.

Carbides and the eutectic γ' are usually found in close proximity to each other. Therefore the dissolution of the eutectic γ' may also affect failure initiation at the carbide sites. Failure in both carbides and eutectic γ' is attributed to impinging slip bands and localised shear[72,73]. Removal of the eutectic γ' may reduce the likelihood of localised shear, since this relatively weak phase is replaced by the stronger fine γ'. This may reduce the intensity of deformation that is transferred

to the carbides. It is then possible that a greater nominal stress is required to cause localised shear in the carbides.

(iii) Removal of Less Effective Strengtheners

The greatest difficulty of dislocation motion is on entering the γ' particle against misfit stresses and solid solution strengthening. In addition an anti-phase boundary (APB) must be formed by any dislocation entering the precipitate[55,66]. Once the dislocation has entered the precipitate, dislocation motion is relatively easy. Hence, a large number of γ-γ' interfaces are required for optimum tensile strength. For a given amount of γ', smaller precipitates present many more γ-γ' interfaces than larger precipitates. Thus, smaller precipitates are more effective as dislocation obstacles. The eutectic γ' is a poor strengthener since it exists in the form of relatively large particles. The VRSHT specimens contain a particularly large eutectic γ' because of the long exposure to heat during the solution treatment. Dissolving the eutectic γ' and precipitating a finer particle in its place should contribute to greater strength.

The 1220°C/2h and the VRSHT 1240°C tensile specimens possess similar, intermediate tensile strengths. The benefits of eutectic dissolution are not seen in either of these specimens as the solution temperatures are too low to dissolve the eutectic γ'. Factors contributing to the intermediate tensile strengths of these specimens are the presence of the primary γ' and the coarse eutectic γ'. The 1220°C/2h specimens possess considerably more primary γ' than the VRSHT 1240°C material. Due to its larger size, the primary γ' is less effective as a strengthener than the smaller secondary γ'. On this basis the 1220°C/2h specimens would not be expected to be as strong as the VRSHT 1240°C material. This effect is, however, offset by the coarser eutectic γ' that is seen in the VRSHT 1240°C specimens; the coarse eutectic γ' having a lower strengthening effect. The presence of the eutectic γ' and large primary γ' in these specimens leads to localised strains and failure at the carbide and eutectic γ' sites.

The low tensile strengths of the as received and the VRSHT 1220°C specimens are again due to the presence of primary γ' and eutectic γ'. The as received

condition contains considerably more primary γ' than any other heat treated condition, and it also contains a significant amount of eutectic γ'. The "weak link" phases (primary γ', eutectic γ', carbides) are all found in the interdendritic regions. Thus, these regions are expected to exhibit lower strengths than the dendritic regions, which are composed mainly of secondary γ'. Early failure is the result, particularly at the carbide sites.

There are two microstructural features that suggest that the VRSHT 1220°C specimens should be stronger than the as received material. Firstly, the VRSHT 1220°C specimens have less primary γ' than the as received specimens. Secondly, a fine γ' is found amongst the primary γ', which may strengthen these interdendritic regions. However, these features are offset by the extensive coalescence of the eutectic γ' during the long solution treatment period. The cumulative effects may lead to a tensile strength that is no greater than the as received material. Additionally, the decrease in the amount of primary γ' and the presence of the finer γ' in the VRSHT 1220°C specimens may provide negligible increases in tensile strength.

Although solution treated at the same final temperature, the VRSHT 1220°C specimens appear to have more primary γ' in the dendrites and a coarser eutectic γ' than the 1220°C/2h material. This results in the VRSHT 1220°C condition being weaker than the 1220°C/2h specimens.

6.2.2 Proof Stress

The 0.2% proof stress may be regarded as a measure of the difficulty with which dislocations become mobile during tensile deformation. The VRSHT 1260°C Test 2 specimens exhibit the largest proof strengths, suggesting that the Test 1 specimens would have displayed similar behaviour. This may be explained by the large number of fine γ' precipitates and the consequent γ-γ' interfaces that oppose dislocation motion (Fig. 2.11). The material solution treated at lower temperatures do not have as many γ-γ' interfaces, since they contain the larger primary γ'. Therefore these specimens cannot resist dislocation motion to the same degree. This is aggravated by the coarse eutectic γ'. The proof strengths are thus lower for these specimens.

Although differences in microstructure discussed in section 6.2.1 have profound effects on the tensile strengths of the specimens, they do not appear to have much effect on the 0.2% proof stresses of the 1220°C/2h, VRSHT 1220°C or the VRSHT 1240°C specimens. The lower proof strength of the as received specimen is due to the large primary γ' in the interdendritic regions, which is more prevalent in the as received specimens than the other heat treated specimens. Additionally, because there is no secondary γ' found amongst the primary γ' of the as received material, the regions of primary γ' do not receive the benefit of secondary γ' strengthening.

6.2.3 Elongation

There are no significant differences in the elongation behaviour of the tensile specimens. This suggests that a certain strain is required to cause fracture in the material. Thus, it may be plausible that cracking at the main regions of failure is strain controlled. It should be remembered that localised strains and impinging slip bands are thought to initiate cracking at these carbide and eutectic γ' sites[72,73]. The strains and slip bands may be aggravated or resisted by the phases surrounding and composing the failure initiation sites. Different tensile loads are required to bring about this level of strain for the various specimens, because of the dissimilar microstructures. Therefore, although the tensile strengths differ, the elongation remains constant.

The correlation between decreased ductility and the presence of the eutectic γ-γ', noted by Walston et al[72], was not seen in this study. This may be due to the presence of the carbides, which initiate early failure. Fracture may occur before any differences in ductility arising from eutectic γ' dissolution can be seen.

6.3 Microstructure-Creep Properties

6.3.1 Creep Life

The effective creep lives of the different heat treated conditions can be compared by examining the shortest creep life in each condition. On this basis, the 1220°C/2h, VRSHT 1240°C and VRSHT 1260°C conditions are equivalent and possess the longest creep lives (~260 hours). It is surprising to note that

the VRSHT 1260°C specimens contain the largest volume fraction of fine γ', yet do not exhibit the longest creep lives. This is contradictory to the findings of Jackson et al[88], who measured increased creep life with increased volume fraction of fine γ'. The discrepancy is due to the final failure process in DS MarM-002, which appears to be controlled by the carbide characteristics and distribution. Any benefit arising from the increase in volume fraction of fine γ' is negated by relatively early initiation of failure at the carbide sites. The shape of the carbides may play a role in carbide failure, presumably because of stress concentration effects. Erickson et al[96] have suggested that the script carbides commonly seen in MarM-002 are more susceptible to cracking than blocky carbides. It should also be noted that the largest volume fraction of fine γ' measured by Jackson et al[88] (Fig. 2.13) is in the region of 50%, while the volume fraction of γ' in MarM-002 is 60%. It is not impossible that a saturation point for the volume fraction of γ' may exist, above which there is no added benefit from further increases in the amount of γ' because of carbide failure. On the other hand, Erickson et al[9] noted an increase in stress-rupture properties with increased volume fraction γ' in a MarM-247 derivative alloy, which has a similar quantity of γ' as MarM-002. Unfortunately, neither Erickson et al[9] nor Jackson et al[88] mention the failure initiation sites and the effect of the carbides is unknown in these alloys.

The factors contributing to the maximum creep lives (~400 hours) are unclear. A tentative suggestion is that the difficulty of failure initiation may have a strong effect. Failure initiation is associated with tertiary creep, which constitutes a large part of the creep life seen in these specimens[52,77,85]. This implies that in some specimens, the carbides and eutectic γ' were distributed in such a way that strain build up was not localised at these phases, delaying the onset of cavitation. Possibly the strain was accommodated by homogeneous plastic deformation in the primary γ', eutectic γ' or carbide envelopes, rather than localised deformation.

6.3.2 Creep Life Scatter

A benefit of the increased eutectic γ' and primary γ' dissolution in the VRSHT 1260°C specimens is the decrease in creep life scatter. The reduction in the volume fraction of the eutectic γ' and removal of the primary γ' "refines" the

microstructure of the specimens. Since the mechanical properties of materials are directly related to the microstructure, this suggests that the microstructures have been refined to a point where they are essentially the same and thus exhibit similar creep behaviour. Refinements in microstructure through heat treatment and accompanying decreases in creep life scatter have also been seen in the alloy IN738LC (Ref.44).

The greater degree of scatter seen in the specimens solution treated at lower temperatures can be attributed to the presence of the eutectic γ' and the primary γ'. The specimens tested in the as received condition displayed the greatest scatter in creep life. The 1220°C/2h and the VRSHT 1240°C specimens contained less primary γ' and creep life scatter was decreased. The VRSHT 1220°C specimens exhibited a large amount of creep life scatter, possibly because the primary γ' and the eutectic γ' were coarsened by the long solution treatment period.

Unlike the tensile behaviour, failure during creep is not controlled by the overall specimen strain. It is possible that creep failure may initiate at a smaller number of carbide or eutectic γ' sites than tensile failure. This may result from preferred cavitation at selected carbide or eutectic γ' sites, rather than cavitation across the entire cross section of the alloy. Cavitation may form only in selected areas because of relatively severe stress states, due to factors such as the orientation and morphology of carbides, neighbouring weak phases or grain boundaries.

6.3.3 Shape of the Creep Curves

The majority of the creep curves are dominated by tertiary creep. Primary and secondary creep are non-existent or are difficult to distinguish in these specimens. A possible explanation can be rationalised on the basis of dislocation behaviour and the resolved shear stress. It should be remembered that primary creep involves the activation of dislocation sources and the formation of a steady state dislocation network[76-82]. Secondary creep involves the equilibrium between dislocation work hardening and recovery. Where the creep curves do not reveal primary creep it is possible that the applied load was severe enough to cause rapid formation of a dislocation network. This is plausible, considering that dislocations are easily nucleated from the grain

boundaries[83]. The dislocation network may have developed in a shorter time span than the 30 minute period used to measure changes in creep strain.

The lack of secondary creep suggests that there was no balance between work hardening and recovery, but that dislocation climb and plastic deformation dominated over the recovery processes. Therefore, the resolved shear stresses must have been relatively large in these specimens. Hence, the steadily increasing strain rate characteristic of tertiary creep dominated the curve.

Effect of Grain Orientation

Some specimens did exhibit primary and secondary creep. It is possible that grain orientation may have played a role in determining whether a specimen would exhibit these creep stages. Through Schmid's Law, the orientation of the grains alters the resolved shear stress. The resolved shear stress can affect both primary and secondary creep. Firstly, the formation of the dislocation network during primary creep is dependent on the resolved shear stress active in the material. The greater the resolved stress, the faster the dislocation network is formed. Secondly, during secondary creep the resolved shear stress affects the equilibrium between work hardening and recovery. For equilibrium to be maintained the resolved stress must be below a critical level.

In the specimens that exhibit primary and secondary creep it is likely that the resolved stresses are below the critical value. During primary creep, the low resolved stress results in the slow formation of the dislocation network. Under these conditions the primary creep stage becomes more noticeable and is measurable with the testing apparatus. Similarly, the equilibrium essential for secondary creep is achieved.

In both DS and single crystal superalloys the [001] direction is the preferred direction of grain growth during solidification[3,4], but it is not impossible for other orientations to form. Thus it is possible that the specimens which exhibited primary and secondary creep were not oriented along the [001] direction. Instead, the orientation may have been one with a lower Schmid factor. For example, the [111] orientation has a lower resolved shear stress than the [001] orientation[78]. Since the resolved stress of the [111] orientation is lower, the

presence of the primary and secondary stages of creep would be more likely. Hence, an argument exists for the proposal that specimens which reveal primary and secondary creep have strong orientations that are not in the [001] direction. This is supported by the fact that the majority of the specimens are expected to have [001] orientations and did not exhibit the three stages of creep. Unfortunately accurate orientation determination was not within the scope of this study.

6.3.4 Gamma Prime Rafting

The microstructures of the failed creep specimens indicate that rafting occurred sometime during creep deformation. The time at which the onset of rafting occurred is unknown, but rafting is thought to occur relatively early in the creep process[71,91-93], possibly even in the primary creep stage. Prior to creep testing the initial γ' cube length was 0.25 μm, but after the creep tests the thickness of the rafts was in the region of 0.50 μm. This indicates that raft thickening did occur, although it is unknown whether raft thickening was associated with the onset of tertiary creep[92,93] or whether thickening occurred continuously during creep deformation. The thickness of the rafts and the distribution, or "waviness", were essentially the same for almost all of the specimens. This suggests that differences in creep behaviour are not caused by the raft characteristics. An exception is the as received material which did display a greater degree of "waviness". This may account for the short creep lives seen in some of these specimens. In material with poorly aligned rafts there are less γ-γ' interfaces to act as dislocation obstacles and there are more vertical γ channels. Dislocation climb is relatively easy in these situations[78,87,89,93]. Creep behaviour is generally poor where the rafts are poorly aligned.

7. Conclusions

1. MarM-002 has a gamma prime solvus temperature of 1260°C. Solution treatment at 1260°C dissolves all of the primary γ' and secondary γ'.

2. The eutectic γ' solvus temperature is 1280°C. At 1260°C the volume fraction of eutectic γ' decreases from 15% to 2%. No eutectic γ' dissolves at temperatures of 1240°C and below.

3. Incipient melting occurs at 1240°C in segregated castings. Incipient melting is caused by the presence of Ni-Hf compounds.

4. The incipient melting point and the solution treatment temperature are raised through the use of the varied rate solution heat treatment (VRSHT).

5. Solution treatment at 1260°C using the VRSHT provides a 10% increase in tensile strength over the industry standard 1220°C/2h solution treatment. The tensile properties of the 1220°C/2h specimens are equivalent to the material solution treated at 1240°C using the VRSHT. Poor tensile properties are exhibited by material in the as received condition and in the VRSHT 1220°C condition.

6. The improved tensile properties of the VRSHT 1260°C specimens are caused by the increased volume fraction of fine γ' and the removal of failure initiation sites. These effects arise from extensive eutectic γ' dissolution.

7. The lower tensile properties exhibited by the remainder of the specimens are due to the presence of varying amounts of the large primary γ' and the eutectic γ'.

8. The shortest creep lives of the 1220°C/2h, VRSHT 1240°C and the VRSHT 1260°C specimens are similar, and superior to specimens in the as received or VRSHT 1220°C conditions.

9. Creep properties of the VRSHT 1260°C specimens are not improved by the increased volume fraction of fine γ' because of failure initiation at the carbide sites. However, greater consistency in creep life is seen in the VRSHT 1260°C specimens. This is attributed to the removal of the eutectic γ' and primary γ'.

10. Coarse primary γ' and eutectic γ' are responsible for the poor creep lives of the as received material and the VRSHT 1220°C specimens.

11. Most creep curves are dominated by tertiary creep. This suggests rapid formation of the dislocation network and no equilibrium between work hardening and recovery. Resolved shear stresses are expected to be high in the material since the specimens are expected to have a [001] orientation.

12. Some creep curves contain primary, secondary and tertiary creep stages. This is attributed to a lower resolved shear stress. The specimens exhibiting primary, secondary and tertiary creep may have an orientation that is not in the [001] direction. Instead a direction with a lower resolved shear stress, such as the [111] orientation, may be favoured.

8. References

1. K. Harris, G.L. Erickson and R.E. Schwer, *Metals Handbook*, Vol.1, 10th Ed., ASM.

2. H.E. Miller and W.L.Chambers, *Superalloys II "High Temperature Materials for Aerospace and Industrial Power"*, John Wiley & Sons, 1987, eds. C.T. Sims, M.S. Stoloff and W.C. Hagel, pp. 27-56.

3. M. Gell, D.N. Duhl and A.F. Giamei, *Superalloys 1980 "Proc. 4th Intl. Symp. Superalloys"*, Seven Springs, PA, USA, ASM, 21-25th Sept. 1980, eds. J.K. Tien et al, pp. 205-214.

4. F.L.Versnyder and M.E.Shank, *Mater. Sci. Eng.*, Vol. 6 No. 4, 1970, pp. 213-247.

5. K. Harris, G.L. Erickson and R.E. Schwer, "CMSX Single Crystal, CM DS & Integral Wheel Alloys Properties & Performance" , presented at the High Temperature Alloys for Gas Turbines and Other Applications Cost 50/501 Conference, Liege, Oct. 6-9, 1986.

6. K. Harris, G.L. Erckson, R.E. Schwer, D.J. Frasier and J.R. Whetstone, "Process and Alloy Optimization for CMSX-4 Superalloy Single Crystal Airfoils", presented at the High Temperature Materials for Power Engineering 1990 Cost 50/501 Conference, Liege, Sept.24-27, 1990.

7. K.Harris, G.L. Erickson, S.L. Sikkenga, W.D. Brentnall, J.M. Aurrecoechea and K.G. Kubarych, " Development of the Rhenium Containing Superalloys CMSX-4 & CM 186LC for Single Crystal Blade and Directionally Solidified Vane Applications in Advanced Turbine Engines", 7th Int. Symp. on Superalloys, Seven Springs, Sept. 20-24, 1992.

8. A.D.Cetel and D.N.Duhl, *Superalloys 1988*, eds. S.Reichman et al, The Metallurgical Society, 1988, pp. 235-244.

9. G.L. Erickson, K. Harris and R.E. Schwer, "Directionally Solidified DS CM 247 LC - Optimized Mechanical Properties Resulting from Extensive γ' Solutioning", Gas Turbine Conference and Exhibit, Houston, Texas, USA, 18-21 March 1985.

10. C.T. Sims, *Superalloys II "High Temperature Materials for Aerospace and Industrial Power"*, John Wiley & Sons, eds. C.T. Sims, N.S. Stoloff and W.C. Hagel, pp. 217-239.

11. H. Harada, T. Yamagata, S. Nakazawa, K. Ohno and M. Yamazaki, *Proc. of "High Temperature Matrials for Power Engineering 1990"*, Liege, Belgium, 24-27th Sept. 1990, Kluwer Academic Publishers, eds. E. Bachelet et al, pp. 1319-1328.

12. M.J. Donachie and O.H. Kriege, J. Mater., *JMSLSA*, Vol. 7 No.3, Sept. 1972, pp. 269-278.

13. M.V. Nathal and L.J. Ebert, *Metall. Trans.*, Vol. 16A, Oct.1985, pp. 1849-1862.

14. G.P. Sabol and R. Stickler, *Phys. Stat. Sol.*, Vol. 35, 1969, pp. 11-52.

15. A.K. Jena and M.C.. Chaturvedi , *J. Mater. Sci.*, Vol. 19, 1984, pp. 3121-3139.

16. D. Blavette and A. Bostel, *Acta Metall.*, 1984, Vol. 32, pp. 811-816.

17. D. Blavette, P. Caron and T. Khan, *Scripta Metall.*, Vol. 20, 1986, pp.1345-1400.

18. R. Schmidt and M. Feller-Kniepmeier, *Scripta Metall. Mater.*, Vol. 26, 1992, pp. 1919-1924.

19. R.A. Ricks, A.J. Porter and R.C. Ecob, *Acta Metall.*, Vol. 31, 1983, pp. 43-53.

20. M. Doi, T. Miyazaki and T. Wakatsuki, *Mater. Sci. Eng.*, Vol. 74, 1985, pp. 139-145.

21. E.W. Ross ans C.T. Sims, *Superalloys II "High Temperature Materials for Aerospace and Industrial Power"*, John Wiley & Sons, eds. C.T. Sims, N.S. Stoloff and W.C. Hagel, pp. 97-131.

22. A. Baldan, *Z. Metallkde.*, Bd. 80, 1989, H. 9, pp. 635-642.

23. A. Baldan and J.M. Benson, *Z. Metallkde.*, Bd. 81, 1990, H.6, pp. 446-451.

24. Y.R. Zheng and Y.L. Cai, *Superalloys 1980 "Proc. 4th Intl. Symp. Superalloys"*, Seven Springs, PA, USA, ASM, 21-25th Sept. 1980, eds. J.K. Tien et al, pp. 465-472.

25. C. Lund and J.F. Radavich, *Superalloys 1980 "Proc. 4th Intl. Symp. Superalloys"*, Seven Springs, PA, USA, ASM, 21-25th Sept. 1980, eds. J.K. Tien et al, pp. 85-98.

26. A.A. Hopgood, A. Nicholls, G.D.W. Smith and J.W. Martin, *Mater. Sci. Tech.*, Vol. 4, Feb. 1988, pp. 146-152.

27. D.N. Duhl, *Superalloys II "High Temperature Materials for Aerospace and Industrial Power"*, John Wiley & Sons, eds. C.T. Sims, N.S. Stoloff and W.C. Hagel, pp. 189-214.

28. J. Smith, Ph.D. Thesis, University of Illinois, Urbana-Champaign, U.S.A., 1987.

29. R.A. MacKay and M.V. Nathal, *Acta Metall. Mater.*, Vol. 38 No. 6, 1990, pp. 993-1005.

30. J.E. Doherty, B.H. Kear and A.F. Giamei, *J. Metals*, November 1971, pp. 59-62.

31. J.L. Smialek and G.M. Meier, *Superalloys II "High Temperature Materials for Aerospace and Industrial Power"*, John Wiley & Sons, eds. C.T. Sims, N.S. Stoloff and W.C. Hagel, pp. 293-323.

32. F.S. Pettit and C.S. Giggins, *Superalloys II "High Temperature Materials for Aerospace and Industrial Power"*, John Wiley & Sons, eds. C.T. Sims, N.S. Stoloff and W.C. Hagel, pp. 327-357.

33. I.M. Lifshitz and V.V. Sloyozov, *J. Phys. Chem. Solids*, Vol. 19, 1961, p. 35. as referenced in (28) and (29)

34. C. Wagner, *Z. Electrochem.*, 1961, p. 581, as referenced in (28) and (29).

35. A.A. Hopgood and J.W. Martin, *Mater. Sci. Tech.*, Vol. 2, June 1986, pp. 543-546.

36. A.D. Brailsford and P. Wynblatt, *Acta Metall.*, Vol. 27, 1979, pp. 489-497.

37. C.S. Jayanth and P. Nash, *J. Mater. Sci.*, Vol. 24, 1989, pp. 3041-3052.

38. P.W. Voorhees and M.E. Glickman, *Acta Metall.*, Vol. 32, 1984, pp. 2013-2030.

39. I.M. Wolff, *Mater. Charaterization*, Vol. 29, 1992, pp. 55-61.

40. Z. Yunrong, W. Luobao and L. Chenggong, *Proc. 1st ASM Europe. Tech. Conference "Advanced Materials and Processing Techniques for Structural Applications"*, Paris, 7-9th,Sept. 1987, eds. T. Khan and A. Lasalmonie, pp. 111-118.

41. Z. Yunrong and C. Yulin, *Superalloys 1980, Proc. of the 4th Intl. Symp. on Superalloys*, Seven Springs, PA, USA, 21-25th Sept., ASM, eds. J.K. Tien et al, pp. 465-472.

42. A. Baldan, *J. Mater. Sci.*, Vol. 25, Oct. 1990, pp. 4341-4348.

43. E. Gozlan, M. Bamberger and S.F. Dimfeld, *J. Mater. Sci.*, Vol. 27, 1992, pp. 3869-3875.

44. M. McLean, *Directionally Solidified Materials for High Temperature Service*, The Metals Soc., 1983, ed. M. McLean, pp. 151-156.

45. A.K. Bhambri, T.Z. Kattamis and J.E. Morral, *Metall. Trans.*, Vol.6B, 1975, pp. 523-537.

46. J.K. Tien and R.P. Gamble, *Mater. Sci. Eng.*, Vol. 8, 1971, pp. 152-160

47. R. Fernandez, J.C. Lecomte and T.E. Kattamis, *Metall. Trans.*, Vol. 9A, 1978, pp. 1381-1386.

48. V.A. Wills and D.G. McCartney, *Mater. Sci. Eng.*, Vol. A145, 1991, pp. 223-232.

49. R. Sellamuthu and A.F. Giamei, *Metall. Trans.*, Vol. 17A, March 1986, pp. 419-428.

50. K.L. Zeisler-Mashl and B.J. Pletka, *Superalloys 1992,* eds. Antolovich, R.W. et al, The Minerals, Metals and Materials Soc., pp. 175-184.

51. P. Viatour, D. Coutsouradis and L. HabRaken, *"High Temperature Alloys for Gas Turbines"*, 1978, Applied Science Publishers, eds. D. Coutsouradis et al, pp. 875-891.

52. H. Burt, J.P. Dennison I.C. Elliot and B. Wilshire, *Mater. Sci. Eng.*, Vol. 53, 1982, pp. 245-250.

53. R. Labusch, *Acta Metall.*, Vol. 20, 1972, pp. 917-927.

54. L.M. Brown and R.K. Ham, *Strengthening Methods in Crystals*, Elsevier, Amsterdam, 1971, p.9, as referenced by N.S. Stoloff, *Superalloys II*, 1987, John Wiley & Sons, eds. C.T. Sims, N.S. Stoloff and W.C. Hagel, pp. 61-95.

55. S.M. Copley and B.H. Kear, *TMS-AIME*, Vol.239, 1967, pp. 977-984, as referenced by N.S. Stoloff, *Superalloys II*, 1987, John Wiley & Sons, eds. C.T. Sims, N.S. Stoloff and W.C. Hagel, pp. 61-95.

56. V. Gerold and H. Haberkorn, *Phys. Stat. Sol.*, Vol.16, 1966, pp. 675, as referenced by N.S. Stoloff, *Superalloys II*, 1987, John Wiley & Sons, eds. C.T. Sims, N.S. Stoloff and W.C. Hagel, pp. 61-95.

57. E. Orowan, *Symp. on Internal Stresses in Metals*, Institute of Metals, London, 1948, pp. 451-453, as referenced by N.S. Stoloff, *Superalloys II*, 1987, John Wiley & Sons, eds. C.T. Sims, N.S. Stoloff and W.C. Hagel, pp. 61-95.

58. P.H. Thornton, R.G. Davies and T.L. Johnson, *Metall. Trans.*, Vol. 1, 1970, pp. 207-218.

59. B.H. Kear, G.R. Leverant and J.M. Oblak, *Trans. ASM*, Vol.62, 1969, pp. 639, as referenced by N.S. Stoloff, *Superalloys II*, 1987, John Wiley & Sons, eds. C.T. Sims, N.S. Stoloff and W.C. Hagel, pp. 61-95.

60. M. Yamaguchi, V. Paidar, D.P. Hope and V. Vitek, *Philos. Mag. A*, Vol. 45, 1982, pp. 867-882.

61. V. Paidar, M. Yamaguchi, D.P. Hope and V. Vitek, *Philos. Mag. A*, Vol. 45, 1982, pp. 883-894.

62. R.G. Davies and N.S. Stoloff, *TMS-AIME*, Vol. 233, 1965, pp. 714-719.

63. O. Noguchi, Y. Oya andT. Suzuki, *Metall. Trans.*,Vol. 12A, 1981, pp. 1647-1653.

64. P. Beardmore, R.G. Davies and T.L. Johnston, *TMS-AIME*, Vol. 245, 1969, pp. 1537-1545.

65. G. Scheunemann-Frerker, H. Gabrisch and M. Feller-Kniepmeier, *Philos. Mag.A*, Vol. 65 No.6, 1992, pp. 1353-1368.

66. B.H. Kear, G.R. Leverant and J.M. Oblak, *Metall. Trans.*, Vol. 4, 1973, pp. 355-362.

67. J. DeHosson, *Mater. Sci. Eng.*, Vol. 81, 1986, pp. 515-523.

68. U. Glatzel and M. Feller-Kniepmeier, *Scripta Metall.*, Vol. 23, 1989, pp. 1839-1844.

69 U. Glatzel and M. Feller-Kniepmeier, *Scripta Metall. Mater.*, Vol. 25, 1991, pp. 1845-1850.

70. S. Schanzer and E. Nembach, *Acta Metall. Mater.*, Vol. 40 No.4, 1992, pp. 803-813.

71. R.A. MacKay and L.J. Ebert, *Metall. Trans.*, Vol. 16A, November 1985, pp. 1969-1982.

72. W.S. Walston, I.M. Bernstein and A.W. Thompson, *Metall. Trans.*, Vol. 22A, June 1991, pp. 1443-1451.

73. M. Gell and G.R. Leverant, *TMS-AIME*, 1968, Vol.242, pp. 1869-1879.

74. T. Khan and P. Caron, *Advanced Materials and Processes, Proc. 1st Europ. Conf. on Advanced Materials and Processes*, Euromat '89, Vol.1 Advanced Processing and High Temperature Materials, eds. H.E. Exner and V. Schumacher, Co-eds. D. Driver and H. Mughrabi, pp. 333-338.

75. O.D. Sherby and P.M. Burke, *Prog. Mater. Sci.*, Vol. 13, pp. 325-390.

76. T.M. Pollock and A.S. Argon, *Acta. Metall. Mater.*, Vol. 40 No. 1, 1992, pp. 1-30.

77. A.A. Hopgood and J.W. Martin, *Mater. Sci. and Eng.*, Vol. 82, 1986, pp. 27-36.

78. P. Caron and T. Khan, *Strength of Metals and Alloys (ICSMA)*, Proc. 8th Intl. Conf. on the Strength of Metals and Alloys, Tampere, Finland, 22-26 August 1988, Vol.2, pp. 893-904.

79. P. Caron and T. Khan, *Mater. Sci. and Eng.*, Vol. 61, 1983, pp. 173-184.

80. T. Link and M. Feller-Kniepmeier, *Metall. Trans. A*, Vol. 23A, January 1992, pp. 99-105.

81. T.L. Lin and Mao Wen, *Mater. Sci. and Eng.*, Vol. A128, 1990, pp. 23-31.

82. T.M. Pollock and A.S. Argon, *Superalloys 1988*, eds. S. Reichman et al, The Metall. Soc., 1988, pp. 285-294.

83. B.H. Kear and G.R. Leverant, *Metall. Trans.*, Vol. 1, 1970, pp. 491-.498.

84. T.M. Pollock and A.S. Argon, *Acta. Metall. Mater.*, Vol. 42 No .6, 1994, pp. 1859-1874.

85. J.P. Dennison, I.C. Elliott and B. Wilshire, *Mater. Sci. and Eng.*, Vol. 53, 1982, pp. 291-293.

86. W. Schneider, J. Hammer and H. Mughrabi, *Superalloys 1992*, eds. Antolovich, R.W. et al, The Minerals, Metals and Materials Society, 1992, pp. 589-598.

87. P. Caron and T. Khan, *Mater. Sci. Tech.*, Vol. 2, May 1986, pp. 486-492.

88. J.J. Jackson, M.J. Donachie, R.J. Henricks and M. Gell, *Metall. Trans.* A, Vol. 8A, Oct. 1977, pp. 1615-1620.

89. M.V. Nathal, *Metall. Trans. A*, Vol. 18A, Nov.1987, pp. 1961-1970.

90. I.L. Svetlov, B.A. Golovko, A.I. Epishin and N.P. Abalakin, *Scripta Metall. Mater.*, Vol. 26, 1992, pp. 1353-1358.

91. R.A. MacKay and L.J. Ebert, *Scripta Metall.*, Vol. 17, 1983, pp. 1217-1222.

92. M.V. Nathal and L.J. Ebert, *Scripta Metall.*, Vol. 17, 1983, pp. 1151-1154.

93. M.V. Nathal and L.J. Ebert, *Metall. Trans.*, Vol. 16A, March 1985, pp. 427-439.

94. S.M. Copley, *Fracture and Failure : Analyses, Mechanisms and Applications, Proc. ASM Western Metal and Tool Exposition and Conference (WESTEC)*, 17-20 Mar. 1980, Los Angeles, USA, eds. P.P. Tung, S.P. Agrawal, A. Kumar and M. Katcher, pp. 111-114.

95. E.A. Ault, United States Patent 4 717 432, 5 Jan. 1988.

96. G.L. Erickson, K. Harris and R.E. Schwer, "Optimized Superalloy Manufacturing Process for Critical Investment Cast Components", presented at the 1984 TMS-AIME Annual Meeting, Los Angeles, California, U.S.A., 28 Feb. 1984.

Appendix I

The composition (wt.%) of the DS and CC MarM-002 is listed in the table below :

Element		Element	
C	0.13	Ga	<10.0 ppm
Si	<0.10	Hf	1.61
Mn	<0.10	In	<0.1 ppm
S	0.002	Mg	<5.0 ppm
Ag	<0.1 ppm	Mo	<0.10
Al	5.56	Pb	0.3 ppm
As	<5.0 ppm	Sb	<1.0 ppm
B	0.015	Se	<2.0 ppm
Bi	<0.1 ppm	Sn	<5.0 ppm
Cd	<0.1 ppm	Ta	2.71
Co	10.19	Te	<1.0 ppm
Cr	8.89	Ti	1.36
Cu	0.07	Tl	<0.2 ppm
Fe	<0.05	V	<0.10
Ni	Balance	W	10.09
Zr	0.042	Zn	<1.0 ppm